

Advances in non-linear imaging microscopy  
for tissue and *in-vivo* biological samples  
characterization

PhD thesis

by

**VASSILIS TSAFAS**

University of Crete  
Department of Physics

2021



**FORTH**

INSTITUTE OF ELECTRONIC STRUCTURE AND LASER

Εξελίξεις στη μη γραμμική απεικονιστική  
μικροσκοπία για το χαρακτηρισμό ιστών και  
βιολογικών δειγμάτων *in-vivo*

Διδακτορική Διατριβή

**ΒΑΣΙΛΗΣ ΤΣΑΦΑΣ**

Πανεπιστήμιο Κρήτης  
Τμήμα Φυσικής

2021



**FORTH**

INSTITUTE OF ELECTRONIC STRUCTURE AND LASER

*Supervised by :*

**Professor Costas Fotakis**

**Dr. George Filippidis**

*Advisor Committee:*

**Professor Costas Fotakis**

**Professor Dimitris Charalambidis**

**Professor Nektarios Tavernarakis**

This doctoral thesis was financially supported by the Hellenic Foundation for Research and Innovation (HFRI) and the General Secretariat for Research and Technology (GSRT).



## List of publication during this thesis:

### PEER-REVIEWED JOURNALS PUBLICATIONS

**V. Tsafas**, K. Giouroukou, K. Kounakis, M. Mari, C. Fotakis, N. Tavernarakis, and G. Filippidis. (2021), “Monitoring aging-associated structural alterations in *Caenorhabditis elegans* striated muscles via PSHG measurements”, *Journal of Biophotonics*, e202100173.

**V. Tsafas**, I. Oikonomidis, E. Gavgiotaki, E. Tzamali, G. Tzedakis, C. Fotakis, I. Athanassakis, and G. Filippidis, (2021), “Application of a deep-learning technique to non-linear images from human tissue biopsies for shedding new light on breast cancer diagnosis”, *IEEE Journal of Biomedical and Health Informatics*.

**V. Tsafas**, E. Gavgiotaki, M. Tzardi, E. Tsafa, C. Fotakis, I. Athanassakis, and G. Filippidis, (2020), “Polarization-dependent second-harmonic generation for collagen-based differentiation of breast cancer samples”, *Journal of Biophotonics*, 13(10), e202000180.

E. Gavgiotaki, G. Filippidis, **V. Tsafas**, S. Bovasianos, G. Kenanakis, V. Georgoulas, M. Tzardi, S. Agelaki and I. Athanassakis, (2020), “Third harmonic generation microscopy distinguishes malignant cell grade in human breast tissue biopsies”, *Scientific Reports*, 10(1), 1-13.

G. J. Tserevelakis, **V. Tsafas**, K. Melessanaki, G. Zacharakis, and G. Filippidis, (2019), “Combined multiphoton fluorescence microscopy and photoacoustic imaging for stratigraphic analysis of paintings”, *Optics letters*, 44(5), 1154-1157.

G. Violakis, **V. Tsafas**, G. Filippidis, and S. Pissadakis, (2019), “Electrically poled, MNA-microstructured optical fibers for second harmonic generation”, *IEEE Journal of Selected Topics in Quantum Electronics*, 26(4), 1-8.

M. Mari, **V. Tsafas**, K. Melessanaki, and G. Filippidis, (2018), “Applications of non-linear imaging microscopy techniques to cultural heritage objects”, *Insight-Non-Destructive Testing and Condition Monitoring*, 60(12), 663-669.

**FULL-LENGTH ARTICLES IN EDITED PEER-REVIEWED VOLUMES**

E. Gavgiotaki, **V. Tsafas**, S. Bovasianos, S. Agelaki, V. Georgoulas, M. Tzardi, I. Athanassakis, G. Filippidis "*Nonlinear imaging of female breast tissue biopsies*" Proceedings of the Society of Photo-optical Instrumentation Engineers (SPIE), Vol 11076, Advances in Microscopic Imaging II, E. Beaufort; S. Pavone Eds, 110760I (June 2019)

G. Violakis, **V. Tsafas**, G. Filippidis, S. Pissadakis "*Implementation of non-linear optical materials inside microstructured optical fibers*" IEEE 22nd International Conference on Transparent Optical Networks (ICTON) TuA6.4, pp1-4 (July 2020)

## Abstract

The use and development of spectroscopic techniques with emphasis on advanced microscopic methods for the timely and accurate diagnosis of diseases such as cancer or the need to understand some of the most important mechanisms of Biology, such as aging, based on observation and extraction of information at the cellular level is an interdisciplinary field of enormous research interest. Non-linear imaging microscopy is a reliable diagnostic tool for microscopic studies, as it is a minimally invasive technique with high resolution, while also providing the ability to simultaneously capture images through different non-linear signals such as: second and third harmonic generation (SHG / THG) or multiphoton excitation fluorescence (MPEF). During the present dissertation, studies were carried out that help the further development of the above techniques for the investigation of various biological problems. In addition, the creation of new data analysis algorithms and the implementation of artificial neural networks open new horizons in the fields of application of nonlinear microscopy.

Specifically, the first of the above studies concerns the application of neural networks to THG images from human biopsy specimens for the accurate diagnosis of breast cancer at subcellular level. Although only the diagnosis of this type of cancer based on the imaging of unstained biopsies through THG was very innovative, it faced a key problem, the need for specialized staff to evaluate and separate the samples. THG mainly depicts optical inhomogeneities, lipids or cell membranes and the diagnosis is based on various characteristics of the cells such as their volume, their morphology and their emitted signal. However, locating cells in THG images is an extremely time consuming process and requires special experience, thus greatly limiting the use of this non-invasive diagnostic technique. The solution to this problem was given through the application of neural networks to categorize specific images. It is worth noting that the application of neural networks in THG images for the diagnosis of breast cancer was done for the first time and its success leads to the elimination of the need for specialized staff and the dramatic reduction of diagnostic time, thus bringing non-linear microscopy one step closer to clinical trials.

The second study also concerns the diagnosis of breast cancer based on the above biopsies and non-linear microscopy, but this time the recorded non-linear signal was that of SHG. Tissues are rich in collagen fibers which is capable of emitting strong SHG signals. In recent years there have been several studies on the dependence of SHG on incoming polarization of radiation (PSHG) and on the quantified information obtained through it, such as the anisotropy parameter  $B$ . Through this parameter but also with the introduction of a new one (ratio parameter) it became possible to completely differentiate between all cancer stages of the biopsies we studied (from benign to third stage). The calculation of both of these parameters takes less than one second for each sample as it is based on the Fourier analysis of PSHG measurements. In addition, a biophysical model was proposed that interprets these results based on the mechanical strain applied to the collagen fibers during the various stages of cancer.

In this dissertation, the capabilities of PSHG in combination with Fourier analysis were also used to study possible structural changes in the striated muscles of the model organism *Caenorhabditis elegans* (*C. elegans*) during aging. The results of this study indicate that the striated muscle structure of *C. elegans* changes as the age of the sample increases. As far as is known, this is the first time that differentiation of the PSHG results has been observed through Fourier analysis from *in-vivo* muscle as the sample age increases. The differentiation was based on the difference of the spectral phases of the recorded PSHG signals. In addition, through the newly introduced ratio parameter, this study showed that the hitherto usual

assumption of cylindrical symmetry for the biophysical model of PSHG lacks in satisfactory and complete description of the recorded data compared to the triangular symmetry, which in turn is inferior to the most general case where the sample does not need to have any particular symmetry.

The last part of this thesis was dedicated to highlight the prospect of non-linear microscopy for application in material studies with the aim of delivering innovative results. Non-linear measurements were used to study Cultural Heritage art works. Specifically, a specially designed algorithm was developed, which through MPEF measurements determines with great accuracy the thickness of the protective varnish layer in a work of art, thus helping in the process of its restoration.

## Περίληψη

Η χρήση και η ανάπτυξη φασματοσκοπικών τεχνικών με έμφαση στις προηγμένες μικροσκοπικές μεθόδους για την έγκαιρη και ακριβή διάγνωση ασθενειών όπως ο καρκίνος ή η ανάγκη για κατανόηση κάποιων από τους σημαντικότερους μηχανισμούς της Βιολογίας, όπως η γήρανση, βασιζόμενη στην παρατήρηση και την εξαγωγή πληροφοριών σε επίπεδο κυττάρου αποτελεί ένα διεπιστημονικό πεδίο με τεράστιο ερευνητικό ενδιαφέρον. Η μη γραμμική απεικονιστική μικροσκοπία είναι ένα αξιόπιστο διαγνωστικό εργαλείο για μελέτες σε μικροσκοπικό επίπεδο, μιας και είναι μια ελάχιστα επεμβατική τεχνική με υψηλή διακριτική ικανότητα, ενώ επιπλέον παρέχει την δυνατότητα για την ταυτόχρονη λήψη εικόνων μέσω διαφορετικών μη γραμμικών σημάτων όπως: γένεσης δεύτερης και τρίτης αρμονικής (SHG/ THG) ή του πολυφωτονικά διεγερόμενου φθορισμού (MPEF). Κατά την παρούσα διατριβή, πραγματοποιήθηκαν μελέτες που βοηθούν την περαιτέρω εξέλιξη των παραπάνω τεχνικών για τη διερεύνηση ποικίλων βιολογικών προβλημάτων. Επιπλέον, η δημιουργία νέων αλγορίθμων ανάλυσης δεδομένων και η εφαρμογή τεχνητών νευρωνικών δικτύων ανοίγουν νέους ορίζοντες στα πεδία εφαρμογής της μη γραμμικής μικροσκοπίας.

Συγκεκριμένα, η πρώτη από τις παραπάνω μελέτες αφορά την εφαρμογή των νευρωνικών δικτύων σε εικόνες THG από ανθρώπινα δείγματα βιοψίας για την ακριβή διάγνωση του καρκίνου του μαστού σε υπό κυτταρικό επίπεδο. Αν και μόνο η διάγνωση αυτού του είδους καρκίνου με βάση την απεικόνιση άβαφων βιοψιών μέσω THG, ήταν ιδιαίτερα καινοτόμος, αντιμετώπιζε ένα βασικό πρόβλημα, την ανάγκη εξειδικευμένου προσωπικού για την αξιολόγηση και τον διαχωρισμό των δειγμάτων. Η THG απεικονίζει κυρίως οπτικές ανομοιογένειες, λιπίδια ή κυτταρικές μεμβράνες και η διάγνωση βασίζεται σε διάφορα χαρακτηριστικά των κυττάρων όπως ο όγκος τους η μορφολογία τους και το εκπεμπόμενο σήμα τους. Ωστόσο ο εντοπισμός των κυττάρων στις εικόνες THG είναι μια εξαιρετικά χρονοβόρα διαδικασία και απαιτεί ιδιαίτερη εμπειρία περιορίζοντας έτσι σε μεγάλο βαθμό την χρήση της συγκεκριμένης μη επεμβατικής διαγνωστικής τεχνικής. Η λύση σε αυτό το πρόβλημα δόθηκε μέσω της εφαρμογής των νευρωνικών δικτύων για την κατηγοριοποίηση των συγκεκριμένων εικόνων. Αξίζει να σημειωθεί ότι η εφαρμογή νευρωνικών δικτύων σε εικόνες THG για την διάγνωση του καρκίνου του μαστού έγινε για πρώτη φορά και η επιτυχία της οδηγεί στην εξάλειψη της ανάγκης εξειδικευμένου προσωπικού και στην δραματική μείωση του χρόνου διάγνωσης φέρνοντας έτσι ένα βήμα πιο κοντά τη μη γραμμική μικροσκοπία σε κλινικές δοκιμές.

Η δεύτερη μελέτη αφορά πάλι τη διάγνωση του καρκίνου του μαστού με βάση τις παραπάνω βιοψίες και τη μη γραμμική μικροσκοπία, όμως αυτή τη φορά το καταγραφόμενο μη γραμμικό σήμα ήταν αυτό της SHG. Οι ιστοί είναι πλούσιοι σε ίνες κολλαγόνου το οποίο είναι ικανό να εκπέμπει ισχυρά SHG σήματα. Τα τελευταία χρόνια έχουν πραγματοποιηθεί αρκετές μελέτες πάνω στην εξάρτηση της SHG από την εισερχόμενη πόλωση της ακτινοβολία (PSHG) και στις ποσοτικοποιημένες πληροφορίες που προκύπτουν μέσω αυτής όπως για παράδειγμα η παράμετρος ανισοτροπίας B. Μέσω αυτής της παραμέτρου αλλά και με την εισαγωγή μιας νέας (ratio parameter) κατέστη δυνατός ο πλήρης διαχωρισμός μεταξύ όλων των καρκινικών σταδίων των υπό μελέτη βιοψιών (από καλοήθους έως και τρίτου σταδίου). Ο υπολογισμών και των δύο αυτών παραμέτρων διαρκεί λιγότερο από ένα δευτερόλεπτο για κάθε δείγμα μιας και βασίζεται στην ανάλυση Fourier των PSHG μετρήσεων. Επιπλέον, προτάθηκε ένα βιοφυσικό μοντέλο το οποίο ερμηνεύει αυτά τα

αποτελέσματα με βάση τις μηχανικές τάσεις που εφαρμόζονται στις ίνες κολλαγόνου κατά τα διάφορα στάδια του καρκίνου.

Στο πλαίσιο αυτής της διατριβής οι δυνατότητες της PSHG σε συνδυασμό με την ανάλυση Fourier χρησιμοποιήθηκαν και για τη μελέτη πιθανών δομικών αλλαγών στους ραβδωτούς μύες του πρότυπου οργανισμού *Caenorhabditis elegans* (C. elegans) κατά τη γήρανση. Τα αποτελέσματα αυτής της έρευνας υποδεικνύουν ότι η δομή των ραβδωτών μυών του C. elegans μεταβάλλεται καθώς αυξάνεται η ηλικία του δείγματος. Από όσο είναι γνωστό, είναι η πρώτη φορά που παρατηρείται διαφοροποίηση των εξαγόμενων PSHG αποτελεσμάτων μέσω ανάλυσης Fourier από μύες *in-vivo* καθώς αυξάνεται η ηλικία του δείγματος. Η διαφοροποίηση στηρίχτηκε στη διαφορά των φασματικών φάσεων των καταγραφόμενων PSHG σημάτων. Επιπλέον μέσω της νεοεισαχθείσας παραμέτρου  $\text{ratio}$  η συγκεκριμένη μελέτη έδειξε ότι η μέχρι τώρα συνήθης παραδοχή της κυλινδρικής συμμετρίας για το βιοφυσικό μοντέλο της PSHG υστερεί στην ικανοποιητική και ολοκληρωμένη περιγραφή των καταγραφόμενων δεδομένων σε σχέση με την τριγωνική συμμετρία, η οποία με την σειρά της, υπολείπεται συγκρινόμενη με την πιο γενική περίπτωση όπου το δείγμα δεν είναι απαραίτητο να διακατέχεται από κάποια συγκεκριμένη συμμετρία.

Το τελευταίο μέρος της παρούσας διατριβής αφιερώθηκε στην ανάδειξη της δυνατότητας της μη γραμμικής μικροσκοπίας για εφαρμογή σε μελέτες υλικών έχοντας ως στόχο την απόδοση καινοτόμων αποτελεσμάτων. Μη γραμμικές μετρήσεις πραγματοποιήθηκαν για την μελέτη έργων Πολιτιστικής κληρονομιάς. Συγκεκριμένα, αναπτύχθηκε ένας ειδικά σχεδιασμένος αλγόριθμος, ο οποίος μέσα από μετρήσεις MPEF προσδιορίζει με μεγάλη ακρίβεια το πάχος του προστατευτικού στρώματος βερνικιού σε ένα ομοίωμα έργου τέχνης βοηθώντας έτσι, στη διαδικασία αποκατάστασης αυτού.

## Ευχαριστίες

Η επιτυχής ολοκλήρωση της παρούσας διατριβής οφείλεται σε μεγάλο βαθμό στη θετική συμβολή κάποιων ανθρώπων τους οποίους θα ήθελα να ευχαριστήσω.

Αρχικά ευχαριστώ ιδιαίτερα για την γενική επίβλεψη αυτής της διατριβής τον Καθηγητή Κώστα Φωτάκη. Η πίστη που έδειξε από προπτυχιακό ακόμα επίπεδο προς το πρόσωπό μου μου έδωσε την απαιτούμενη ώθηση για να πιστέψω στις ικανότητές μου και να ασχοληθώ με τον τομέα της έρευνας.

Ένα μεγάλο ευχαριστώ θα ήταν το λιγότερο που θα μπορούσα να πω και στον συνεπιβλέποντα αυτής της διατριβής Δρ. Γιώργο Φιλιππίδη οποίος είναι και ο υπεύθυνος του εργαστήριου στο οποίο πραγματοποιήθηκαν το σύνολο των απαιτούμενων πειραμάτων (Εργαστήριο Μη Γραμμικής Μικροσκοπίας, ΙΗΔΛ/ ΙΤΕ). Όλον αυτό τον καιρό δεν υπήρξε ούτε μια στιγμή που να μη χρειάστηκα την βοήθειά του και να μην μου την παρείχε απλόχερα. Η εμπειρία, οι γνώσεις και η πορεία του στον τομέα την μη γραμμικής μικροσκοπίας έπαιξαν καθοριστικό ρόλο για την επίλυση οποιουδήποτε προβλήματος και αν προέκυψε. Επιπλέον δεν ήταν οι λίγες και οι φορές στις οποίες συνειδητοποίησα ότι νοιάζονταν για εμένα πιο πολύ από ότι εγώ για τον εαυτό μου.

Στη συνέχεια θα ήθελα να ευχαριστήσω για την συνεργασία μας αλλά και για την βοήθεια που μου προσέφεραν και τα υπόλοιπα μέλη της ομάδας Δρ. Ευαγγέλια Γαυγιωτάκη, Δρ. Μερόπη Μάρη και Κωνσταντίνα Γιουρούκου.

Σε αυτό το σημείο θα ήθελα να επισημάνω επίσης ότι είχα την ευκαιρία να βρίσκομαι σε ένα άριστο εργασιακό περιβάλλον το οποίο οφείλονταν τόσο στα άτομα με τα οποία είχα την τύχη να μοιράζομαι το ίδιο γραφείο όσο και στην πλειοψηφία των ατόμων του ΙΗΔΛ. Δεν είναι τυχαίο άλλωστε το γεγονός ότι κάποιες από τις σημαντικότερες φιλίες που ανέπτυξα είναι με κάποια από τα παραπάνω άτομα για τα οποία έχω και μια ιδιαίτερη εκτίμηση.

Ωστόσο δεν θα μπορούσα να μην ευχαριστήσω και κάποιους ιδιαίτερα κοντινούς μου ανθρώπους οι οποίοι στάθηκαν δίπλα μου σε και στις πιο δύσκολες μέρες.

Τέλος το μεγαλύτερο ευχαριστώ πηγαίνει στην οικογένειά μου η οποία δεν σταματάει ποτέ και σε τίποτα να με στηρίζει.

## Αφιέρωση

*Στη συνονόματη γιαγιά μου που δεν πρόλαβε να με δει “γιατρό”*

# Contents

Chapter 1 - Non Linear Optical Microscopy (NLOM).....	14
1.1 Introduction .....	14
1.2 Recent biological applications of NLOM.....	15
1.3 Multi Photon Excitation Fluorescence (MPEF) .....	18
1.4 Second and Third Harmonic Generation (SHG, THG) .....	21
1.5 Polarization-depended SHG (PSHG) Theory .....	26
1.6 NLOM setup.....	29
Chapter 2 - THG as a new diagnostic tool for discrimination of breast tissue biopsies samples .....	32
2.1 Introduction .....	32
2.2 Manual based analysis of THG images .....	32
2.2.1 Materials and Methods .....	32
2.2.2 Results .....	34
2.2.3 Discussion .....	37
2.3 THG image analysis through Neural Networks .....	38
2.3.1 Introduction to Neural Networks .....	38
2.3.2 Convolutional Neural Networks .....	38
2.3.3 Methods .....	44
2.3.4 Results .....	45
2.3.5 Discussion .....	51
Chapter 3 - Novel PSHG studies .....	53
3.1 PSHG for collagen-based differentiation of breast cancer samples .....	53
3.1.1 Introduction .....	53
3.1.2 Materials and Methods .....	54
3.1.3 Results .....	56
3.1.4 Discussion .....	59
3.2 PSHG for myosin structural alterations of C elegans body-muscles during aging .....	62
3.2.1 Introduction .....	62
3.2.2 Materials and Methods .....	62
3.2.3 Results .....	67
3.2.4 Discussion .....	70
Chapter 4 - NLOM for material characterization .....	72
4.1 Introduction .....	72
4.2 Specially designed deconvolution algorithm for MPEF signals.....	74

Chapter 5 - Conclusions .....	79
Chapter 6 - Bibliography .....	81

# Chapter 1 - Non Linear Optical Microscopy (NLOM)

## 1.1 Introduction

A nonlinear optical process according to Boyd occurs when “the response of a material system to an applied optical field depends in a nonlinear manner upon the strength of the optical field”[1]. The first described nonlinear optical phenomenon, the quantum mechanism of two photon molecular excitation, presented in 1931 by Maria Goeppert-Mayer in her doctoral thesis. However, two photon excitation was experimentally observed for the first time by Wolfgang Kaiser et al. after 30 years in 1961. During the same year Second Harmonic Generation (SHG), one of the most used nonlinear optical phenomenon, observed by Franken and coworkers. It is not a coincidence that the first working laser presented one year before in 1960 by Maiman. Laser is the only light source with high enough intensity to produce nonlinear optical phenomena and at the same time, a large number of laser applications owe their existence to nonlinear optics[2]. The first nonlinear optical microscopy (NLOM) image was created by Gannaway and Sheppard at Oxford in 1977 when they combined the nonlinear phenomenon of SHG with a laser scanning microscope. Afterward, in 1990 Denk, Strickler, and Webb presented the first practical biological application of NLOM where this time the scanning procedure was done through galvanometric (galvo) mirrors and laser beam moved relative to the sample. A few years later NLOM starts to be a well-established microscopy technique as femtosecond pulsed Ti:sapphire lasers, which have the necessary intensity to induce high enough nonlinear signals, became commercially available, stable, user friendly systems[3]. Some of the main advantages of NLOM are[4]:

- Penetration depth up to 500  $\mu\text{m}$ , due to the fact that many materials and especially biological samples present an optical window in the near infrared light spectrum in which usually located the excitation laser wavelengths
- The nonlinear response of the material to the light intensity provides intrinsic 3D resolution even below 1 $\mu\text{m}$  as only a small volume around the focal spot have high enough intensity to produce nonlinear phenomena
- Simultaneous acquisition of different nonlinear signals like Multiphoton Excitation Fluorescence (MPEF), SHG, and Third Harmonic Generation (THG) that provide complementary information from the specimens
- Quantitative information about the sample due to the dependence of nonlinear signal from the incident laser polarization[5] or lifetime fluorescence
- It is a minimally invasive technique as there is no need for special sample preparation and at the same time, only a very small volume of laser light interacts with the sample. Especially in cases of SHG or THG, the sample does not absorb any laser light so there is no thermal deposition on it

From the above characteristics, it is clear why NLOM is a suitable imaging technique for biomedical research and this fact is presented by the annual steadily increase numbers of publications or conferences in that field (Figure 1.1).

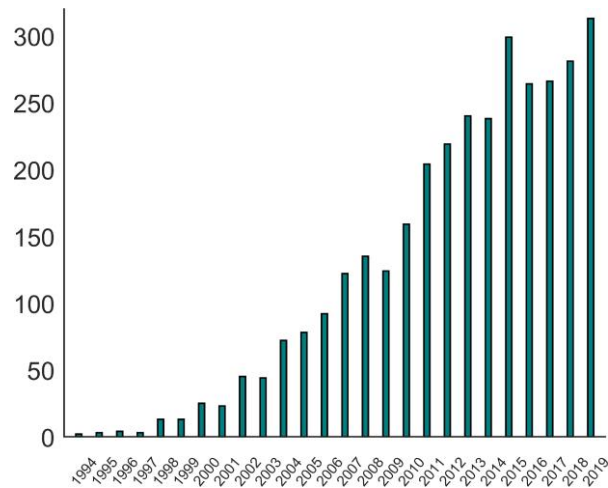


Figure 1.1 : Annual publications based on webofknowledge.com of studies using NLOM.

The possibility offered by NLOM for in-vivo investigation of cellular and sub-cellular activities can provide valuable information in fields such: neurobiology[6], embryology[7], tumor biology[5], etc. This information leads to a deeper understanding of some fundamental biological questions and improving the quality of life for millions of people.

Finally, it worth mentioning that NLOM is not limited to biomedical applications. NLOM, due to minimal invasive interaction with the sample and the complementary information can provide new insights, in the materials science through imaging objects from Cultural Heritage[8][9][10] to optic fiber [11][12][13] and 2D materials[14][15][16].

## 1.2 Recent biological applications of NLOM

Nowadays, due to the fact that human health around the world is affected by diseases that are expressed at the cellular level such as cancer [17], the need to develop minimally invasive techniques and tools capable of diagnosing these diseases is greater than ever. NLOM seems to be suitable for this kind of studies since allows to perform label-free, vital, and three-dimensional observations in biological specimens, from in vitro samples to preclinical in vivo models and, potentially, to clinical applications[18]. Indeed, in 2016 presented the first THG images from unstained but formalin-fixed and paraffin-embedded breast tissues biopsy samples in epi-direction[19]. In the same year was published a study on the pathology of human brain tumors based on THG images again in epi-direction from fresh samples while the imaging was performed in a thickness of a few hundreds of micrometers [20]. These images can illustrate some of the main cell characteristics that pathologists taking into account in order to decide if they are malignant or not. In addition, the setup of this study was capable at the same time to record the reflected SHG signal creating combined images like the following ones.

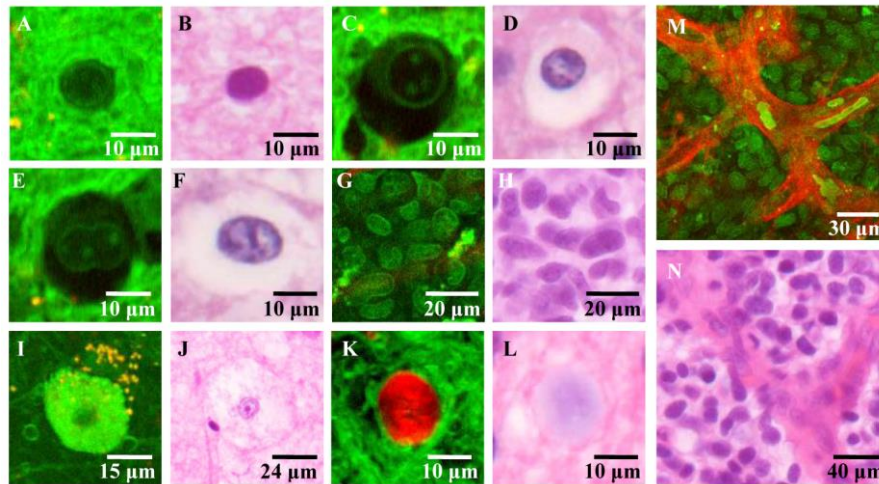


Figure 1.2 : (A, C, E, G, I, K, M) Merged THG (green) with SHG (red) images of different glioma tissues areas and grades with the corresponding H&E images (B, D, F, H, J, L, N). (A, B) Glial cell with a nearly round nucleus and large nuclear/cytoplasm ratio. (C, D) Glial cell with a round nucleus and smaller nuclear/cytoplasm ratio. (E, F) Glial cell with an indented nucleus and multiple nucleoli. (G, H) Highly cellular area in high-grade glioma (glioblastoma) with multiple pleomorphic tumor cell nuclei with dense chromatin and high nuclear/cytoplasmic ratio. (I, J) A neuronal or glial cell with vacuolated cytoplasm in the edematic peritumoral neocortex of the high-grade glioma tissue. Autofluorescent deposits in the neuropil appear as yellow dots. (K, L) Corpus amylaceum surrounded by neuropil. (M, N) Intense vascular proliferation in high-grade glioma focus.[20]

The feasibility of a non-linear phenomenon to epi-detected is necessary for a real-time diagnosis via an appropriate endoscope. Many multimodal nonlinear endoscopies setups have been developed during the last years promising to provide an overview to the surgeon of the pathology area that extends inside the tissue during the surgery[21][22][23]. Applications on in-vivo samples such as rat's kidney, or mice's intestinal mucosa, kidney, and ear tissue, indicate that the technology of nonlinear endoscopy is close to be employed in the clinical environment [24][25][26]. Although NLOM can be used to diagnose various types of malignancies in tissues of breast[27], pancreas[28], and colorectal[29], it is not limited only to these applications. In fact, NLOM could also be used for studies on cell response to drugs for cancer treatment[30] or even as a microsurgery tool[31].

Except for cancer studies, NLOM applications extent in a plethora of biomedical problems or fundamental biological mechanism such as cell activation. For example, it has been shown that the BV-2 microglia activated cells present a significant increase of the intensity as well as and of the area of THG signal compared with the normal[32]. Through co-localization of THG and TPEF images, they showed that the largest THG signal is derived from lipid bodies (LB) (Figure 1.3) and thus suggesting that cell activation leads to an increase in their concentration.

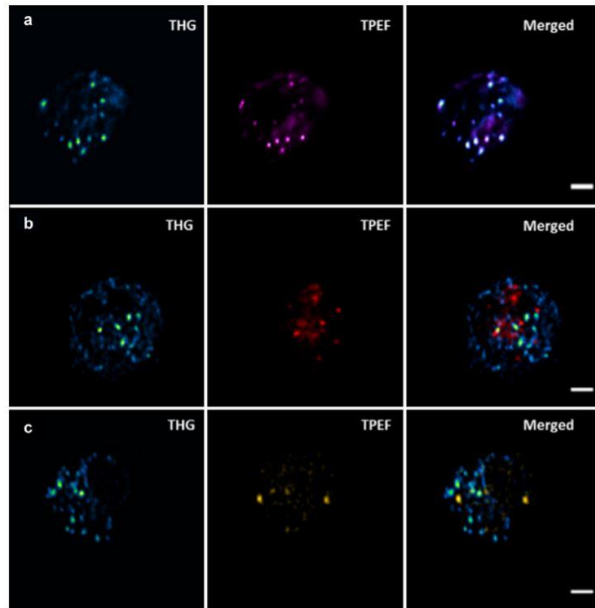


Figure 1.3 : Identification of sub-cellular organelles of BV-2 cells that produce high THG (blue-green) signals. THG and TPEF images were collected simultaneously. (a) 2D image (500 500pixels) of a BV-2 cell stained with Nile red (LB marker - magenta), (b) 2D image of a BV-2 cell stained with Mitotracker red fm (mitochondria marker - red), (c) 2D image of a BV-2 cell stained with Alexa 488 (late endosomes marker - yellow). Scale bars denote 5  $\mu\text{m}$ . [32]

The fact that most of THG signal arises from LB was also verified via the performance of the corresponding co-localization measurements and for *C. elegans* samples *in-vivo* (Figure 1.4) [33]. Based on an appropriate quantification of THG images they showed that the ectopic accumulation of fat on the pharyngeal muscles increases in wild-type *C. elegans* with the process of aging.

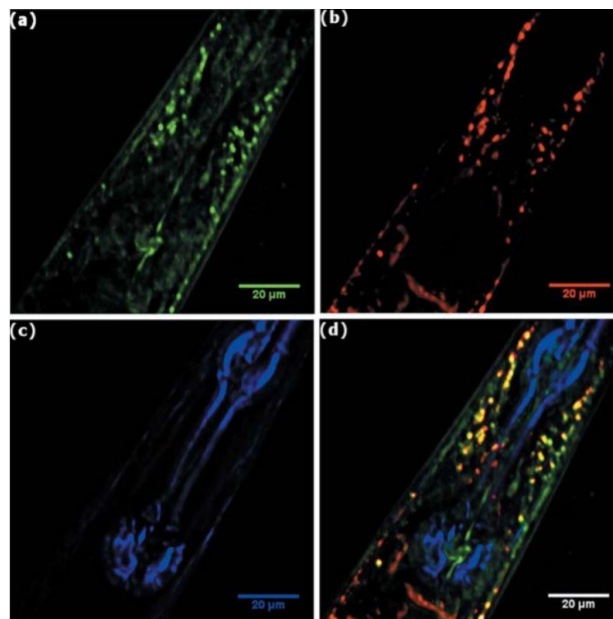


Figure 1.4 : The three-color images of the head area of a 1-day-old stained adult *C. elegans*. (a) THG (green) arises from internal head structures (mostly lipids), (b) TPEF (red) emanating from the lipids stained with Nile Red, (c) SHG (purple) originating from the

*musculature of the head region (pharyngeal and body wall muscles), and (d) the merge of all three colors.* [33]

Another field where the implementation of NLOM can also provide valuable information is embryology. A recent study via three-dimensional multiphoton microscopy showed that glands are connected directly to the crypt encasing the mouse embryo during implantation and for this reason are crucial for the pregnancy success[34]. Moreover another study in mouse embryos was focused on the early heart development in genetic mouse models based on the SHG produced by the extracellular matrix (ECM) collagen fibers. They showed that the organization and the content of ECM fibrillary collagen, which is central to heart biomechanics, regulating tissue strength and elasticity are strongly related to the cardiac contractility[35]. In addition, there are other model organisms whose embryos can be studied through NLOM and providing useful information for the development of various organs. For example zebrafish embryos was used in order to examine neural crest migration into the developing of eye[36]. Neural crest is a transient population of migratory stem cells that give rise to numerous cell types throughout the body. A recent work highlighted the truly non-invasive nature of NLOM, as it had no effect on stem cell differentiation[37]. This means that NLOM is suitable for skeletal research, regeneration medicine and tissue engineering. Indeed, in 2017 presented for the first time a quantitative evaluation of tissue-engineered skeletal muscle based on NLOM[38]. In that study presented a positive correlation between structural NLOM measures and force production suggesting thus that NLOM could potentially serve as an accurate predictor of functional behaviors, such as integration and tissue regeneration, after implantation. A case of very important tissue regeneration is that which occurs during wound healing. Improved knowledge in this area could permit the development of treatments to support wound healing, especially in patients with suppressed immune systems and impaired wound healing responses. For a better understanding of this biomedical process a special device developed, which allowed long-term collagen fibers reorganization observation during wound healing via SHG measurements [39]. More recently, (in 2019), the results of another study focused on impaired wound healing due to diabetes suggested again that NLOM is one of the most suitable tools for biomedical applications and research[40].

### 1.3 Multi Photon Excitation Fluorescence (MPEF)

For a better understanding of MPEF and its characteristics, One Photon Excitation Fluorescence (OPEF) will be firstly analyzed.

In OPEF[3], an electron from the ground state level of a molecule interacts with a photon. If the photon energy is higher than the energy difference between the first excited state and the ground state then the photon will be absorbed by the electron causing thus the transition of the electron to a first excited state level. Afterwards, through non radiative processes such as thermal relaxation, the excited electron loses a part of its energy and demoted to the lowest vibrational level of the excited state. Finally, the radiative electron de-activation and returning to the ground state via the emission of a photon called fluorescence. This procedure is illustrated in the image below.

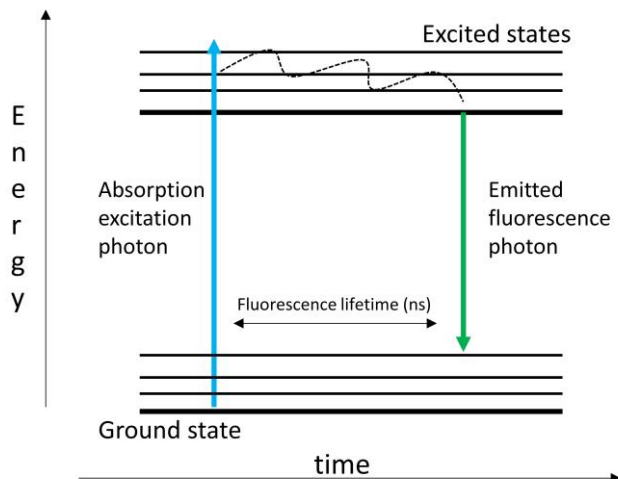


Figure 1.5 : Example of OPEF Jablonski energy diagram. The horizontal axis refers to time and the vertical to electron energy within a molecule. Since the absorption process last only a few femtoseconds it appears as instantaneous. The horizontal black lines denote the energy eigenvalues of the molecule, where the thick and the thin lines correspond to the electronic and vibrational states respectively. In addition, the blue and green vertical lines denote the absorbed and emitted photons respectively. Finally, the curved line represents non radiative de activation due to the thermal relaxation of the electron.

From Figure 1.5 it is clear that the emitted photon will have a longer wavelength compared to the absorbed photon since part of its energy will be converted to heat or kinetic energy of the system due to the aforementioned thermal relaxation of the electron. This effect is known as ‘Stokes shift’ and facilitates the separation of fluorescent signal from the excitation radiation. As shown from equation 1.1 the OPEF absorption rate of a molecule  $W_1$  (photons/sec) increased linearly with incident photon flux  $F$  (photons/cm<sup>2</sup>·sec), and considering that photon flux is proportional to the intensity  $I$  ( $I=F \cdot \hbar \cdot \omega$ ,  $\hbar$ : reduced Planck’s constant,  $\omega$ : frequency of incident light) it is obvious that OPEF is a linear phenomenon. The variable of equation 1.1  $\sigma_1$ , is the cross section of OPEF and has typical a value in order of  $10^{-17}$  cm<sup>2</sup> [41].

$$W_1 = \sigma_1 \cdot F \quad 1.1$$

On the other hand, as will be shown, MPEF is a nonlinear phenomenon. The simplest case of MPEF is Two Photon Excitation Fluorescence (TPEF). In this case, two photons interact with an electron in order to produce one fluorescence photon, and it follows a brief description of the phenomenon:

An electron from the ground state of a molecule interacts this time, with a photon whose energy is a little bit larger than the half of the energy difference between the first excited state and the ground state. Then, the electron excited to an intermediated energy level between the ground state and the first excited state well known as “virtual state”. However, for the reason that the virtual state is not an eigenstate of the molecule, the electron’s lifetime in this state is extremely short. A good approximation in order to estimate electron’s lifetime  $\Delta t$  in a virtual state is through the uncertainty of energy  $\Delta E$  ( $\Delta E \cdot \Delta t \approx \hbar$ ). If we consider that  $\Delta E$  is about half of the energy difference between the first excited state and ground state with a typical value of 1 eV then the electron’s lifetime for this virtual state is about 0.5 fs. Moreover, if during this short time electron interacts with a second identical photon then it will be excited to a vibrational level of the first excited molecule state. Afterward, in the same way as in the OPEF

case, electron through thermal relaxation will lose a part of its energy and demoted to the lowest vibrational level of the excited state. The radiative de-excitation of the electron to a vibrational or a rotational level of the ground stage via the emission of a photon is called fluorescence. In this case, the fluorescence photon's energy will be smaller than the sum of the two incident photons.

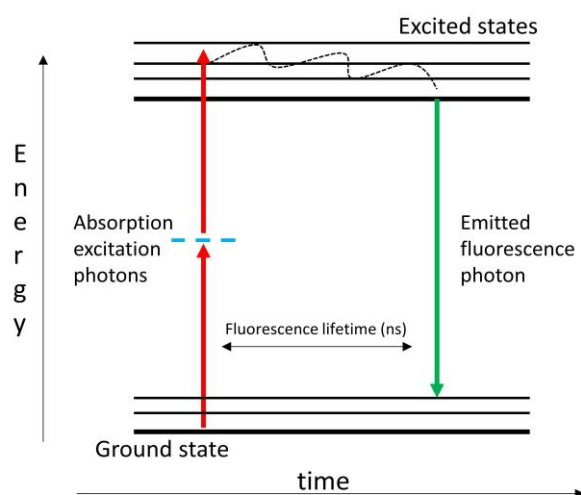


Figure 1.6 : Example of TPEF Jablonski energy diagram. The horizontal axis refers to time and the vertical to electron energy within a molecule. As in Figure 1.5, the horizontal black lines denote the energy eigenvalues of the molecule, where the thick and the thin lines correspond to the electronic and vibrational states respectively. The blue dashed denotes the virtual state energy level, and the colored vertical lines the absorbed and emitted photons. Finally, the curved line represents non radiative de activation due to the thermal relaxation of the electron.

However, the probability of the electron interaction with a second photon while it is at the virtual state is extremely low and for that reason, TPEF needs high photon flux in order to be observed. As mentioned before, photon flux is proportional to the intensity of the radiation, which is proportional to the power of the source and inverse proportional to the radiated area. Now it becomes clearer the need to use high numerical aperture (NA) lenses and short pulse duration lasers. High NA lenses ensure the focusing of the radiation in a small area while ultrashort pulsed lasers ensure the instantaneously high peak power, which is needed in order to produce TPEF signals. The absorption rate  $W_2$  of TPEF as shown from equation 1.2 indicates the non-linear dependence of the phenomenon with the incident radiation flux  $F$  and therefore with the intensity.

$$W_2 = \frac{1}{2} \cdot \sigma_2 \cdot F^2 \quad 1.2$$

Again variable  $\sigma_2$  represents the cross section of the phenomenon with a typical value in the order of  $10^{-50} \text{ cm}^4 \cdot \text{s}/\text{photon}$  [41]. The reason that cross section of TPEF  $\sigma_2$  is much smaller than the cross section of OPEF is that TPEF is extremely unlikely to happen compare with OPEF. However is the combination of this low value of cross section and the non-linear dependence with radiation intensity that gives NLOM one of its most important advantages, which is the 3D high resolution.

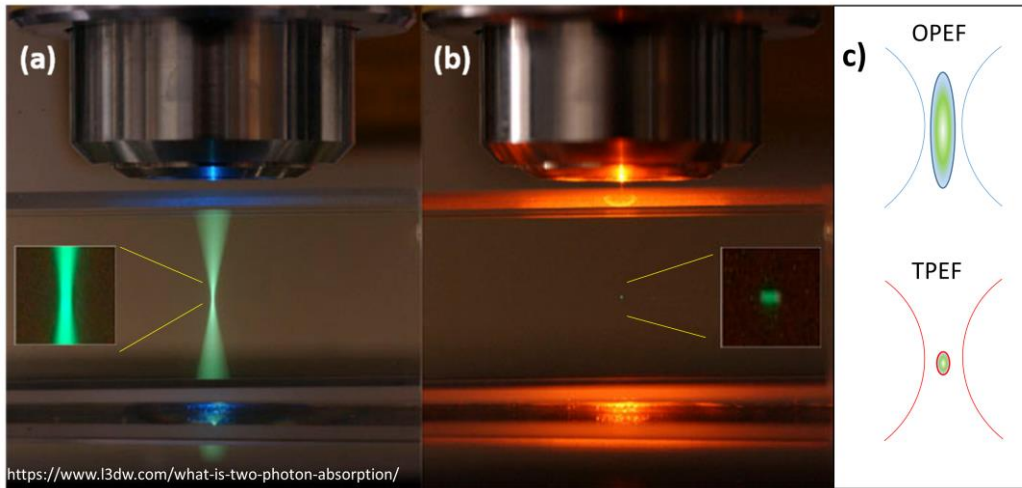


Figure 1.7 : a) OPEF emission (green) from a photoactive solution which is radiated by a continuous wave laser with 488 nm wavelength (blue). The laser light focused inside the solution and the rectangular box zooms in at the focal plane. b) TPEF emission from the same photoactive solution with (a), which radiated by a red pulsed laser. This time an almost invisible green dot of fluorescence appears at the middle of the focal plane. c) Schematic representation of the excited spot from a Gaussian like focused beam in case of OPEF and TPEF respectively.

As Figure 1.7 depicts, in the case of TPEF, a tiny fluorescence spot appears in the center of the focused beam. Only in this volume exist high enough intensities in order to produce TPEF signals and due to the non-linear dependence of the phenomenon on the incident intensity the size of the excited spot decreases rapidly. The size of the excited spot determines the resolution of the imaging technique. As a consequence, the resolution of NLOM starts from a few  $\mu\text{m}$  and drops down to a few hundreds of nm, especially in the case of lateral direction. At the same time side effects like photodamage and photobleaching are minimized in out of focus regions.

Another MPEF process which shares the same principles and advantages is the Three Photon Excitation Fluorescence (3PEF). One of the difference compared with the TPEF, is that in the case of 3PEF, the electron interacts with three photons and excited through two intermediated virtual states. An additional difference is that the absorption rate of 3PEF depends on the third power of incident photon flux with a typical cross section value in order of  $10^{-84} \text{ cm}^6 \cdot \text{s}^2 / \text{photon}^2$  [42]. Finally, one would expect that 3PEF, due to the cubic dependence of its absorption rate on the incident photon flux, would have a better resolution than TPEF, which is not true, as both microscopy techniques have a similar resolution. The reason behind this, as will be discussed in the NLOM setup subsection, is that in the case of 3PEF longer wavelengths must be used which according to the Rayleigh criterion are proportional to the resolution (the longer the wavelength used by a microscopy imaging technique, increase the values of the obtained resolution).

#### 1.4 Second and Third Harmonic Generation (SHG, THG)

Unlike MPEF, Harmonics Generation are multiphoton nonlinear coherent scattering phenomena. For example, in case of SHG, the electron of a molecule interacts with two identical photons whose energy is smaller than the half of the energy difference between the

first excited state and the ground state. After the interaction with the first photon the electron will be found again on an intermediate virtual state. If during electron's lifetime on this state the electron interact with the second photon then it will be promoted to a new higher energy virtual state.

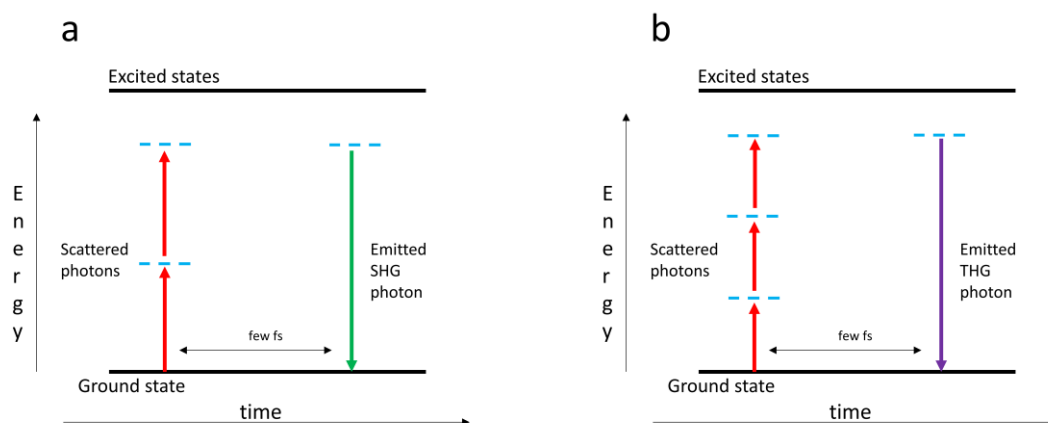


Figure 1.8 : Example of SHG (a) and THG (b) Jablonski energy diagrams. The horizontal axis refers to time and the vertical to electron energy within a molecule. Horizontal black lines denote molecule's energy eigenvalues, blue dashed the virtual states energy levels, and colored vertical lines the scattered and emitted photons.

The electron, due to the fact that the two photons do not have enough energy in order to excite it to the first excited state, will return to the ground state of the molecule through the emission of one photon. But this time the energy of the emitted photon will be exactly the same as the sum of the two incident photons. As shown in Figure 1.8a, the electron is not able to reach any vibrational level of the first excited state. For this reason, the electron will not lose part of its energy through thermal relaxation and as a result, the emitted photon will have exactly twice the frequency of one of the incident photons. At this point, it should be mentioned that, if the energy of the laser photons is approximately equal with material's energy gap, the harmonic procedure is enhanced[1]. However, this latter case will not be taken into account in this thesis since the samples studied considered to be off-resonant to laser radiation that was used.

The following equation shows the nonlinear nature of the second harmonic generation signal. The power of SHG depends on the square of the radiation intensity.

$$P_{SHG} = \frac{1}{2} \cdot \sigma_{SHG} \cdot I^2 \quad 1.3$$

The SHG cross section  $\sigma_{SHG}$  of equation 1.3, for one molecule, is about four orders smaller than the TPEF cross section but in practice for standard dye labeling densities due to the coherent summation of SHG fields, the output powers of these two phenomena are comparable[43]. Furthermore, the quadratic dependence of SHG power on the intensity of incoming radiation results in SHG microscopy having approximately the same resolution as TPEF. Nevertheless, one of the most critical differences between these two microscopy techniques is that in the case of SHG there is no need to labeling the sample which is required most of the times in TPEF case. This, in combination with the fact that there is no energy deposition in the sample due thermal relaxation, renders SHG as a minimally invasive technique ideal for in vivo studies. Finally, as expected, THG it is also a coherent scattering

phenomenon (Figure 1.8b) and this phenomenon scales with the third power of the incident radiation intensity. So, THG microscopy has also the same resolution as the aforementioned multiphoton techniques and its main differences, especially with SHG, will be highlighted in the following classical description of the harmonics generation.

In general, the response of any physical system from an external disturbance can be described with a good approximation from a linear function of this disturbance, as long as the system is close to its equilibrium state. In other words, this is nothing else than the first order Taylor approximation when for no disturbance there is no response of the system. A simple but highly representative example is Hooke's law, which states that force required to compress or extend a spring by some distance from its equilibrium position scales linearly with that distance. But the above rule is valid only for small distances, otherwise, this linear dependence stops to be a good approximation of the reality and needs additionally and higher orders of the force in order to describe correctly the generated compression or extension of the spring. Similar nonlinear optical phenomena occur during the interaction of strong electromagnetic fields with common materials. It is well known that an external electric field, through the forces that exerts mainly on the valence electrons of a material, can induce an electric polarization  $P$  (dipole moment per unit volume) inside this material. Under the assumption of a weak field, as in the case of Hooke's law, the induced polarization is proportional to the external electric field. So, for a time dependent electric field  $E(t)$  the polarization  $P(t)$  can be calculated as:

$$P(t) = \varepsilon_0 \cdot \chi^{(1)} \cdot E(t) \quad 1.4$$

where  $\varepsilon_0$  is the permittivity of free space and  $\chi^{(1)}$  is the first order (or linear) susceptibility of the medium. Since  $P(t)$ ,  $E(t)$  are generally three-dimensional vectors  $\chi^{(1)}$  is a second rank tensor.

However, as Hooke's law valid for short distances from the equilibrium state of the spring. This valid and for equation 1.4 which predicts with good precision the induced polarization from a weak electric field. As the electric field getting stronger upper nonlinear terms should take into account in order to describe sufficiently the induced polarization.

$$P(t) = \chi^{(1)} \cdot E(t) + \chi^{(2)} \cdot E^2(t) + \chi^{(3)} \cdot E^3(t) \dots \quad 1.5$$

As before  $\chi^{(2)}$ ,  $\chi^{(3)}$  are third and fourth rank tensors known as the second and third order nonlinear optical susceptibilities respectively. At this point it must be notice that each term of the induced polarization from the above equation can act as a source for the Maxwell's Equations leading to:

$$\nabla^2 E - \frac{\varepsilon^{(1)}}{c^2} \cdot \frac{\partial^2 E}{\partial t^2} = \frac{1}{\varepsilon_0 \cdot c^2} \cdot \frac{\partial^2 P^{NL}}{\partial t^2} \quad 1.6$$

whereas  $c$  is the speed of light in vacuum,  $\varepsilon^{(1)}$  is the dimensionless relative permittivity of the material where propagates the electric field  $E$ , and  $P^{NL}$  is the nonlinear part of the induced polarization. In the case of an oscillating electric field entering the material with a frequency  $\omega$  the propagating electric field and the induced polarization can be expressed as the sum of their frequency components based on  $\omega$ . In order to be valid for each of these frequency components Equation 1.6 re-expressed to the following form:

$$\nabla^2 E_n - \frac{\varepsilon^{(1)}(\omega_n)}{c^2} \cdot \frac{\partial^2 E_n}{\partial t^2} = \frac{1}{\varepsilon_0 \cdot c^2} \cdot \frac{\partial^2 P_n^{NL}}{\partial t^2} \quad 1.7$$

The index n of Equation 1.7 referred to  $\omega_n$  frequency component where  $\omega_n = n \cdot \omega$  (the relative permittivity depends on the frequency).

Considering the case of a focused incident Gaussian beam with a confocal parameter b, it turns out from Equation 1.7 that the amplitude of the n-harmonic electric field is proportional to  $J_n$ , where  $J_n$  is equal to:

$$J_n(\Delta k) = \begin{cases} 0, & \Delta k \leq 0 \\ \frac{b}{2} \cdot \frac{2\pi}{(n-2)!} \cdot \left(\frac{b\Delta k}{2}\right)^{n-2} \cdot e^{-\frac{b\Delta k}{2}}, & \Delta k > 0 \end{cases} \quad 1.8$$

$\Delta k$  is known as wavevector mismatch and is equals to:

$$\Delta k = n \cdot k - k_n \quad 1.9$$

where k and  $k_n$  are the wavenumber of the incident (fundamental) beam and of the produced harmonic wave respectively.

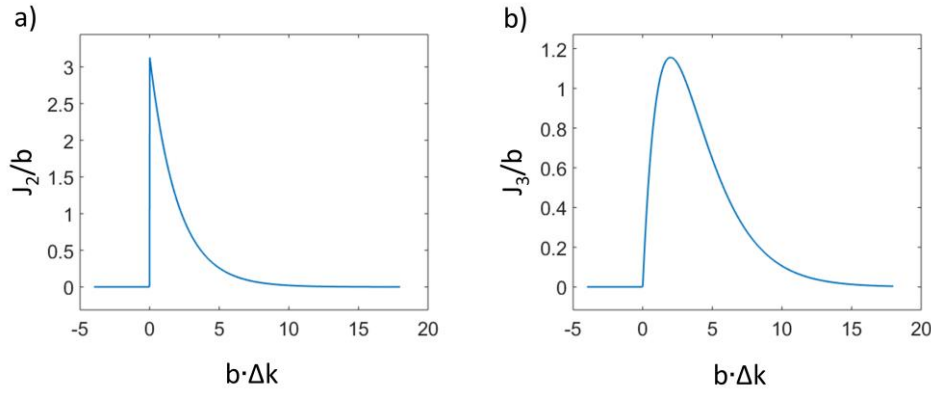


Figure 1.9 : Plot diagrams of Equation 1.8 for  $n=2$  (a) and  $n=3$  (b).

Figure 1.9a shows that in the case of SHG ( $n=2$ ) the  $J_2$  takes its maximum value for a very small positive  $\Delta k$  (practically zero). This means that the signal of the produced SHG maximized under the so-called perfect phase matching condition ( $\Delta k=0$ ). Setting thus  $\Delta k$  to zero in Equation 1.9 and replacing k,  $k_2$  with the  $n(\omega) \cdot \omega/c$  and  $n(2\omega) \cdot 2\omega/c$  the condition of the perfect phase match expressed as:

$$n(\omega) = n(2\omega) \quad 1.10$$

which implies that the refractive index of the fundamental and the SHG waves must be equal.

For normally dispersive materials the refractive index increase monotonic with the frequency making thus the condition of the perfect phase match for the production of SHG impossible. However, by taking advantage of the birefringence of some materials, it is feasible the condition of the perfect phase match is satisfied. Birefringence is the dependence of the refractive index value on the polarization direction of the radiation that some materials (mainly crystals) presented. For that reason for normally dispersive material that present high enough birefringence the fundamental and the SHG waves propagate always with different polarization directions. Nevertheless, for biological samples which they do not exhibit the

strictly periodic structure of the above crystals, SHG can be produced under the so-called quasi-phase-matching conditions. The three most common cases of biological materials that efficiently emit SHG are: collagen, myosin, and tubulin.

The described requirements in order to be produced SHG briefly depicted in the following figure.

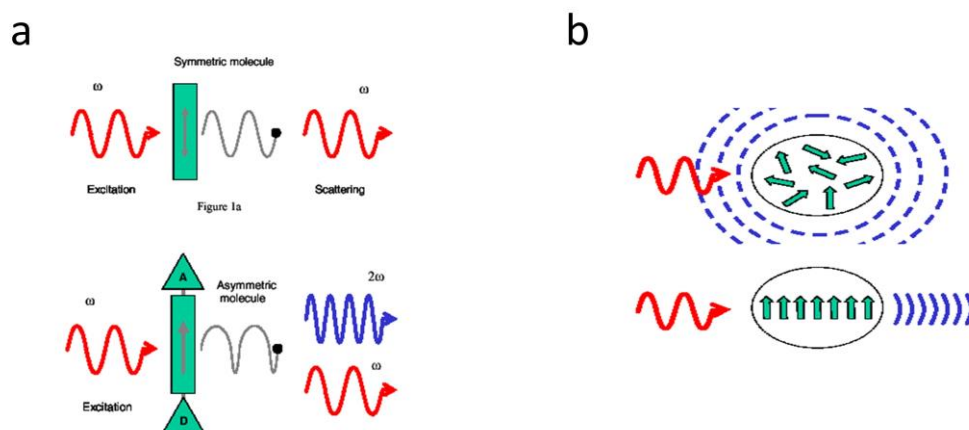


Figure 1.10 : a) Electron response (gray line) due to incident  $\omega$  frequency radiation (left red line) for a symmetric and asymmetric uni-axial molecule. In the asymmetric molecule's case, the break of the symmetry was caused by the existence of electron donors (D) and acceptors (A) moieties at the opposite ends of the molecule, whereas the blue line corresponds to the scattered light component with  $2\omega$  frequency. b) Scattered  $2\omega$  frequency radiation (blue lines) from randomly and well-aligned asymmetric molecules (the dashed line denotes the incoherence of the phenomenon). [3]

When driven by light of frequency of  $\omega$ , the induced electron motion in a symmetric uni-axial molecule produced Rayleigh scattering at the same frequency  $\omega$  (Figure 1.10a). The absence of  $2\omega$  frequency component is due to the fact that  $\chi^2$  coefficient is zero for symmetric uni-axial molecules and the same holds for the centrosymmetry case in the 3D space [1]. For an asymmetric molecule,  $\chi^2$  is not zero and the induced accelerated electron motion produces scattered light at frequencies  $\omega$  and  $2\omega$ . The latter is called Hyper-Rayleigh scattering (HRS).

Except for the lack of symmetry and centrosymmetry for 1D and 3D molecule's respectively, in order to be produced SHG from a population of N molecules they must be well-aligned to each other. In that case, the HRS contribution of each molecule is coherent leading to enhancement of the total radiation which propagates along the same direction as the driving field (Figure 1.10b).

This radiation is the well-known SHG and its total power scales as the square of the number of scattering molecules. Otherwise, if the asymmetric molecules are randomly oriented, interact incoherently with the electric field and the total HRS radiation propagates uniformly all over the directions, while its total power is simply proportional to the number of the molecules. In addition, it must be emphasized here that, if a sample is well organized like just described for the production of SHG it is sure that also presents birefringence and the fast axis of this sample would be parallel to the electron donor-acceptor axis [3]. Reminded that for normally dispersive materials the only way to be achieved the perfect matching condition in order to be produced sufficiently SHG is when the material presents birefringence.

On the other hand, the sufficient production of THG (as Figure 1.9b shows) requires positive values for phase mismatch. Despite that some crystals present high enough birefringence in order to be achieved this positive mismatch [44], in practice, detectable THG arises from optical inhomogeneities, such as interfaces between two mediums, of size comparable to the beam focus [45]. Thus this modality is extremely sensitive to probe refractive indexes changes and provide sub-micrometer structural and morphological information.

### 1.5 Polarization-depended SHG (PSHG) Theory

In this section, the dependence of the SHG signal from the laser polarization will be analyzed. The analysis is based on the assumption that the second order polarization from Equation 1.5 of the medium induced from the laser has only vertical to the direction of the laser propagation components. This assumption is absolutely true in the case where the radiation entering the medium is a planar wave, but is a reasonably good approximation even in the case of a focused beam [46][47]. Under that approximation, the intensity of the SHG produced from the laser ( $I^{2\omega}$ ), which is proportional to the square of the induced polarization of the medium, can be written in the next form:

$$I^{2\omega} \sim |P_Z^{2\omega}|^2 + |P_Y^{2\omega}|^2 \quad 1.11$$

The Z, Y subscripts of Equation 1.11 referred to the laboratory coordinate system XYZ with the X-axis being the propagation axis of the laser. As discussed in the previous section the second order induced polarization described by the third rank tensor  $\chi^{(2)}$ . However, in the case of SHG,  $\chi^{(2)}$  can be written in a compressed form of a 3x6 matrix as[1]:

$$\chi^{(2)} = \begin{matrix} & \chi_{11} & \chi_{12} & \chi_{13} & \chi_{14} & \chi_{15} & \chi_{16} \\ \chi^{(2)} = & \chi_{21} & \chi_{22} & \chi_{23} & \chi_{24} & \chi_{25} & \chi_{26} \\ & \chi_{31} & \chi_{32} & \chi_{33} & \chi_{34} & \chi_{35} & \chi_{36} \end{matrix} \quad 1.12$$

determining thus the produced second order polarization  $P^{2\omega}$  by an external electric field  $E^\omega$  with the following way:

$$\begin{matrix} P_x^{2\omega} \\ P_y^{2\omega} \\ P_z^{2\omega} \end{matrix} = \begin{bmatrix} \chi_{11} & \chi_{12} & \chi_{13} & \chi_{14} & \chi_{15} & \chi_{16} \\ \chi_{21} & \chi_{22} & \chi_{23} & \chi_{24} & \chi_{25} & \chi_{26} \\ \chi_{31} & \chi_{32} & \chi_{33} & \chi_{34} & \chi_{35} & \chi_{36} \end{bmatrix} \cdot \begin{matrix} E_x^\omega E_x^\omega \\ E_y^\omega E_y^\omega \\ E_z^\omega E_z^\omega \\ 2E_y^\omega E_z^\omega \\ 2E_x^\omega E_z^\omega \\ 2E_x^\omega E_y^\omega \end{matrix} \quad 1.13$$

where x,y,z subscripts of P and E referred to the sample's coordinate system. Via the expression of P and E in this coordinate system is feasible in the case where the sample possesses some kind of symmetries the  $\chi^{(2)}$  to be simplified even more. For example, the simplest form that  $\chi^{(2)}$  can take corresponding to a centrosymmetric sample, is the one where all the elements are equal to zero. In other words, a centrosymmetric sample is unable to produce SHG. So, the lack of centrosymmetry and the birefringence of the material are the two main conditions that a sample must fulfill in order to produce SHG.

The second order polarization tensor  $\chi^{(2)}$  can be simplified greatly in the case where the sample presents cylindrical symmetry along one major axis as the next Equation shows:

$$\chi^{(2)} = \begin{matrix} 0 & 0 & 0 & 0 & \chi_{31} & 0 \\ 0 & 0 & 0 & \chi_{31} & 0 & 0 \\ \chi_{31} & \chi_{31} & \chi_{33} & 0 & 0 & 0 \end{matrix} \quad 1.14$$

Biological structures that have this kind of symmetry are collagen and myosin filaments. Except that the most elements of  $\chi^{(2)}$  from the above Equation are zeros it is interesting that some of the remaining are not independent of the others. In fact, the only two independent and non-vanishing  $\chi^{(2)}$  elements in the case of a cylindrical symmetric sample are  $\chi_{31}$  and  $\chi_{33}$ . Moreover, in this case, the induced polarization can be computed through Equation 1.13 and 1.14. Afterward, by expressing this polarization to the laboratory coordinate system and using Equation 1.11 it turns out that the total SHG signal is proportional to[48]:

$$I^{2\omega} \sim [\sin(2(a-f))]^2 + [B\cos(a-f)^2 + \sin(a-f)^2]^2 \quad 1.15$$

Equation 1.15 is one of the main equations for the PSHG analysis since it relates the modulation of the recorded SHG signal in respect to the rotation angle  $a$  of laser linear polarization. Angle  $f$  is the angle between the initial polarization of the laser and the projection of the sample's symmetry axis onto the polarization plane.  $B$  is known as anisotropy parameter, and is a function of the ratio of the only non-vanishing and independent sample's  $\chi^{(2)}$  elements which its symmetry axis forms an angle  $\delta$  with the laser propagation direction.

$$B = \frac{\chi_{33}}{\chi_{31}} \cdot \sin^2(\delta) + 3 \cdot \cos^2(\delta) \quad 1.16$$

In the macroscopic point of view,  $B$  can be expressed as the ratio of the SHG electric fields when the linear polarization is parallel ( $a-f=0^\circ$ ) and perpendicular ( $a-f=90^\circ$ ) to the sample's symmetry axis

$$B = \sqrt{\frac{I_{SHG}^{\parallel}}{I_{SHG}^{\perp}}} = \frac{E_{SHG}^{\parallel}}{E_{SHG}^{\perp}} \quad 1.17$$

Furthermore, the ratio  $\chi_{33}/\chi_{31}$  is also related with the effective angle  $\theta_e$  which is the most probable angle between the SHG emitters and sample's symmetry axis. In cases like myosin and collagen the effective angle  $\theta_e$  is in agreement with the pitch angle of their helices[49]

$$\cos^2(\theta_e) = \frac{\frac{\chi_{33}}{\chi_{31}}}{2 + \frac{\chi_{33}}{\chi_{31}}} \quad 1.18$$

Another sample where the effective angle  $\theta_e$  resulting from PSHG experiments is in agreement with the helix pitch angle on which the emitters are arranged on is starch granule[50].

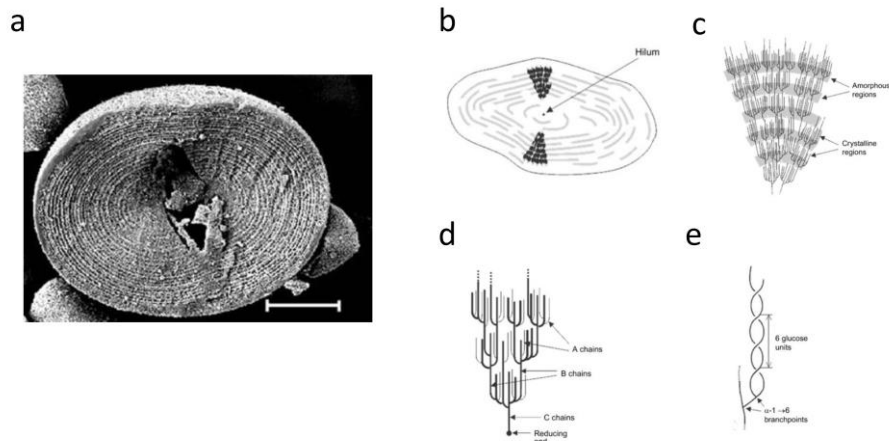


Figure 1.11 : a) Cross-section of a starch grain, showing their three-dimensional shape whereas the scale bar represents  $5 \mu\text{m}$  [51]. b) Orientation of the amylopectin molecules in a cross section of an idealized granule. c) Amorphous and crystalline regions of the amylopectin structure. d) General structure of amylopectin. e) Double helix structure that produce the extensive degree of crystallinity in granule [52].

As Figure 1.11 shows the amylopectin molecules, which are the source of SHG from a starch granule sample[53]. These molecules are oriented radially inside the starch granules. For that reason starch granule samples provide valuable information about the state of the laser's polarization (e.g. orientation and the linearity degree) at the focal plane [54].

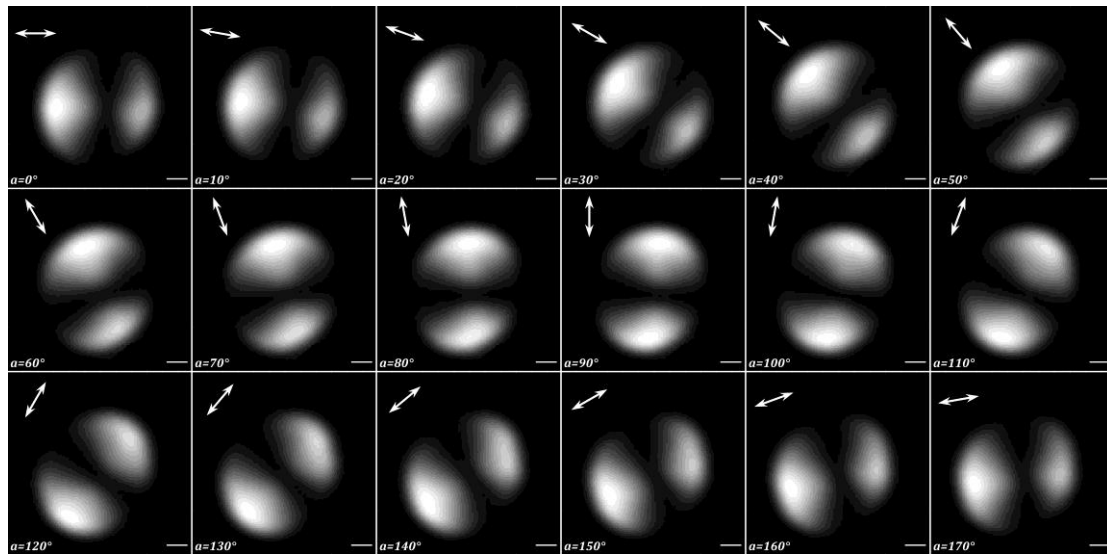


Figure 1.12 : SHG images recorded via the NLOM setup of this thesis from the same starch granule area during the rotation of the laser's linear polarization. At the bottom left depicted the value of angle  $a$  of Equation 1.15 whereas the white double-headed arrow on the top left of each subfigure shows the corresponding direction of the laser's polarization. The scale bars represent  $5 \mu\text{m}$ .

The illustration of the laser's polarization direction in Figure 1.12 based on the two bright lobes that the sample presented. As mentioned before, the anisotropy parameter  $B$  of a sample can be seen, in a macroscopic point of view, as the ratio of the produced SHG electric fields when the linear polarization of the laser is parallel and perpendicular to the emitters' symmetry axis. The estimated  $B$  value via PSHG experiments for starch granule sample is

centered to 3.7[50]. Since the depicted area of Figure 1.12 corresponds to a middle cross-section of the granule it can be assumed that angle  $\delta$  is  $90^\circ$ . In this case anisotropy parameter  $B$  is equal to  $\chi_{33}/\chi_{31}$  ratio (Equation 1.16) and through Equation 1.18 results that the effective angle of SHG emitters to their symmetry axis ( $\theta_e$ ) is  $36.1^\circ$ . This value matches with the helical pitch angle obtained via x-ray scattering experiments[55]. Indeed, the measured amylopectin molecule radius  $R$  and helical pitch  $P$  found to be equal to  $2.75 \text{ \AA}$  and  $5.38 \text{ \AA}$  respectively, which through the next equation resulting a helical pitch angle  $\theta$  equals to  $38.89^\circ$ .

$$\tan(\theta) = \frac{2\pi R}{P} \quad 1.19$$

Since the anisotropy parameter value of a starch granule sample is about 3 times greater than the unit it is expected that the direction of the two bright lobes that appearing in SHG images will be parallel to the laser's linear polarization. In addition, due to the radial distribution of the amylopectin inside the granule and the linear polarization of the laser the two bright lobes follow the rotation of the polarization which performed via the implementation of a half-wave plate in the direction of the excitation beam. For these reasons, a starch granule sample was used during this thesis in order to visualize and verify the polarization state at the focal plane.

## 1.6 NLOM setup

In this section, it will be presented a general overview of the setup from which all nonlinear data of this thesis came from. This custom made setup located at the nonlinear microscopy lab (NLM) of Dr. George Filippidis at IESL/FORTH. The detailed specifications from some of the components will be presented in the following chapters since they change depending on the demands and the needs of the experiments.

One of the main components of the NLOM apparatus was a femtosecond pulsed laser with high enough output instantaneous intensities to produced detectable nonlinear signals (SHG, THG, MPEF) from the specimens. In the framework of this thesis two different fs excitation sources are used, one diode pumped (t-pulse) and one with fiber based oscillator. The specifications of these lasers was 1028 nm wavelength, 50 MHz repetition rate, 200 fs pulse duration, 1 W output power and 1064 nm wavelength, 80 MHz repetition rate, 150 fs pulse duration, 5 W output power respectively. Most of the setup peripherals were adapted on a modified Nikon upright microscope (Nikon Eclipse MED600D). The power at the focal plane can be adjusted with use of intensity filters in front of the laser output. Moreover, in order to be ensured a high degree of the laser linear polarization a linear polarizer is placed just after the intensity filters. In some experiments there is a phase retardation wave plate (WPH05ME; Thorlabs, Newton, New Jersey, USA) with which it is possible the rotation of the laser polarization by a specific angle (this is the angle  $\alpha$  of Equation 1.15). Silver mirrors (5103; New Focus, Irvine, California, USA) which consist a periscope drive the laser beam into a pair of galvanometric mirrors (6210H; Cambridge Technology, Bedford, Massachusetts, USA). With these galvanometric (galvo) mirrors, it is feasible a raster scanning with the laser beam of areas up to  $200 \mu\text{m}^2$ . In addition a telescope system, consists by two converging lenses is employed for obtaining the detected scanning regions and fulfill the back aperture of the objective lens. The utility of the telescope is to expand the laser beam diameter in order to take advantage of the whole of the following objective lens's numerical aperture leading thus

close to a diffraction limited focused beam. Just before the objective lens, there is a mirror that turns the laser beam path by 90° and there is the option to be dichroic in cases where the acquisition of the reflected nonlinear signal is required. Two different objective lens were used in the experiments of this thesis, one air immersion (Carl Zeiss, Plan Apochromat, 20x, 0.80) and the other water immersion (Carl Zeiss, C-Achroplan, 32x, 0.85). The focal plane as well as and the desired area for the raster scanning of the sample selected by a three axis translation stage, on which is mounted the sample's base, whereas the motion gives by stepper motors (Standa Ltd. 1µm minimum step). The produced nonlinear transmitted signal collected from a condenser lens (Carl Zeiss, PlanNeofluar, 40x, 0.75 NA, air immersion) below the sample's base and delivered it to a UV-enhanced aluminum mirror (PF 10-03-F01; Thorlabs). At the end, the signal reaches the PMT's entrance (H9305-04, Hamamatsu, Hamamatsu City, Shizuoka, Japan) after passed through appropriate filters based on the desired to be measured nonlinear signals. In addition, this custom-built imaging setup provides the ability to lighting the sample with an illumination source (white lamp) and observe it through a CCD sensor (PLA662; PixeLINK, Ottawa, Ontario, Canada) attached to the camera port of the microscope. Furthermore, it is feasible the reflected nonlinear signal to be collected from the objective and passed through the dichroic mirror reaching a second PMT adapted to the eyepieces port of the microscope after again a proper spectral filtering.

The galvo-mirrors and the PMTs are connected to a connector block (BNC-2110; National Instruments, Austin, Texas, USA), which is interfaced to a PC through a DAQ(PCI 6259; National Instruments). The synchronization of the PMTs, galvo-mirror, and the translation stage in order to perform all the experiments achieved through LabView software (National Instruments) programs. Finally, a typical duration time for one raster scanning images with 500x500 pixels and up to 200x200 µm<sup>2</sup> lasts about one second.

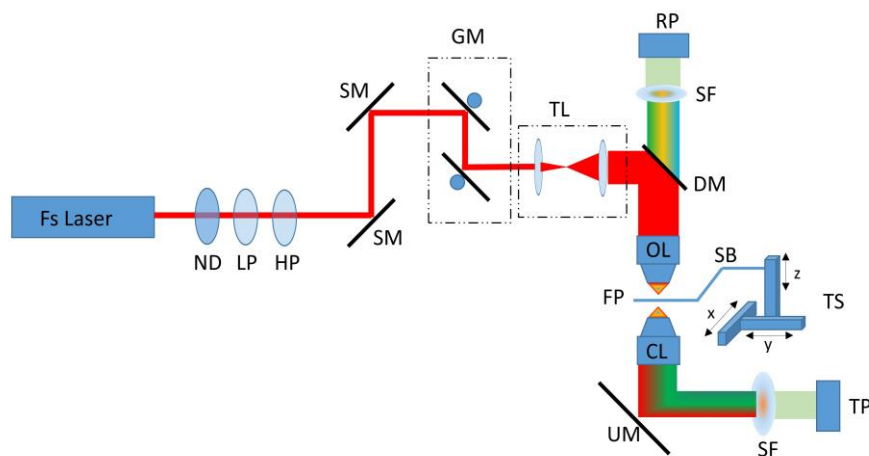


*Figure 1.13 : Schematic representation of the setup. Abbreviations: Neutral Density filters (ND), Linear Polarizer (LP), Half wave retardation plate, Silver coated mirrors (SM), Galvo mirrors (GM), Two converging lenses telescope (TL), Dichroic mirror (DM), Objective Lens (OL), Focal plane (FP), Condenser Lens (CL), UV-enhanced aluminum mirror (UM), Spectral filters (SF), Transmission PMT (TP), Sample's Base (SB), Motorized stage (XYZ) (TS), Reflection PMT (RP).*

The resolution of a NLOM setup, depends on the effective volume of the spot, which is defined as the volume of the focused beam within which there are high enough intensities to produce the corresponding nonlinear signal. In the diffraction limit where no aberrations taking account, the radius  $r$  of the spot at the focal plane equals to [56]:

$$r = 0.61 \frac{\lambda}{NA} \quad 1.20$$

where  $\lambda$  is the wavelength of the laser and NA the numerical aperture of the objective lens that focused the beam. If the induced from the laser phenomenon was linear the Equation 1.20, according to the Rayleigh criterion[57], gives also the lateral resolution of the system. However, in the case of non-linear induced phenomena like SHG, THG, and MPEF the resolution R reduced to:

$$R = \frac{r}{\sqrt{m}} \quad 1.21$$

where m denotes the degree of the non-linearity in the sense of the power dependence of the produced signal to the laser radiation. For example, in the case of THG (m=3), if the laser wavelength is 1028 nm and the numerical aperture of the objective is 0.85, the diffraction limited lateral resolution is about to 426 nm.

Following the same approach with the lateral resolution the diffraction limited axial resolution of NLOM setup can be calculated through the next equation,

$$R_{axial} = \frac{n \cdot \lambda}{NA^2} \cdot \frac{1}{\sqrt{m}} \quad 1.22$$

where n is the refractive index of the material into which the laser beam is focused. Since one of the main components of the biological samples is the water, it is a reasonably good choice for n to be assumed equal to water's refractive index ( $n_{water}=1.33$ ). By replacing the values of the previous example's variables (m=3,  $\lambda=1028$ , NA=0.85) into Equation 1.22 resulting that the diffraction limited axial resolution is close to 1.9  $\mu\text{m}$ .

## Chapter 2 - THG as a new diagnostic tool for discrimination of breast tissue biopsies samples

### 2.1 Introduction

Breast cancer is one of the most common malignancies in the female population worldwide, caused by a combination of genetic and environmental factors, while displaying different phenotypes according to the pathophysiology of each patient [58]. Breast cancer encompasses a heterogeneous array of tumor cell types that are classified according to their histological and molecular characteristics into at least four subtypes, each one associated with a different prognosis and course of treatment. Although molecular markers, such as hormone receptors, HER2 and Ki67 have been used for tumor classification, prognosis prediction as well as the choice of treatment protocol cannot be effectively applied to all patients. The lack of specific tumor markers for evaluating the exact grade of disease for all patients highlights the necessity of developing new tools for the reduction of patients' recalls and unnecessary biopsies, while maintaining or even improving the current cancer detection rates. Indeed, in spite of marker expression, cancer cells share common features in the context of activation, increase or energetic pools, dynamic nuclear activity, which could be universally applied for diagnosis. Ideally, novel non-invasive methods for unanimous cell evaluation and fast decision-making therapeutic strategies are required.

Until now, non-linear optical modalities, such as MPEF, SHG and THG have been applied to detect responses to neoadjuvant therapies for cancer[59]–[61] and to define surgical margins in tissues [59], [62], [63]. Commonly to other non-linear imaging techniques, THG not only enables recording of label-free images without causing photobleaching and phototoxicity effects on the biological samples, but it also allows quantitative analysis [64]–[68]. Of note, THG signal can be enhanced by the presence of multilayered structures detected in membranes, lipid bodies [69] and inhomogeneities.

In the present research THG microscopy was employed for accurate imaging and signal quantification in breast cancer tissues. Indeed, at the cellular level THG signal has been largely correlated to lipid bodies (LBs) [65], [69], which are highly dynamic and functional cellular organelles, actively involved in inflammation and cancer[70]. Thus, THG utilized to shed light on cancer research as a novel imaging diagnostic tool for differentiating malignant from benign breast tissue samples and discriminating among the different grades of cancer[71]. Two different approaches for data analysis were followed, a simple time consuming manual based analysis and a faster via the application of a deep-learning technique to the obtained nonlinear images. The first approach (manual analysis) was part of the PhD thesis of Dr. Gavgiotaki.

### 2.2 Manual based analysis of THG images

#### 2.2.1 Materials and Methods

Setup: The nonlinear signals for this study produced by the diode pumped laser. The energy per pulse at the sample plane was 0.4nJ and a high numerical aperture objective lens (Carl Zeiss, C-Achroplan 32x, NA 0.85, water immersion) was employed for the tight focusing of the laser beam onto the sample. For wide scanning regions (~mm) a synchronized movement

of galvo mirrors with the xyz stage was performed through a specially designed LabView program. SHG & MPEF signals were collected in the backward direction using a photomultiplier tube (PMT Hamamatsu R4220, Hamamatsu city, Japan). A bandpass interference filter (CVI 514 nm) was placed at the PMT input to cut off the reflected laser light and solely detected SHG signals from the samples. The short bandwidth of the filter (3nm) used herein, verified that only a minimal amount of fluorescence signals can be detected as an extremely weak constant background. In case of MPEF, a short pass filter (SPF 700 nm, CVI Laser, Albuquerque, New Mexico) and a notch filter (NF 514-17 Thorlabs, Germany) were placed at the PMT input for the detection of fluorescence signals from the samples. SHG and MPEF signals were recorded in distinct set of measurements. THG signals were detected simultaneously in the forward direction, by employing a colored glass filter (U 340nm Hoya, UOG optics, Cambridge, UK) and a second PMT (Hamamatsu H9305-04, Hamamatsu city, Japan). As mentioned in the last section of the previous chapter a typical time duration for obtaining a 2-D 500x500 pixels non-linear image is one second, whereas for large scanning areas, a 2D 1x1mm image could be acquired in 100 sec. To improve the signal to noise ratio (SNR) of the small areas ( $45 \times 45 \mu\text{m}^2$ ), 20 scans were realized for each sample plane. A series of 2D optical sections for these areas were obtained at 1  $\mu\text{m}$  intervals (z stack) and projected (maximum intensity projection) onto a single plane. The depth of scanning was dependent of the tissue width (~10 slices covered the whole sample). Image J software was used for data viewing and processing (NIH, <http://imagej.nih.gov/ij/>).

**Biological samples:** Benign (control) and cancerous tissues were obtained from a total of 15 patients, including 2 cases of benign bearing tumor (grade 0, ductal carcinoma), 4 patients with grade I tumor, 5 patients with grade II tumor and 4 patients with grade III tumor. All patients were older than 60 years of age. The experimental protocol was approved by the Ethics and Scientific Committees of the University Hospital of Heraklion (IDs 16/16-10-2019 (579) and 4428/10-07-2019; Crete, Greece). All methods were carried out in accordance with relevant guidelines and regulations.

Tissue samples were embedded in paraffin, sliced in 5-10  $\mu\text{m}$ -thick histological sections and routinely stained with hematoxylin and eosin (H&E) for optical microscopy examination [72]. For non-linear imaging, unstained tissue slices were placed on special very thin (0.07mm) round glass microscope slides of 3.5cm diameter to provide a flat sample surface. Moreover, H&E images of serial sections of the same sample were recorded for evaluation and comparison with the non-linear data. Tissue sections were in some cases stained with Nile red (Sigma-Aldrich Co., MO, USA) according to the manufacturer's instructions for the detection of lipid bodies.

**Data analysis:** For the identification of the cells in the tissue (cell segmentation), a scanning region of  $45 \times 45 \mu\text{m}^2$  was selected from a larger field of view (Figure 2.1) and images were collected from the whole tissue volume of the regions (3-D images). This scanning region was selected to identify the cells and study the intracellular structures.

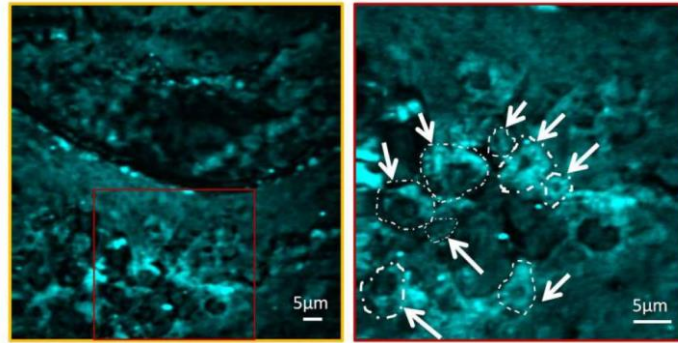


*Figure 2.1 : 2D THG images of different field of views (FOV) left image  $90 \times 90 \mu\text{m}^2$  and right image  $45 \times 45 \mu\text{m}^2$  of breast cancer grade II. Red square represents the area that is zoomed in the right picture. White arrows in the right picture indicate some of the cells that were manually segmented.*

This selection was assisted and verified with the white light observation of the same investigated area and the information derived from the sequential H&E slice images of the tissue. The cells could be identified through the 3D dimension of the tissue. In particular, 3D obtained THG images revealed the margins between the cells due to the inhomogeneities (membranes) as well as the black central area corresponding to the nucleus.

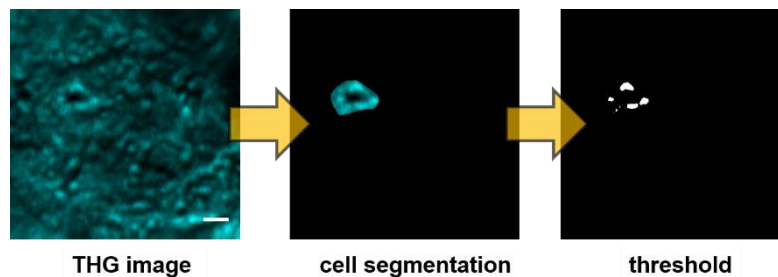


*Figure 2.2 : Illustration of THG tissue processing. Manual isolation of individual cells for quantification analysis (based on LB content, inhomogeneities and membranes). The threshold was set in a way to allow the higher THG signal that indicates mainly inhomogeneities and lipid content of the cell area to be analyzed and measured. [71]*

After the optically isolation of the cells from each sample like presented in Figure 2.2 follows the quantification processing which includes the calculation of each cell volume, the mean THG area of each cell and the mean THG intensity signal of the tissue area. Quantification of the THG signal was accomplished by setting a threshold that allows the higher THG signal to be analysed. The volume of each cell was calculated by measuring the surface of the cell of each slice and then multiplying by the number of slices of the tissue that was evaluated. This manual analysis was performed by Dr. Gavgiotaki.

### 2.2.2 Results

In an effort to examine whether THG imaging could distinguish malignant from healthy cells within breast tissues and provide information as to the severity of tumor invasion, the aforementioned paraffin embedded sections were submitted to qualitative and quantitative non-linear imaging.

Breast tissues from benign (grade 0) and grades I, II and III malignant tumors were submitted to multimodal non-linear imaging. The applied technology integrates non-linear processes,

such as SHG and THG into a single, unified microscopy platform, providing thus complementary structural information within individual cells at the submicron level. Using a single beam, without the need of staining, information on inhomogeneities (mainly membranes and LBs, THG), as well as collagen distribution (SHG) could be visualized (Figure 2.3). Indeed, as shown in Figure 2.3,(Grade I sample) inhomogeneities and structural information (THG cyan) and collagen distribution (SHG red) were easily detectable via nonlinear imaging and compared to H&E staining from a sequential tissue section.

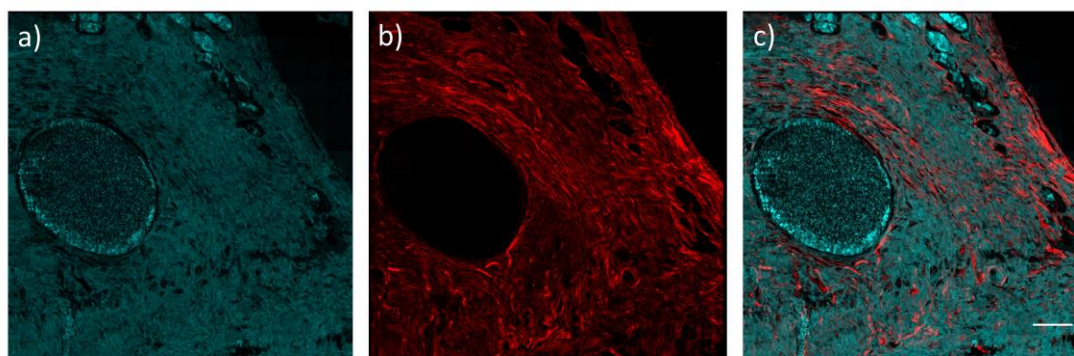


*Figure 2.3 : Characteristic multimodal non-linear image of a grade II sample (c) consisting of a THG image (a) and a SHG image of the same tissue area (b). Scale bar depicts 100  $\mu\text{m}$ .*

During the present thesis, the experimental setup optimized allowing to scan increased region areas of the tissue at the order of  $\sim\text{mm}^2$ . Figure 2.4 is a result of 100 images whereas the size of each one was  $100 \times 100 \mu\text{m}^2$ . These images were recorded by a specially designed LabView program in order to minimize any side effects, such as the backlash of the stepper motors when changing direction and at the same time to provide a small overlap area for each image with its neighbors. Taking advantage of this overlap a program was developed in MatLab, takes-over to “sticking” correctly these images and to create the final big image area. This modality is very useful in our studies since it offers a general overview of the tissue for the appropriate selection of the areas that will be zoomed for quantification analysis.

In Figure 2.4 THG signal clearly showed increased intracellular inhomogeneities and lipid bodies, with tumor progression, benign (grade 0) to grades I, II and III malignant tumors. At the same time, SHG signal that detects collagen fibers, showed that although in grade 0 tissues collagen orientation was well structured with specific continuity, in grades I, II and III collagen gradually disoriented and became less and less apparent [73]–[75].

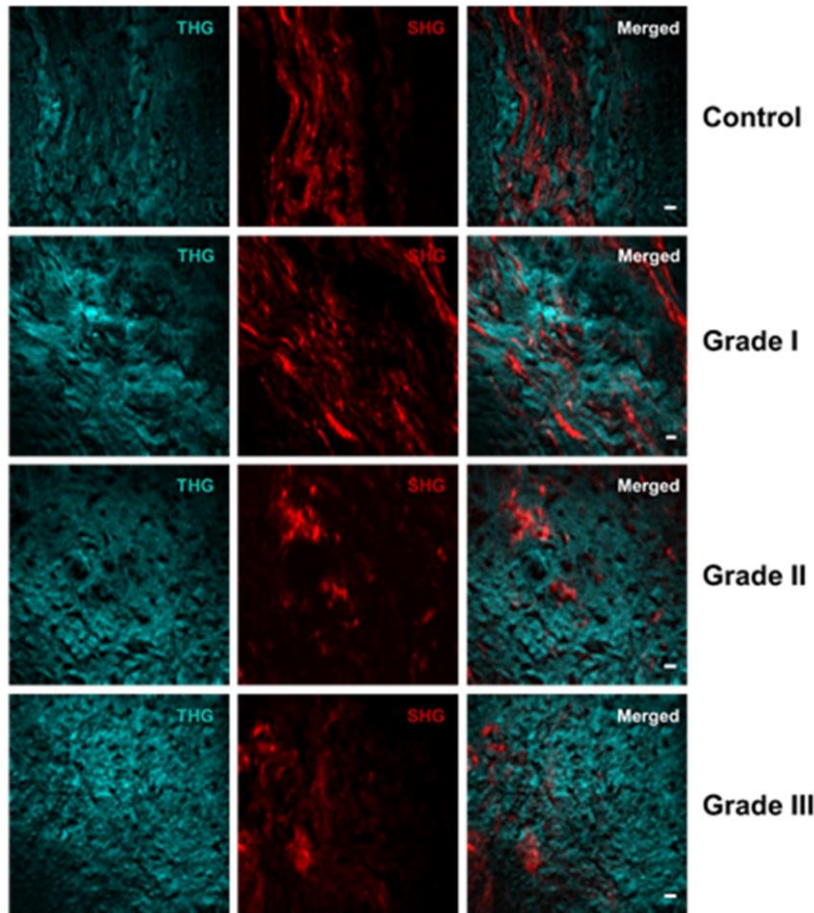


Figure 2.4 : Non-linear images (SHG & THG) of benign (grade 0) and malignant (grade I, grade II, grade III) breast tissues. THG images (cyan) of tissues show intracellular inhomogeneities, while SHG images (red) indicate collagen (scanning area  $\sim 150 \mu\text{m}^2$ ). Third column shows the multimodal (THG and SHG) images. Scale bar of non-linear images depicts  $5 \mu\text{m}$ .

In this manual analysis of the THG signals, via the isolation of individual cells, the classification of tissues based to their THG mean area, THG intensity and cell volume was investigated.

Because of the heterogeneous structure of breast tissue, the efforts to predict the behavior of the different lesions are limited to cytomorphology and biological marker analysis. Irregularities in both nuclear shape and size ('pleomorphism'), coupled with changes in chromatin amount and distribution, remain the basic microscopic criteria for a cytologic diagnosis of cancer [76]. Morphologically, tumor cells are characterized by large nuclei of irregular size and shape, prominent nucleoli and reduced cytoplasm areas. The nucleus in neoplastic cells plays a key role in the assessment of tumor malignancy. Changes concerning the surface area, volume, the nucleus/cytoplasm (N/C) ratio, shape and density, as well as structure and homogeneity, serve as criteria in malignancy identification. These features could be easily detected by non-linear imaging without the need of staining[77]. Thus for our quantification analysis, except from THG area intensity and cell volume and the nuclear to cytoplasmic (N/C) ratio values of the isolated cells were calculated.

Combining the results of the mean THG signal area/volume, N/C ratio for a representative number of N=40 cells and THG tissue intensity, an indisputable discrimination of the different grades of malignant samples could be detected (Figure 2.5).

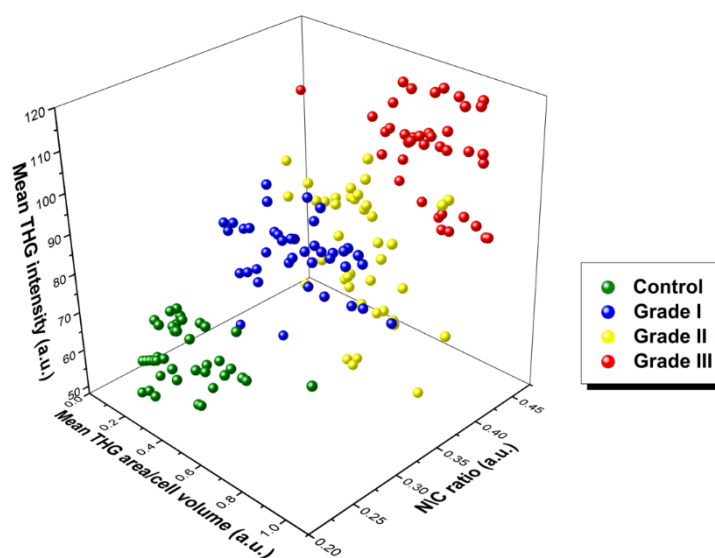


Figure 2.5 : 3D graph for the distinction between cancerous and control (grade 0) tissues via THG signals quantification. Mean THG area / cell volume area in x-axis, N/C ratio in y- axis and THG intensity values in z-axis. The grade III and the control tissues clearly appeared as separable sub populations of spots in the scatter plot (N=40 for each tissue type).

Higher grades of cancerous tissues were showing increased mean THG area, cell volume and N/C ratio, as shown in Figure 2.5. The results presented reports that quantification of THG signals provides a reliable classification as it can differentiate malignant from benign breast tissue samples and segregate the different grades of cancer based on their THG response. This information is crucial and could supplement standard histopathology procedures.

### 2.2.3 Discussion

Non-linear optical modalities such as SHG and THG provided unique morphologically information of breast biopsies, including collagen distribution, intracellular structures and inhomogeneities, using a single laser beam. In benign tissues, cells followed collagen orientation, which was well structured with specific continuity, while the increasing cancer severity correlated with collagen disorientation, which is in agreement with previous studies [73]–[75]. THG imaging also provided the opportunity to calculate the surface area, volume, and nucleus/cytoplasm ratio of tumor cells, which serve as criteria for malignancy identification [77]. Quantification of the THG recorded signal area and volume, which mainly detect intracellular LB structures and inhomogeneities without the need of staining, allowed distinction between benign and malignant tissues (Figure 2.5). The presented findings are in agreement with previous observations showing that THG modality could detect increased lipid profiles in inflammation or cancer [68], [78].

Notably, these data are interrelated to those from clinical diagnostic approaches, since non-linear optical images were comparable to standard H&E staining images, also enabling the analysis of cell size, cell shape, nuclear shape and intracellular organelles without the need of a specific staining. Thus, the unique attributes of non-linear optical microscopy provide promising imaging modalities for disease diagnostics in clinic. A limiting parameter in the

applications of the proposed non-linear technology is the time-consuming, manually, by experienced personnel, THG data analysis. As mentioned previously the manual analysis was part of Phd thesis of Dr Gavgiotaki. However, as it will be presented in the following section, a significant advancement comes from the implementation of neural networks for the fast and accurate analysis of the collected THG images. The methodology that had been developed in the framework of the current thesis could be used for the quick characterization of newly excised unstained thin biopsy samples.

## 2.3 THG image analysis through Neural Networks

### 2.3.1 Introduction to Neural Networks

During the last decade, significant rapid advancements in the area of deep learning have given rise to the so called Deep Learning category of approaches, which revolutionized areas like computer vision, natural language processing and more [79], [80]. Advances in deep learning have enabled the automatic and rapid identification of cancer cells in tissues/organs (segmentation), as well as the categorization of the severity of the disease [81]. Such approaches present a great opportunity for the development of an objective diagnostic tool that will indicate structural changes for prognosis. In the framework of this thesis taking advantage of the deep learning technologies, a convolutional neural network (CNN), which is a type of deep Neural Networks (DNN) and widely applied in imaging tasks model, was developed. It is worth noting that the benefit of using CNN is that it avoids feature extraction from the images since this is part of its training process. We have to note that, it is not possible to know what these features actually represent. However it sure that a CNN uses the whole image and not parts of it for the features extraction. In addition, as the CNN training process is completed, the network is ready to be used by the user who does not need to have any previous relevant experience. The aim of the this section is to present the application of the developed CNN model, in the discrimination of benign versus malignant breast tissue and evaluation of the disease severity, based on the collected THG data from the tissue biopsies. The results presented herein paves the way for the application of novel, non-invasive, label-free optical methods in clinic, which in the future could supplement standard histopathology procedures.

### 2.3.2 Convolutional Neural Networks

For a better understanding of what deep learning and especially what a CNN is, this subsection will provide a general description of its structure and the main components of it[82].

First of all, CNN is an artificial neural network and for that reason, it is important the definition of the single neuron which is the basic entity of any neural network. The mathematical model of an artificial neuron described by:

- input array,  $X$
- weight array,  $W$
- bias,  $b$
- activation function,  $\phi$
- scalar output,  $y$

whereas the next equation shows the way that all these are connected

$$y = \varphi(W^T \cdot X + b) \quad 2.1$$

Equation 2.1 indicates that the output of an artificial neuron  $y$  is the value of the activation function  $\varphi$ , when the argument of the last one, is the summation of bias  $b$  and all the elements of the input array  $X$  after weighted with the corresponding values of  $W$ , where  $T$  denotes the transpose operation.

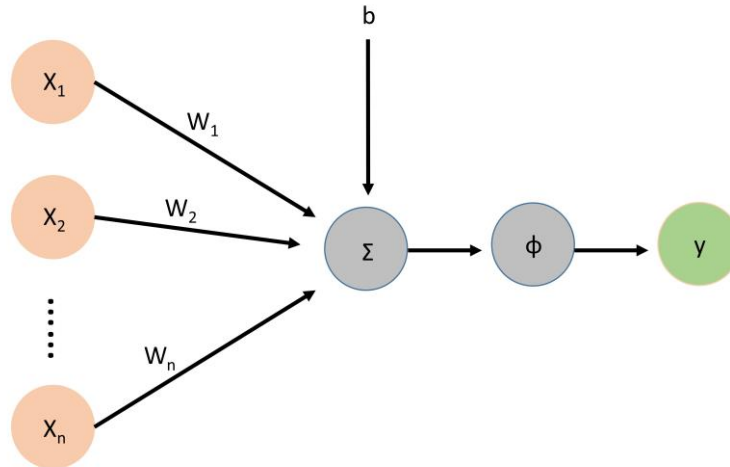


Figure 2.6 : Schematically representation of an artificial neuron based on 2.1.

One of the most popular activation function especially for deep neural networks is the Rectified Linear Unit (ReLU) [83]. The output of the ReLU function is the same as its argument if the argument is not negative and zero if it is. Moreover, another activation function commonly used since the early stages of the CNNs is the softmax activation function [84], which is defined as:

$$y_i = \frac{e^{X_i}}{\sum_{j=1}^n X_j} \quad 2.2$$

As Equation 2.2 shows, the softmax function re-adjust the values of a  $n$ -dimensional vector  $X$  in such a way that the summation of the generated vector  $Y$  elements is equal to the unit. For that reason, the softmax function is suitable to be the final layer activation function of neural network, especially for classification applications. In this case, the values of  $Y$  will represent the probability with which the network predicts that its input will match its  $n$ th category.

The output of the neuron showed in Figure 2.6 can act as input for other neurons leading thus to the formation of a neural network. The simplest structure of neural networks is that of feedforward (FFNN).

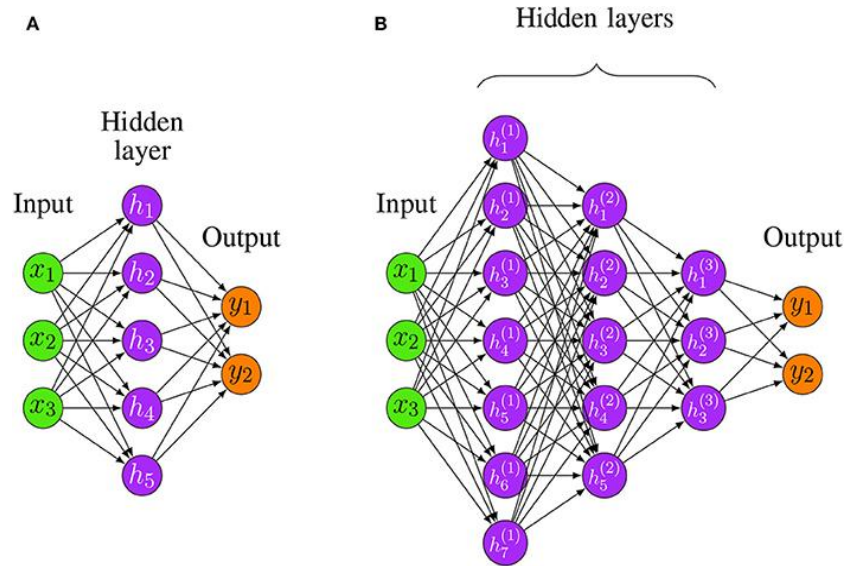


Figure 2.7 : Simplified schematic representation of FFNNs where only the key elements are depicted, i.e., the input, the output, and the weights.

Hidden layers of a neural network are defined between the first (input) and the last (output) one and architectures with more than two hidden layers are commonly considered as deep[85]. In addition, both of the illustrated examples of Figure 2.7 characterized as fully connected since all the elements of one layer act as input to every neuron of the following layer.

Except for the choice of an activation function, which usually is the same for all the neurons of each layer, the only two things that remain to be specified before the training procedure, are the depth of the network and the width of each layer. The depth of a neural network is defined as the total number of its layers except for the first one which is its input, whereas the width of a layer is the number of neurons of which it consists.

After these, the network is ready to be trained through the training dataset. A training dataset consists of a number of  $X$  vectors which for classification applications, such as the present study, have been appropriately labeled. Each vector inserts separately as input to the network and the difference between the output of the network and the label of the vector corresponds to an error. This error back-propagated through the network in order to be minimized by the readjustment of the network's weights. Instead of this readjustment being performed for each input, in most cases, an overall one resulting from a gradient descent optimization algorithm on a batch of the training dataset is preferred. That leads to an increase in the learning speed and the robustness of the training procedure[86]. This minimization process is repeated iteratively until an epoch is completed. An epoch ends when all the batches that assemble the whole training dataset have been used. The number of the epoch must be chosen in such a way that the final network neither under-fitting the training data nor over-fitting them.

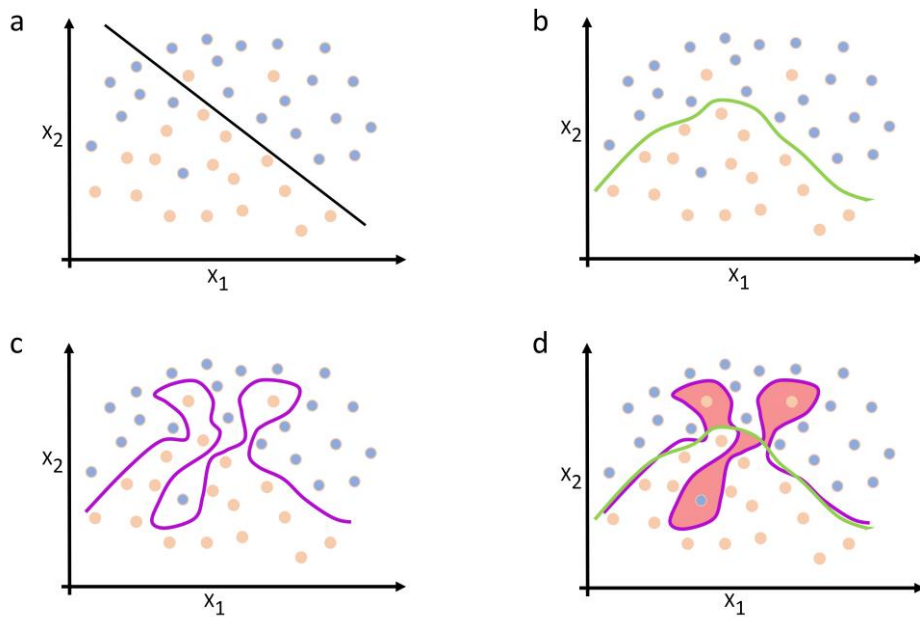


Figure 2.8 : Example of under and overfitting based on a two-class training dataset whereas the color of the cycles corresponds to the label of each two-dimensional datum. a) The black line represents the results of an under-fitted neural network with two outputs (that is, the number of classes of the training dataset). All the new data below that line will be characterized as “orange” class by that model and those above the line as “blue”. b) Results of an optimum-fitted network. The green line represents the predicted from that network boundary between these two classes. c) The same boundary is set by the purple line resulting from an over-fitted network and the pink areas of (d) denote the difference in the predictions of these last two networks.

As reflected in Figure 2.8 neither the under nor the over-fitted networks described sufficiently the two classes. The first one due to a limited number of epochs or trainable weights provide a false oversimplified trend of the data, whereas the second one for exactly the opposite reasons since it affected by the 3 “noisy” data (2 orange, 1 blue), seems to memorize the data instead of learning from them. In the results subsection, it will be discussed analytically how an assessment can be done in order to characterize a model as under or over-fitted.

In addition, all the three networks of Figure 2.8 have the same number of outputs as the number of different classes in which the data is classified. This is something that holds for all classification neural networks. On the other hand, the number of inputs of these networks is the same as the number of features on which the classification is based. In our case, for the classification of THG tissue images in 4 categories corresponding to their different possible grades, a neural network based on the previous section’s analysis should have three inputs N/C ratio, Mean THG intensity, and Mean THG area according to the previous manual analysis.

However, a network like the previous one, wouldn’t provide any reduction to the whole classification procedure time if the manual indication of the cells which is the main time-costly process is not be avoided. As will be shown in a next subsection, it is not necessary to be done the above classification based on structural features of the THG images specified by us. In fact, there is a fast and automatic way for a neural network to classify these images, based on features that have been found by the same network, and this can be done via kernel (convolution) matrices.

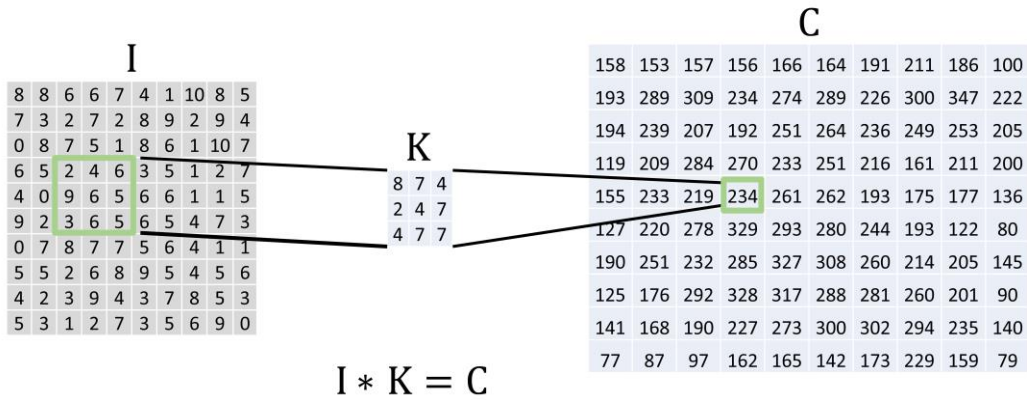


Figure 2.9 : Example of image convolution with an input image  $I$  of size 10 by 10 and a kernel  $K$  of size 3 by 3. The convolved image  $C$  is produced after the center of the kernel passes over all the initial image's pixels. For each position of the kernel's center calculating the corresponding value of the  $C$  matrix pixel. This value defined as the summation of the kernel elements after they have been multiplied point by point with pixels of the initial image  $I$ .

The values of the matrices  $I$  and  $K$  from Figure 2.9 are random since the aim of this example is just to present what a convolution, through kernel matrices, is. In practice, the values of a kernel matrix are crucial because these determine what features will be extracted or what characteristics will be highlighted from a figure after the convolution.

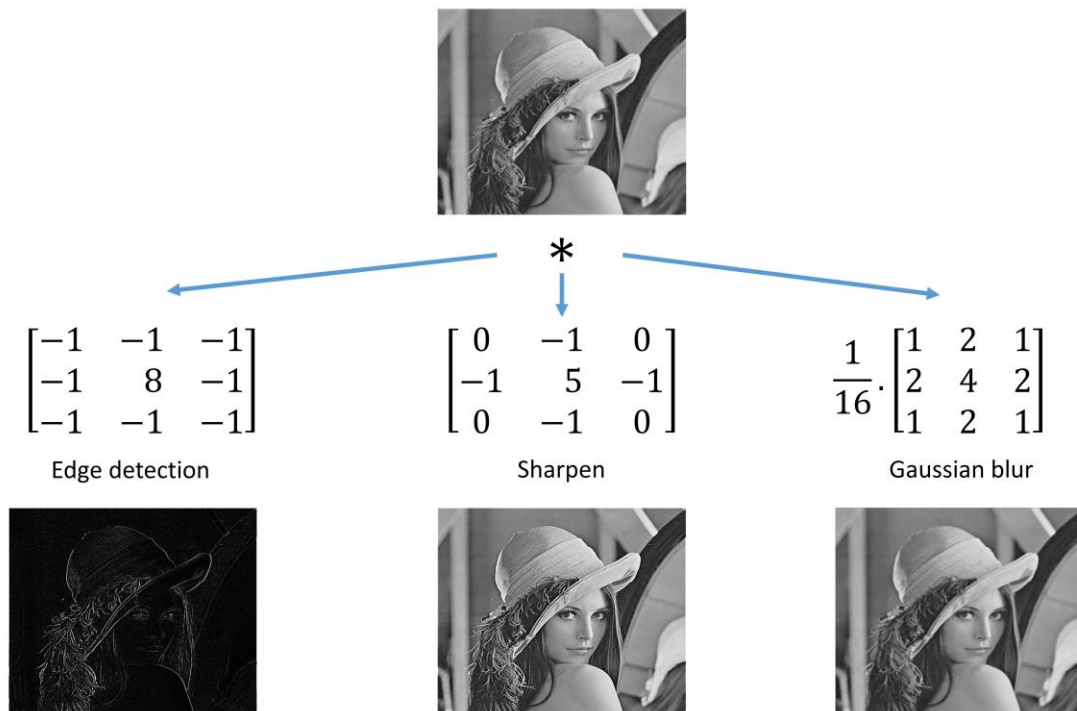


Figure 2.10 : Results of three different convolutions based on the corresponding kernel matrix.

Figure 2.10 confirms that the extracted information from an image after a convolution depends on the values of the kernel matrix that was used which is the main idea behind CNN. The most common CNN architecture for classification applications consists of some

convolutional and a few classical (as described above) layers respectively at the beginning and at the end of it. As input for a neuron at a convolution layer is a 3D matrix whereas the output is a 2D matrix (feature map) produced after the convolution of the input matrix with a 3D kernel matrix and the addition with an extra bias value. The third dimension of the kernel is always the same as the third dimension of the input matrix whereas the outputs of that layer stacked together creating the input for the next one. Afterward, before the generated matrix inserted as input to the next layer its first two dimensions reduced via an appropriate 2D max-pooling filter compressing thus spatially the corresponding feature maps. This reduction is necessary since the results of the final convolution layer, in order to act as input for the first of the classical layers, will be converted to a 1D array with the same number of elements as the 3D matrix. If the number of the elements of this 1D is not significantly smaller than the number of the initial image's pixels there is no need to be used CNN for the reason that the image could also be transformed to a 1D array. However, in practice, a network like that due to the huge unnecessary number of inputs would be very hard and time-consuming to be properly trained as it possesses a high risk of over-fitting.

In conclusion, a CNN for image classification applications learns to extract the appropriate features from the images since the values of all the kernels are trainable parameters and based on these features categorizes the images via the last classical layers. The characteristics of a typical CNN model that was used for the automatic categorizations of THG breast tissue images based on the grade of cancer as well as the training procedure that was followed will be presented in the next subsections.

Several studies have been applying deep learning techniques in mammography interpretation seeking to improve the breast cancer detection success rates [87]–[90]. Moreover, the implementation of CNN models to breast biopsies for precise classification of hematoxylin and eosin stained samples, has been demonstrated [91]–[93]. Most of these methods are binary classifiers that aim to distinguish benign from cancerous tissue, however there are also multiclass algorithms aiming to identify the tumor grade from the tissue under study. A variety of databases is currently available for histopathological stained images for breast cancer that gives to the engineering community the opportunity for continuous development of their methods and direct comparison of the classification performance. Despite the relatively large amount of available data, these works attempt to solve several challenges in digital histopathology including variations in sources of acquisition device, different protocols in stain normalization, as well as the information loss introduced by the down sampling of the original images that is necessary to speed up the network training [91]–[93]. Additionally, the need of tissue processing and staining could alter tissue morphology as well as sub-cellular and extra-cellular structures misleading diagnosis.

In the current thesis only raw THG images, showing discontinuities and multilayered structures detected in membranes and lipid bodies of the investigated samples, were used for the characterization of the different tissue types. Signals were recorded from specimens without further processing or staining.

We mainly focus on multi-regional classification and explore whether grading is possible considering the complex multilayered structures in membranes visualized in THG images and the intra-tumoral heterogeneity observed in breast cancer [94].

### 2.3.3 Methods

Cancer Grade Estimation with Neural Networks: The THG images of the previous section were used to train a DNN in the task of cancer grade estimation, essentially an image classifier with four possible labels as output. A simple CNN architecture was used (see Figure 2.12). The network was trained on some of the acquired images, and its accuracy was evaluated on the remaining images.

Data Pre-processing: As described above, the train and the evaluation data of the neural network were THG images. Figure 2.11 depicts a characteristic THG image recorded from a grade II breast cancer tissue.

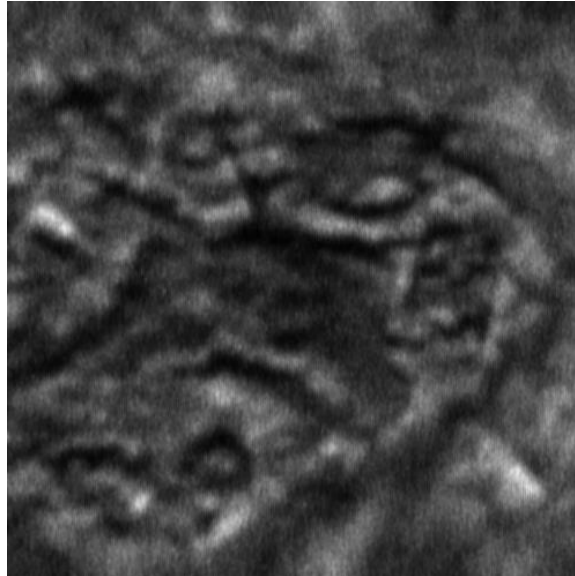


*Figure 2.11 : 2D THG image from a grade II tissue sample (raw data). White color denotes the maximum and black color the minimum THG intensity signals.*

Due to the limited number of data at patient level ( $n=15$ ), we focus mainly on intra-tumoral heterogeneity and explore the performance of our classifier at image-based level. Thus, samples originating from the same patient appear in both the training and validation set. Although the number of patients is limited, data were collected from various regions (at least 10) of each investigated sample for increasing the reliability of this work. The data were normalized to the range  $[0 - 1]$  after excluding extreme recorded PMT values (outliers). The number of the different areas was 210 (32 grade 0, 60 grade I, 72 grade II and 46 grade III respectively). For each area, 10 different z layers at  $1 \mu\text{m}$  distance apart from each other were analyzed. The classification performance of the algorithm was evaluated each time through a cross-validation (CV) resampling approach. In this study, the dataset is split into  $k=10$  folds. Each time, 90% from the total 2100 images were used as training data and the remaining 10% was employed for the evaluation of the developed algorithm. The areas for training or validation of the network were selected randomly while ensuring that all images from an area would be used either for training or validation, but not both. Differences in the successive layer images that may not be observed with simple eye inspection will be explored via the implementation of neural network data processing.

Neural Network Model: A CNN model with six convolutional layers was employed for the analysis of the obtained non-linear images from the tissue biopsies, as illustrated in Figure 2.12. At each convolutional layer a  $3 \times 3$  kernel matrix was used for the features' extraction

(except from the first and last one, where 9x9 and 2x2 kernels were used respectively). The number of the different kernel matrices at each convolution layer was 4,8,16,16,32,32 in order of layer depth. After each convolutional layer, the values of the generated matrices filtered by a ReLU activation function which is the same for all model's layers except the last layer where the softmax was used. Then, the matrices normalized via a batch normalization in order to increase training speed and decrease instability of the model[95]. Furthermore, after each batch normalization layer, the dimensions of the resulting feature maps were halved, using a 2D max pooling layer. The outputs of the last convolutional layer were flattened and fully connected with the 10 inputs of the next layer. The final output layer employed as input the 10 outputs from the previous layer, again in a fully connected manner, and provided 4 outputs, which correspond to our categories (grade 0-III). At the final layer, the 'categorical\_crossentropy' loss was computed and for the training procedure we employed the 'adadelata' optimizer. Our model trained for 400 epochs while the batch size was set to 16. Overall, the trainable parameters of the network were: the parameters of all the convolution kernels, the weights of the fully connected layers, and the Batch normalization parameters.

For avoiding overfitting during training, a data augmentation procedure was employed, using an Image Data Generator. Each image at every epoch was processed with the combination of the following randomized transformations: 0 to 360 degrees rotation, width and height shifts from -20% up to 20% of corresponding size, vertical and horizontal flips.

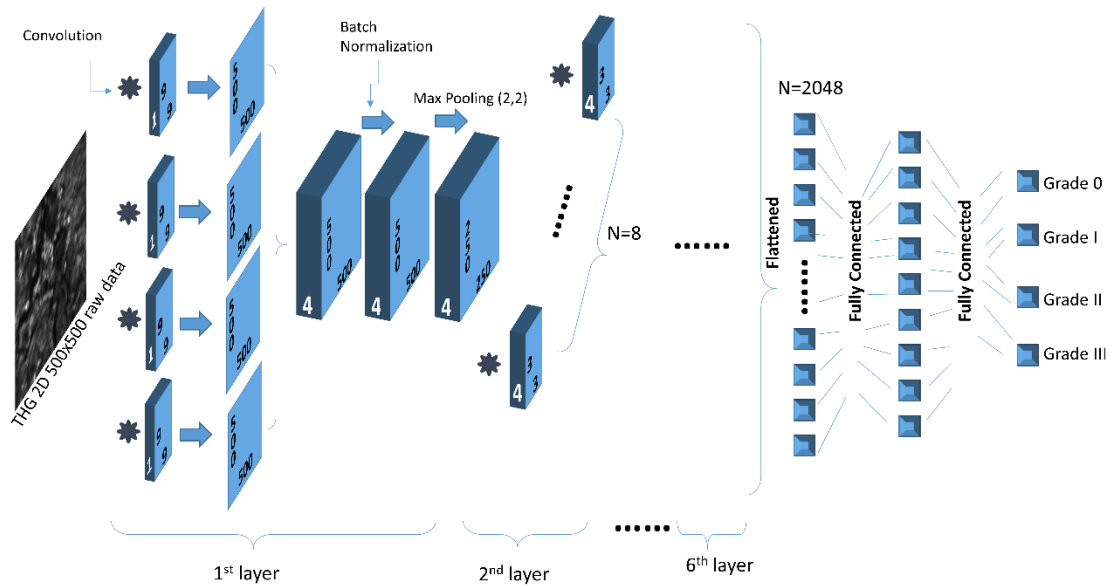


Figure 2.12 : Schematic illustration of the CNN proposed model.

The proposed neural network was implemented using the Tensorflow/Keras deep neural network framework. The experiments were performed using the online platform Google Colaboratory.

### 2.3.4 Results

A total of 2100 THG images were used. The model was tested for its ability to classify the four tumor grades (grades 0-III) at image-based level. A 10-fold CV scheme was implemented to evaluate the performance of the classification task. The performance was evaluated using the accuracy, recall, precision, and F1-score metrics. Whereas accuracy measures the ratio of correctly categorized images to the total validation images, precision

(also called positive predictive value) is defined as the ratio of true positives over the total predicted positives. Recall (also known as sensitivity) is defined as the ratio of true positives over the total actual positives. The F1-score is the harmonic mean of precision and recall. The confusion matrix is also presented. The higher values of the matrix along its diagonal indicate that the predictions of the model coincided with the histological labeling of the tissues as evaluated by the experienced pathologists and provided the ground truth annotation.

In order to assess the performance of the present approach, two more variations of the proposed model (PM); that was described in detail in the Methods subsection were experimented: A simplified version of the model (simplified model, SM), where the last convolutional layer was removed, and a slightly more complex version (complex model, CM), where the number of kernels in the last convolutional layer were 64 instead of 32.

There are both computational and machine learning reasons to vary the degree of complexity of a model. A simpler model is faster to train and evaluate, and at the same time imposes a stronger regularization to the learning task, thus avoiding overfitting, at the risk of not having enough capacity to learn the target task. On the other hand, while a more complex model is slower to train and evaluate, it has a larger learning capacity, at the risk of overfitting to the training data[96]. In the present study, 10-fold CV on the data was applied. Table 2.1 shows the best validation accuracy achieved by each fold, for the three different models. Among the three model variations shown in Table 2.1 for 400 epochs of training, PM exhibited the best mean validation accuracy across the 10 folds, which was equal to  $79.4 \pm 1.6$  (Standard error of the mean ‘SEM’) %. Thus PM is preferable for the correct classification of the recorded non-linear tissue images.

Best accuracy (%)			
Training folds	SM	PM	CM
1	<b>87.1</b>	86.6	85.7
2	78.5	80.0	<b>80.9</b>
3	79.5	<b>85.2</b>	79.5
4	<b>82.3</b>	<b>82.3</b>	71.4
5	72.3	77.6	<b>82.3</b>
6	63.3	69.0	<b>70.9</b>
7	71.9	<b>75.7</b>	70.8
8	65.2	<b>74.2</b>	70.0
9	76.6	<b>80.9</b>	74.2
10	82.3	82.3	<b>87.6</b>
mean	75.9	<b>79.4</b>	77.5
SEM	2.3	<b>1.6</b>	1.9

*Table 2.1 : Best validation accuracy during 400 epochs training of three different CNN models for a 10-fold cross validation. PM has 6 convolution layers with 4,8,16,16,32,32 kernels respectively at each layer. SM has one convolution layer less so the number of kernels are 4,8,16,16,32. Finally, CM has 6 convolutional layers, however the number of the kernels in the last convolutional layer is equal to 64 instead of 32 compared to the PM. Bold indicates better performance.*

It is interesting to note that the PM model showed the higher average accuracy and at the same time the lower standard deviation values, which indicates that PM achieves the maximum possible accuracy among similar network architectures.

Representative results of the PM for one fold from the previous CV presented in Table 2.1 are shown in Figure 2.13.

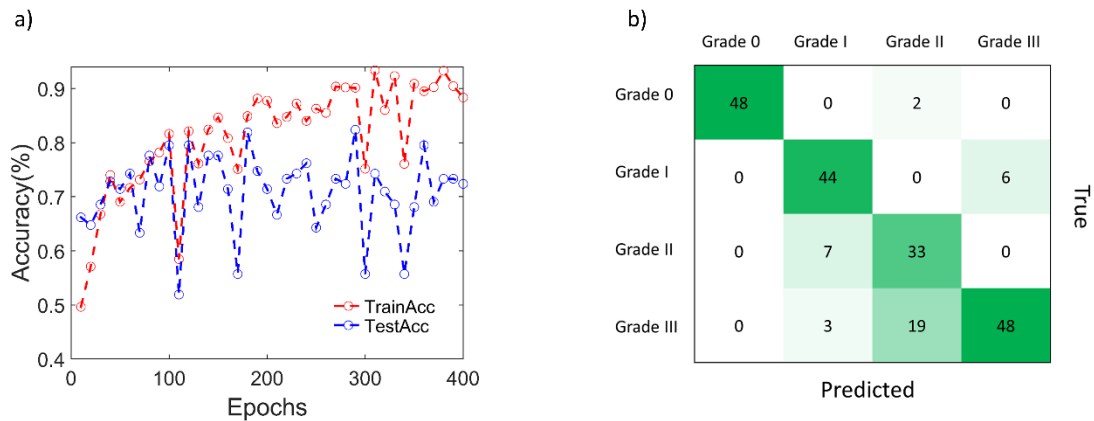


Figure 2.13 : a) Train and validation accuracy plots during PM training for one data fold of Table 2.1. In both diagrams accuracy was measured per 10 epochs. Train accuracy was defined in the same way as validation accuracy. b) Confusion matrix generated by the model after 400 epochs training and the histology predictions for the validation images. Horizontal axis refers to the grades predicted from the model and the vertical to the labeling according to pathologists. Green color brightness is proportional to the value of each cell of the matrix.

As expected, the pattern for the training and validation accuracy were similar (Figure 2.13). It is interesting to note that in most cases, local minimums displayed similar patterns in train and validation accuracy, which indicates the accuracy of the learning procedure. Focusing on this example, it seemed that training accuracy reached a plateau close to 90% after about 300 epochs while validation accuracy reached the maximum value of 82.3% at epoch 290 and decreased thereafter (Figure 2.13a). Thus, it can be argued that after 300 epochs, the proposed model does not suffer from under fitting. Overfitting, on the other hand, is mitigated by the appropriate selection of the network capacity. The PM was chosen to avoid the lower performance of CM due to over-fitting the training data.

The total number of all the tissue areas that were investigated was 210, where 90% of those were used to train the model and the rest 10% were used as validation samples. In order to evaluate the model’s diagnostic accuracy, the “predicted” versus the “true” cancer tissue categorization was examined (Figure 2.13b). In this case, 21 different tissue regions were used. For each area, 10 different sequential z images that cover the whole biopsy specimen were employed. Consequently, the sum of all indices of the confusion matrix was 210.

The images of a specific area (10 for each case) were always at the same group (validation or train). Thus, the sum of the indices for each row of the confusion matrix was always an integer multiple of ten. Indeed, the confusion matrix verified that the model could classify the collected THG images according to the grade of cancer (Figure 2.13b). The higher values of the matrix along its diagonal indicated that, in most cases, the predictions of the model coincided with the histological labeling of the tissues as evaluated by the experienced pathologists. It is interesting to note that in the case of grade 0 cancer, the model labeled in a correct manner 96% of the images and did not confuse any validation image from malignant tissue, as benign. On the other hand, grades II and III showed lower accuracy, which could be due to the partially imbalanced processed data sets. Benign (grade 0) and malignant (grade I, II, III) tissues included 32 areas and 178 areas respectively. Although one could restrict the

study in the distinction of benign and malignant breast tissues, the proposed model provided powerful information as to the grade of the tumor as well. Therefore, the use of a 4 grade classification was successfully chosen instead of a binary, between benign and malignant samples. In addition, the total confusion matrix was calculated in order to verify that the same holds in general for the PM model.

	Grade 0	Grade I	Grade II	Grade III	
Grade 0	295	0	25	0	True
Grade I	10	508	53	29	
Grade II	38	87	553	42	
Grade III	9	59	80	312	
	Predicted				

*Figure 2.14 : Overall confusion matrix generated by the PM after 400 epochs training and the histology predictions for all the 10 folds of Table 2.1. Horizontal axis refers to the grades predicted from the model and the vertical to the labeling according to pathologists. Green color brightness is proportional to the value of each cell of the matrix.*

The outcome of Figure 2.14 confirmed the conclusion derived during the analysis of the one representative data set case. From grade 0 to grade III, the precision is equal to 0.84, 0.78, 0.78, and 0.81 respectively. The recall is equal to 0.92, 0.85, 0.77 and 0.68, whereas the F1-score is equal to 0.88, 0.81, 0.77 and 0.74, for each class respectively.

As mentioned in the data pre-processing analysis, although an obtained THG image could resemble to those recorded from same area at different depths, it could contain detectable information that the model could be able to distinguish.

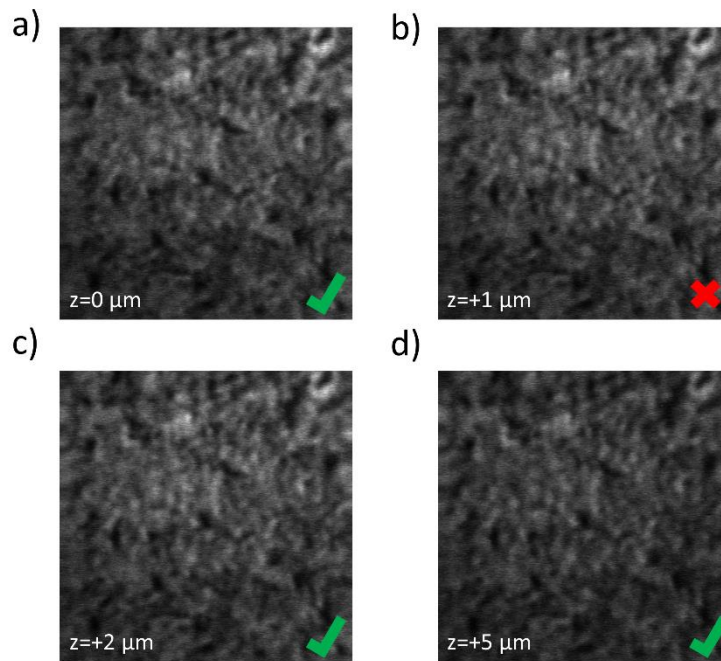


*Figure 2.15 : Characteristic example of a grade III cancer female breast tissue area as imaged using THG microscopy. Image brightness is proportional to the recorded THG signal of each pixel. At the bottom left corner of figures a-d, the depth of the irradiated tissue relative to the first one is indicated. The model correctly predicted the grade of the tissue in three images (green check mark at the bottom right corner) and failed in one case (red X).*

An example is shown in Figure 2.15. No apparent differences can be detected in images obtained at various depths (Figure 2.15a-c). Although the model failed to correctly predict the tissue type from depth  $z=+1\mu\text{m}$  (Figure 2.15b), it is interesting to note that the model correctly evaluated as grade III the image with  $z=+5\mu\text{m}$  regardless its lower brightness as compared to the others, which verified that each adjacent image recorded in  $z$  direction contains valuable information that differentiates it from each other. Consequently, these images were suitable for the training and the evaluation of the model.

The proposed model could successfully distinguish THG images recorded from the different cancer grades (Figure 2.16a-d). However, since these images display significant differences and detectable structural features, conventional machine learning techniques for automating the categorization could have been alternatively applied. Yet, even in this case the features of images should be appropriately chosen to ensure the robustness of the resulting model under the different conditions tested. It is interesting to note that the grade III THG images presented in Figure 2.15 do not resemble the THG image of the same grade depicted in Figure 2.16d. However, by using the developed CNN technique, there was no need for feature extraction, as this was part of the training procedure. The results obtained following the PM (Table 2.1) and the achieved precise discrimination of the different grades (confusion matrix Figure 2.14) indicated the high accuracy of the developed CNN model. Moreover, the model's robustness could be verified through its capability to correctly classify tilted delineated areas and images collected from deeper tissue layers.

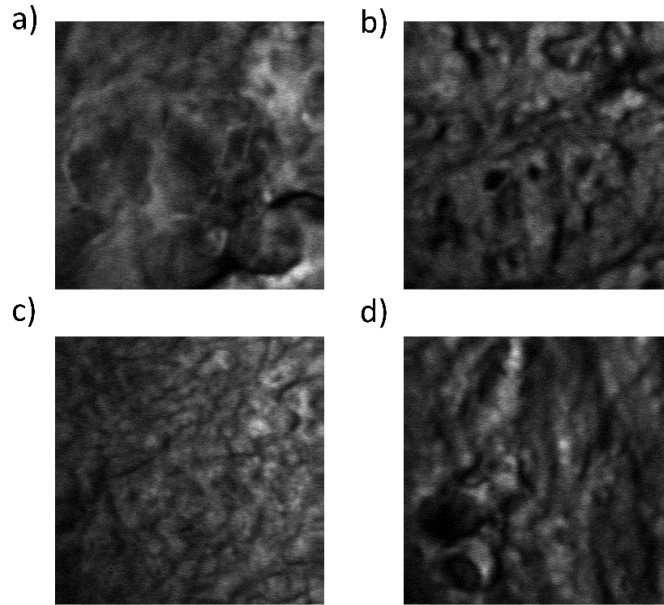


Figure 2.16 : THG images from grade 0-III samples respectively (a to d). These non-linear images were characterized correctly from our model.

In this work, we focused mainly on intra-tumoral heterogeneity and ignored that samples obtained from the same patient might be correlated. We thus explored the performance of our classifier at image-based level. In other words, samples originating from the same patient appear in both the training and validation set. In that way, the overall performance presented was probably overestimated. A patient-based analysis has been also performed (Figure 2.17). However, the limited number of samples dooms the algorithm to under fitting, especially for grade 0, for which, data from only two human subjects are available.

	Grade 0	Grade I	Grade II	Grade III	
Grade 0	53	66	190	11	True
Grade I	39	253	137	71	
Grade II	177	70	437	36	
Grade III	18	35	149	258	
	Predicted				

Figure 2.17 : Characteristic confusion matrix generated on patient-based analysis of the training and validation sets. For comparison with Figure 4 (multi-regional classification) also 10 folds cross validation were employed. Due to the procedure, the data from a grade I patient (100 images from 10 different regions) were not used in the validation set. Thus the total sum of the elements presented in the table is 2000. Horizontal axis refers to the grades predicted from the model and the vertical to the labeling according to pathologists. Green color brightness is proportional to the value of each cell of the matrix. Due to the limited number of samples ( $n=15$ ) the classifier at patient level rendered poor results for tissue discrimination, especially for grade 0 case.

### 2.3.5 Discussion

Early detection of primary or recurrent breast cancer is of considerable clinical importance for effective treatment. The use of molecular biomarkers for classification and assessment of tumor development has been documented, and nowadays such tools are being employed in diagnosis, monitoring response to therapy, early detection of metastasis and recurrence of the disease[58]. However, due to tumor cell polymorphism and the low diagnostic sensitivity and specificity, the usefulness of tumor markers is being re-examined. Physiological cells, by inducing aberrant protein expression succeed to alter their activation state, alter their morphology and behavior and become tumorigenic. The development of technologies that identify tumor cells as to their activation state and morphology could be very useful in the universal detection of tumor cells. To this extend, the use of novel, non-invasive, label-free optical methods and the automation in the analysis procedure by employing advanced computational methods for tissue/cell evaluation are required. Automated detection of clinically meaningful malignant regions of interest is an essential step to diagnosis. In this chapter, the application of a machine learning technique that is able to predict automatically malignant regions in thin biopsy samples, based on the recorded THG signals was depicted. The proposed approach successfully discriminated benign from cancerous samples and categorized the different grades of breast cancer tissue with high accuracy.

The effectiveness of the THG imaging technology in discriminating benign from malignant breast tissue and defining disease severity has been previously demonstrated [71]. Taking the next step, it was mandatory to replace the manual analysis of tissue regions with an automated system that would be applied in clinic, without the need of highly trained personnel. In this respect, an evaluation scheme that could monitor changes in the whole area of the recorded non-linear images is expected to obtain significantly improved results in the classification of the different types of tissues. Towards this direction, the current work showed that the utilization of deep learning methods analysis enabled the discrimination of the different grades of thin breast biopsy samples. The minimum time needed to acquire and analyze the THG images together with the high rates of success, make the proposed method very attractive for real-time applications.

A significant improvement of the current study is that breast tissue characterization was based on the application of a CNN model to images that were recorded from unstained samples, in contrast to other works, where deep learning techniques were applied to images derived from stained specimens (histopathology images) [91]–[93]. This comprises an advancement for the implementation of this methodology to clinic for the fast characterization of newly excised unstained biopsy specimens without further fixation or staining. In addition, several works have shown the feasibility to detect increased back scattered THG signals from thick unstained tissues [97], thus demonstrating the potential usefulness of the developed CNN classifier for precise characterization of a variety of thicker tissue samples.

The proposed technology could therefore be applied to the clinical environment, supplementing the existing, well established, diagnostic histopathology procedures for faster results. Furthermore, the continuous progress in the miniaturization technology and the availability of new, state of the art fs laser sources can assist in the design of innovative compact non-linear optical apparatuses with great flexibility to be incorporated into standard typical clinical endoscopes[98]. The present work anticipates that the development of these

particularly promising set-ups in conjunction with the above described efficient, reliable, and fast, CNN image classifier will open new insights in diagnosis and provide evolutionary microscopy platforms to be used in clinical practice.

## Chapter 3 - Novel PSHG studies

### 3.1 PSHG for collagen-based differentiation of breast cancer samples

#### 3.1.1 Introduction

Collagen, which has been considered as cancer biomarker [99]–[101], is an ideal emitter of high SHG signals due to its non-centrosymmetric structure [102]. Indeed collagen has been considered as a double-edged sword in tumor progression, playing a determinant role, initially in protecting against and later in facilitating tumor cell migration and cancer progression [103]. Collagen is a major structural protein of the extracellular matrix (ECM) consisting of one or multiple fibrils, each one made of three polypeptide  $\alpha$ -chains, held together with hydrogen bonds to form a collagen helix [104].

During tumor progression, the ECM undergoes remodeling, characterized by collagen re-deposition and cross-linking, which under the biomechanical tension of tumor growth becomes accessible to enzymatic digestion, facilitating thus tumor expansion [105]. Briefly, collagen, being the most abundant and most difficult to penetrate component of ECM, when remodeled in response to tumor expansion, increases in density and consequently its mechanical strength protects from further tumor expansion [106][107]. Thickened collagen fibers inhibit enzymatic access and cleavage. However, extensive tumor expansion exerts traction forces on collagen causing its deformation until reaching a critical point, leading finally to triple helix separation, and thus collagen becomes susceptible to enzymatic cleavage [105]. These features are more prominent in higher grades of breast cancer. Unwinding and remodeling of collagen leads to the formation of novel focal points for tumor cell migration and proliferation, infiltration of immune cells with tumor inhibitory or stimulatory effects, which, however, in most cases, promote tumor metastasis [105][108]. Therefore, following collagen behavior could provide very important information in the evaluation of cancer progression.

Breast cancer, which is considered as a typical example of collagen fiber remodeling [109], as mentioned in the previous chapter is one of the most common malignancies in women [58]. For that reason, the efficient treatment of patients, which is based on early and accurate diagnosis, is extremely important. Unfortunately, until now, no ideal markers that could detect all breast cancer cases have been established [58]. Therefore, the development of novel, non-invasive, label-free optical techniques based on collagen alternations could act synergistically with the existing THG results presented in the previous chapter providing thus new insights for early stage breast cancer diagnosis.

In the framework of this thesis, the non-linear imaging modality of PSHG was employed as a tool for breast cancer research. Specifically, quantitative information about structure and directionality of SHG emitters, as represented by collagen, within thin breast tissue sections was obtained upon acquisition of PSHG measurements, which could provide information on the differentiation of benign from cancerous breast tissues. The biophysical model proposed herein could be used for the development of an accurate objective diagnostic tool for breast cancer, based on the PSHG information arising from collagen remodeling.

### 3.1.2 Materials and Methods

#### PSHG setup

In this study, SHG signals produced by the femtosecond fiber based laser and the energy per pulse at the sample plane was 1 nJ. The 0.8 NA objective lens was used and the scanning was performed with a pair of silver coated galvanometric mirrors. SHG signals were collected in forward direction using a bandpass interference filter (Thorlabs 532-10) and a short pass filter (Semrock 720) before the PMT's input to cut off the transmitted laser light and solely detected SHG signals from the samples. Typical time duration for obtaining a 2-D 500x500 pixels (125x125  $\mu\text{m}^2$ ) SHG image was one second. To improve the signal to noise ratio (SNR), 3 scans were realized for each image. For compensating the polarization ellipticity, when a dichroic mirror is being employed, a quarter wave plate is advisable to be introduced in the optical path [110]. However in our case, silver coating mirrors were used to minimize the induced polarization ellipticity at the sample plane. The extinction ratio, using cross polarization measurements at the sample plane, was measured to be higher than 25:1 for all linear polarization orientations, which is in agreement with a study that employed a similar set-up [111].

#### Biological samples

The same samples described in the previous chapter were used since a recent study has reported the feasibility to record high SHG signals from paraffin-embedded tissue sections [112]. Moreover, the selection of the scanning regions was accomplished by looking in parallel through a light microscope, the corresponding H&E stained images that had been classified by experienced pathologists. Multiple regions of each tissue, at least 10, were scanned.

#### PSHG data analysis

Previous studies have shown that the collagen can be considered as a cylindrically symmetrical sample [113][114][48][115], and therefore the overall produced SHG signal from it can be described by the Equation 1.15. In addition, in order to reduce the computational time, Equation 1.15 can be transformed to the following mathematical form [115]:

$$I_{SHG} = c_0 + c_1 \cdot \cos(2 \cdot (a - f)) + c_2 \cdot \cos(4 \cdot (a - f)) \quad 3.1$$

Where,

$$B = \frac{c_0 + c_1 + c_2}{\sqrt{c_0 - c_1 + c_2}} \quad 3.2$$

The advantage of the above approach is that it makes feasible to calculate  $c_0$ ,  $c_1$ ,  $c_2$  coefficients (therefore  $B$ ) and the  $f$  angle by applying Discrete Fourier Transform (DFT) data processing for several different polarization angles  $a$  [115][116]. The computational time of DFT for 500x500 pixels images is  $10^4$  orders of magnitude faster as compared with the utilization of a non-linear fitting algorithm for the Equation 1.15.

Moreover, as mentioned in the PSHG Theory section of Chapter 1, if the laser propagates perpendicular to the collagen symmetry axis (angle  $\delta=90^\circ$ , Figure 3.1a) then via Equation 1.18 and the value of the anisotropy parameter  $B$  can be calculated the effective angle  $\theta_e$  of SHG emitters and sample's symmetry axis (Figure 3.1b).

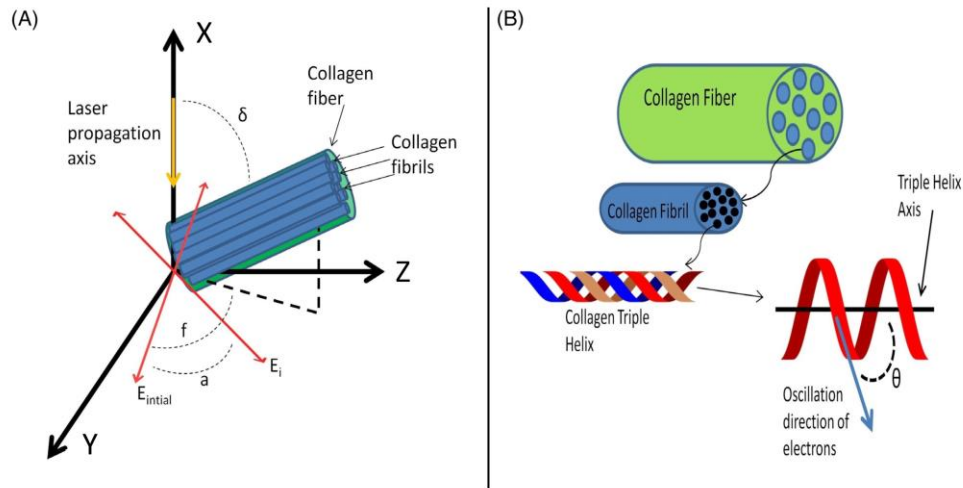


Figure 3.1 : (a) Collagen fiber (green cylinder) is consisting of fibrils (blue cylinders) which are radiated by laser. The yellow arrow represents the direction of laser propagation at the laboratory's coordinates system (XYZ) and  $\delta$  is the angle between the fiber axis and the laser's propagation direction. Red arrows represent the laser polarizations, which are onto the YZ plane.  $E_{initial}$  is the initial electric field and  $E_i$  the electric field after an  $\alpha$  angle of rotation. Angle  $f$  is the angle between the initial polarization and the projection of the fiber axis onto the YZ plane. (b) Hierarchical structure of collagen fiber (green cylinder) is consisting of fibrils (blue cylinder) which are made of triple helices (black dots).  $\theta$  represents the angle between the tangent line at any point of the collagen triple helix and the helix axis, which is a good approximation of the radiated electrons' oscillation direction  $\theta_e$  [49][117].

The analysis for obtaining the anisotropy parameter  $B$  values for each pixel of a SHG image is described below. A 3D matrix (PSHG matrix) was produced from eighteen SHG images of the same area, rotating each time the laser's linear polarization by ten degrees ( $\alpha=0^\circ-170^\circ$ ). The first two dimensions of the PSHG matrix refer the location of the pixels from a SHG image, while the third dimension to the value of each pixel for all laser polarizations.

A specially constructed algorithm, that was designed and programmed in MATLAB environment, computed first the coefficients  $c_0$ ,  $c_2$  and angle  $f$  of the left cosine term of Equation 3.1 by applying DFT along the third dimension of the PSHG matrix. Afterward, the algorithm computed the last one coefficient  $c_4$  by assuming as a constant the already known value for angle  $f$  of the right cosine term. By integrating the total amount of image pixels, the mean anisotropy parameter ( $\langle B \rangle$ ) can be extracted. Erroneous pixels, like noise pixels, which are not in line with the model, must be excluded. In this study, as a filtering criterion, a threshold value was used as referred in literature [118] for the determination the coefficient  $R^2$ , and pixels below this value were excluded from further processing. Specifically, the threshold value of 0.90 was set, in order to verify that the results fit into the model and at the same time, to ensure a high enough number of pixels for the statistical analysis.

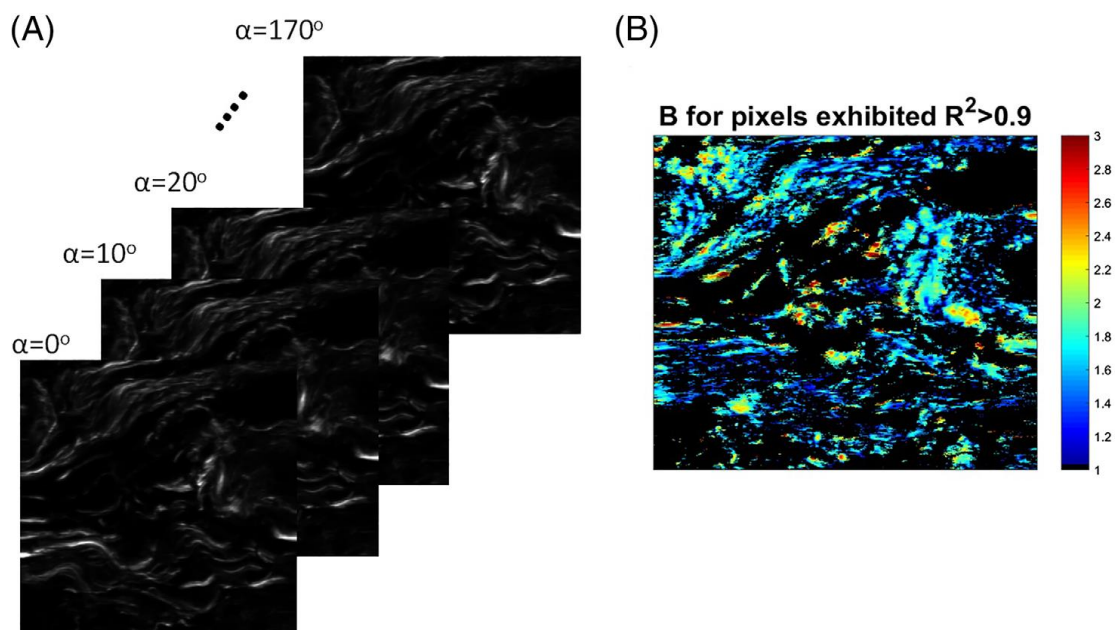


Figure 3.2 : Example of DFT analysis of PSHG data from a benign breast tissue sample. a) Full set of PSHG data consist of 18 SHG images from the same area of the tissue. Each time angle  $\alpha$  of Equation 3.1 is rotating by  $10^\circ$ . b) Results of DFT analysis of PSHG data set (a). Each pixel of figure b corresponds to a  $B$  value, which was calculated through the determination of  $c$  coefficients via DFT analysis and Equation 3.2. Pixels with  $R^2 < 0.9$  were excluded from further analysis and were presented as black spots.

Figure 3.2 presents a characteristic example of PSHG data analysis of a benign tissue specimen. The mean value of  $B$  ( $\langle B \rangle$ ) deriving from pixels with  $R^2 > 0.9$  is  $1.742 \pm 0.001$  (S.E.M.). Moreover, in the framework of the current study a new factor called "ratio parameter" was introduced for providing additional valuable, quantitative information through PSHG analysis of the collected data. The value of this parameter was defined as the number of collagen pixels with  $R^2 > 0.9$  divided by the total number of collagen pixels. As countable collagen pixels were considered only these that presented minimum value along the third dimension of the PSHG matrix over the system noise. For the tissue analyzed in Figure 3.2, this ratio parameter was equal to 0.388. The above data analysis was performed through a constructed algorithm that was designed and programmed in a MATLAB environment for analyzing PSHG data sets and extracting for each area the mean  $B$  as well as the ratio parameter values.

### Statistical analysis

For multi group comparisons, two-tailed unpaired Student's T-test was applied. P-values  $< 0.05$  were considered significant (\*), values  $< 0.01$  were considered very significant (\*\*), and values  $< 0.001$  and  $< 0.0001$  were considered highly significant (\*\*\*) and \*\*\*\*). Statistics were performed using GraphPad Prism 6.01 (Graphpad Software, La Jolla, CA).

### 3.1.3 Results

In an effort to investigate the potential collagen's directionality and organization modifications during the progression of breast cancer without the need of staining, it was

attempted to visualize and obtain qualitative information from collagen structures in thin sections of breast tissue by collecting SHG signals.

Serial sections of breast tissue biopsies were submitted to H&E staining as well as SHG imaging (Figure 3.3). Such manipulation allowed examination of H&E images staining of benign and malignant breast tissues and the corresponding non-linear unstained microscopy images (SHG), so that monitoring reflects the same area of the sample. SHG measurements correspond to collagen organization and distribution within the tissue (Figure 3.3a). As described in the histology-based literature collagen surrounding normal epithelial structures are curly and smooth, while in tumors collagen develops in parallel with the oncogenic tissue, progressively thickens, linearizes and stiffens [109]. Such description completed fitted the SHG-derived images, where thicker and linearized collagen could be visualized around the carcinoma, without the need of use of any histological staining (Figure 3.3a).

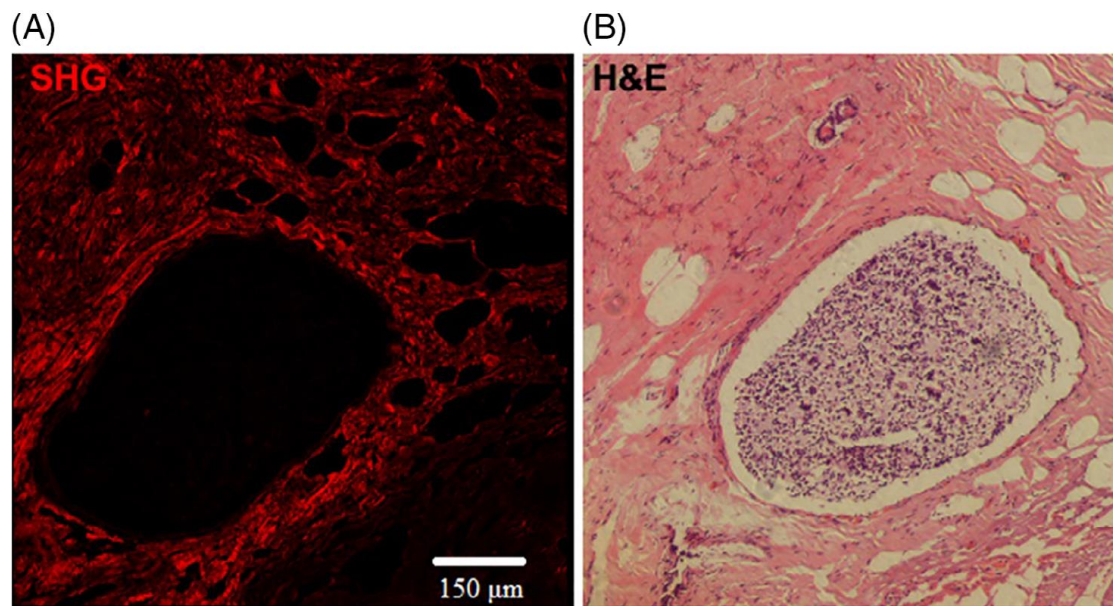


*Figure 3.3 : a) SHG image of ductal carcinoma grade I. The image is 1mm x 1mm in size and consists of 100 sequential sub-images (100μm x 100μm). b) The corresponding H&E stained tissue obtained with a brightfield microscope. The obtained data were recorded from different sequential tissue sections.*

To further characterize the cancerous areas within breast tissue biopsies, PSHG data analysis, as described in materials and methods section, was applied to different cases of breast tumor severity ranging from benign grade 0 to grades I, II and III. In all cases, the scanning regions studied were limited to 125 μm x 125 μm dimensions. Upon acquisition of PSHG images of all tissue types tested, PSHG analysis as to the characteristic anisotropy and ratio parameter values was performed (Figure 3.4).

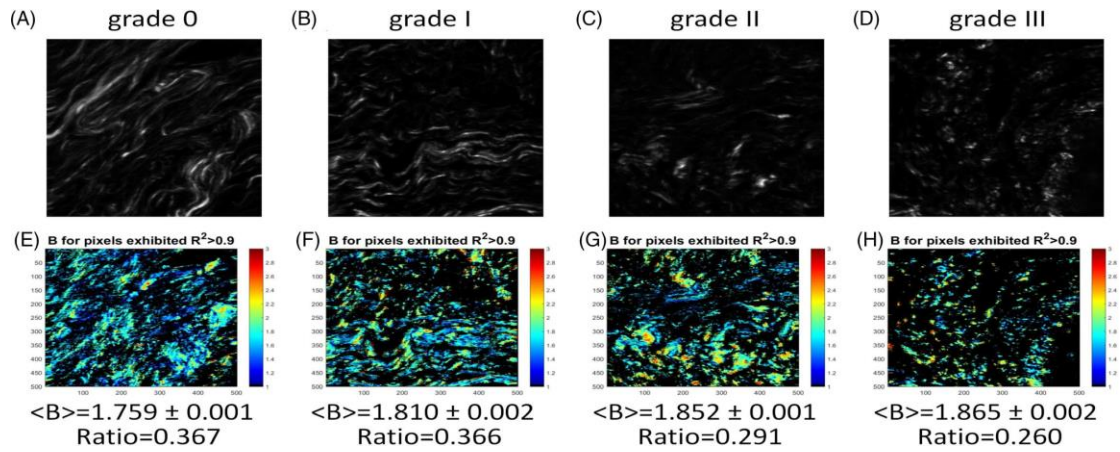


Figure 3.4 : Representative examples of DFT analysis for benign (grade 0), grade I, grade II and grade III breast tissues. (a-d): The sum of 18 different polarization SHG images for each grade. (e-h): Results of the DFT analysis for each sample a-d.

The application of PSHG to grade 0 tumor samples (Figure 3.4a) nicely showed the thickening linearization of collagen, which also showed the lowest anisotropy factor  $B$  (Figure 3.4e). Tumor severity is accompanied with collagen remodeling, likely corresponding to the collagen susceptibility to enzymatic cleavage [105], which is accompanied by increasing  $B$  values and decreasing ratio parameter (Figure 3.4 b-d and f-h).

Collecting the PSHG data sets from eight patients (two in each case) in grades 0, I, II and III, the mean values of anisotropy parameter  $\langle B \rangle$  as well as the mean ratio parameters were calculated as described in the section of materials and methods (Figure 3.5).

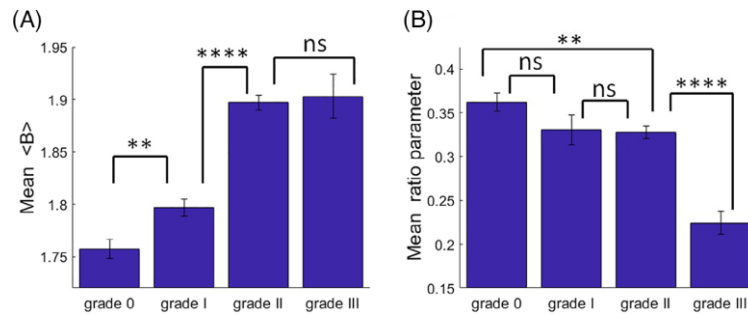
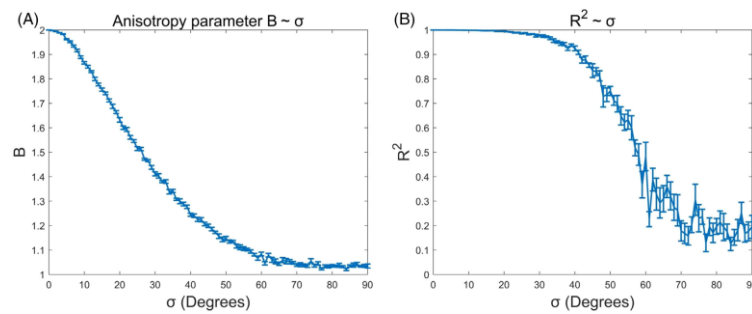


Figure 3.5 : a) Each column represents the mean value of  $\langle B \rangle$  ( $N=20$ , median values) and error bars indicate the Standard Error of the Mean (S.E.M.) of each grade. b) Each column represents the mean ratio parameter ( $N=20$ , median values) and error bars indicate the S.E.M. of each grade. ns: no significant, \*\* and \*\*\*\* statistically significant ( $<0.01$  and  $<0.0001$  respectively).

Thus, the mean anisotropy parameter ( $\langle B \rangle$ ) showed a significant increase until grade II tumor progression. Grades II and III did not show any statistically significant difference in  $\langle B \rangle$  values. Apparently, in the grade II and III samples analyzed herein, collagen could have been disrupted by enzymatic cleavage, showing at the same time an increased anisotropy  $\langle B \rangle$  value, which, however, could not distinguish among the two different grades (Figure 3.5a). In contrast, the mean ratio parameter values showed a highly significant decrease between grade II and III stages (Figure 3.5b).

Thus, if  $\langle B \rangle$  values were affected by collagen disruption and fibril orientation [119], this could mean that not all fibrils were completely parallel to fiber axis, which resulted in an

anisotropy reduction of the fiber. For fully isotropic arrangement of fibrils the expected value of the fiber anisotropy parameter is close to the unit, while increasing along with the alignment of the fibrils across the fiber axis [120][121]. For verifying this hypothesis, the effects of angles  $f$  and  $\delta$  orientation disorders on the calculated from the PSHG analysis anisotropy parameter  $B$  values were simulated. This procedure takes into account the contribution of each collagen fibril intensity value within the focal volume for the calculation of the total SHG intensity [121][122]. Considering that the  $f$  and  $\delta$  angles have constant mean values and follow normal distributions around themselves, with the same standard deviation  $\sigma$ , meaning that standard deviation  $\sigma$  represents the orientation disorders of  $f$  and  $\delta$  angles,  $B$  values tend to the unit as  $\sigma$  increases (Figure 3.6a, simulation from Equation 1.15, 3.1 and 3.2).



*Figure 3.6 : Theoretical effects of angles  $f$  and  $\delta$  disorders ( $\sigma$ ) to anisotropy parameter  $B$  (a) and  $R^2$  (b) values. In both cases it is assumed that the focal volume is  $\sim 3 \mu\text{m}^3$  and includes 100 fibrils with mean diameter and length in the order of 200 nm and 1  $\mu\text{m}$  respectively [123][124]. This is considered to be a good approximation for the focusing conditions that were employed ( $N.A.=0.8$ ). Each fibril follows Equation 1.15 with  $B_{th}=2$  and angles  $f$  and  $\delta$  following a normal distribution with the same standard deviation  $\sigma$  and mean values  $0^\circ$  for  $f$  and  $90^\circ$  for  $\delta$ . For each  $\sigma$ , 10 different PSHG data sets are generated, and PSHG analysis was applied each time for the calculation of anisotropy parameter  $B$  and  $R^2$  values. Error bars corresponds to S.E.M.*

As an example, considering that  $\theta=45^\circ$  in Equation 1.18, which corresponds to the expected collagen helix angle as evaluated by X-ray diffraction experiments [49], a theoretical value of  $B$  in the order of 2 ( $B_{th}=2$ ) is obtained (Figure 3.6a). The calculated  $B$  values tend to the unit when  $\sigma$  increases, and this trend is independent of  $B_{th}$  [121]. At the same time for  $\sigma < 20^\circ$ ,  $R^2$  remains close to the unit (Figure 3.6b). Therefore, up to that point, PSHG data seem to fit perfectly to the biophysical model. Such analysis implies that the reduction of the ratio parameter values at higher grades of tumour progression, observed in Figure 3.5b, could not be attributed to the  $f$ ,  $\delta$  angle orientation disorders, indicating that different morphological modifications of the collagen structure occur after the grade II scoring. These theoretical results were in perfect agreement with the biological events, where after tumour expansion reaches a critical point, collagen is deformed by triple helix separation, becoming susceptible to enzymatic cleavage, forming thus novel focal points for tumour cell development and disease aggravation.

#### 3.1.4 Discussion

In an effort to quantitatively correlate PSHG imaging to differentiate benign from breast cancer samples, tissue biopsies from cancer grades 0, I, II and III were submitted to PSHG imaging and data were then processed using Discrete Fourier Transform analysis, while also calculating SHG anisotropy and the "ratio parameter" values. The obtained results indicated

that PSHG data analysis could correlate the increment of the anisotropy parameter  $B$  (Figure 3.5a) with tumour progression [125]. Such behavior could indeed be due to the mechanical tensions applied to collagen during cancer progression.

The orientation disorders of fibrils result in the reduction of the anisotropy parameter of the fiber as predicted by the theoretical calculations in Figure 3.6a. In the case of collagen, it is assumed that the mechanical stretch further aligns the fibrils with the fiber axis, reducing thus the standard deviation  $\sigma$  of angles  $f$  and  $\delta$  (Figure 3.7 a and b) and finally increasing anisotropy parameter  $B$  values. This is in accordance with the measured values of  $B$  presented in Figure 3.5a. Furthermore, mechanical stretching may decrease collagen helix angle as shown in Figure 3.7 c and d. This reduction of collagen helix angle, according to Equation 1.18 in the section of materials and methods, leads to an increase of  $\chi_{33}/\chi_{31}$  ratio and consequently to a raise of anisotropy parameter  $B$  values, as foreseen from Equation 1.16 of the same section.

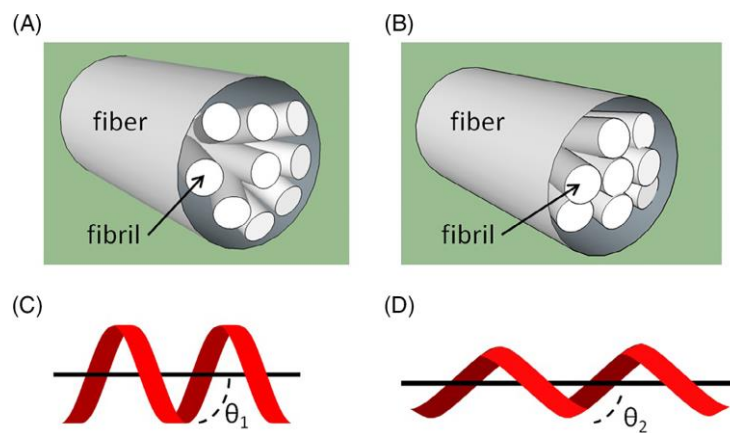


Figure 3.7: Schematic view of collagen's fiber, fibril and helix before (a,c) and after (b,d) mechanical tension. In the case of mechanical tension collagen fibrils are almost parallel to the fiber and the angle of the helix decreases ( $\theta_2 < \theta_1$ ). The scales of the figure in the cartoon are arbitrary.

During cancer progression, collagen structure is deformed and enzymatic cleavage results in a crumbled image [105][108] as the one presented in Figure 3.4d. The observed discontinuities in collagen detected by the SHG signal in Figure 3.4d (grade III sample) could be due to the triple helix separation, while other collagen areas could be only affected by structural organization modifications. Such changes could be expressed through the quantitative calculation of the ratio parameter values presented in Figure 3.5b. The reduction of ratio parameter value at grade III could be nicely explained by the breakdown of the collagen's cylindrical symmetric structure. As a consequence, SHG cannot be described by Equation 1.15, indicating the use of different biophysical model at that point. A recent work demonstrated that a more generalized model, considering both cylindrical and trigonal symmetry, could be used to describe the organization of collagen structure [126]. Such approach could provide improved results in human breast samples [127].

Following the experimental approach described in this thesis, which was based on the calculation of the integrated anisotropy parameter values of different collagen types, the discrimination between benign and malignant cancer tissue samples could be achieved. A study related to the differentiation of biochemically different collagen types, showed that the average anisotropy parameter values in collagen I and II, from tendon and cartilage

respectively, were similar [121]. Therefore, the findings of the aforementioned study [121] indicate that the biochemical nature of collagen does not influence the anisotropy parameter values, which could be considered to be governed by the biomechanical properties of collagen fibers.

It has to be noted that in the experimental design of the current work, a forward detection scheme was employed for the collection of the SHG images from thin paraffin-embedded sections. Although SHG anisotropy parameter values depend on the detection geometry [128], the extracted information could be useful as a novel diagnostic tool for a quick characterization of newly excised thin biopsy samples. A recent study using PSHG reflection measurements at colon mucosa samples shows that cancer may increase collagen fibrils organization even 20 cm away from cancerous area [129].

This study has a significant clinical potential, since it can monitor quantitative changes in the sub-cellular behavior of collagen in different types of breast human tissues. This approach enables to quantitatively differentiate benign from cancerous breast biopsy samples thus PSHG could be a unique tool helping to improve cancer detection rates. Moreover, it is worth underlining that the applied technology has the ability to also act synergistically with other non-linear processes, such as third-harmonic generation and polarization-dependant THG (PTHG) into a single, unified microscopy platform, providing thus complementary structural information from the different types of tissues. Using a single beam, without the need of staining, except from probing collagen modifications via PSHG analysis, information on lipid bodies concentration, inhomogeneities, membranes [68][130][78], as well as ordered lipid assemblies [131] through the performance of THG and PTHG measurements respectively, could be obtained. Thus the unique attributes of non-linear microscopy provide promising imaging modalities as potential new, non-invasive tools for disease diagnostics in clinic. Non-linear endoscopes have been already employed for the imaging of thick animal tissues [132][133] and it is anticipated that the integration of polarization-dependant techniques could provide additional unique molecular information.

## 3.2 PSHG for myosin structural alterations of *C. elegans* body-muscles during aging

### 3.2.1 Introduction

Aging is directly related to the gradual loss of muscle mass and strength of the human musculoskeletal system. The effect of aging on muscles is called sarcopenia. Sarcopenia syndrome is age-related [134] and occurs in healthy adults over the age of 50, but is a high risk for physical disability due to gradual muscle loss affecting thus the quality of their life [135]. On a microscopic scale, the pathological causes of sarcopenia are due to changes in both the composition and function of the molecules and proteins that are structural elements of the sarcomere. Biochemical studies have revealed that the myosin molecule undergoes molecular changes over time, thus contributing to the development of the syndrome [135].

In the framework of this thesis PSHG microscopy was employed to extract quantitative information for the changes that occur in the structure of the myosin molecules of *Caenorhabditis elegans* (*C. elegans*) samples during aging. Striated muscles of the worm were investigated. Striated muscles are formed from multiple sarcomeres and are similar to human skeletal muscles [136]. Myosin molecules are some of the main building blocks of the sarcomeres whereas each molecule consists of two heavy chains, which fold and form a double helix [137]. Myosin is an ideal emitter of high SHG signals due to its non-centrosymmetric structure [138][48].

Studies have been used PSHG measurements for the functional imaging of muscle cells and the in vivo monitoring of conformational changes in myosin [139][140]. Moreover, structural alterations of cardiac myosin filaments has been detected and it was possible the discrimination of a- and b-myosin in cardiac samples via PSHG [141][142]. During this thesis myosin structural alterations due to aging, through PSHG imaging microscopy measurements, were investigated in the striated muscles of *C. elegans* samples. A DFT (Discrete Fourier Transform) algorithm for the fast SHG signal analysis has been employed for probing myosin structural alterations. Based on the classical cylindrical mathematical symmetry model it was not feasible to extract significant changes in the calculated anisotropy parameter values, due to aging of the nematodes. Subsequently, a trigonal symmetry and a general mathematical model, which characterizes specimens with unknown structure and is not based on symmetries, were employed for the PSHG data analysis. It was demonstrated that that the worms were better described via the implementation of these two models while the discrimination of the younger from the older animals was also achieved.

### 3.2.2 Materials and Methods

#### Biological samples

The broad ranges of genetic and molecular techniques applicable in the *C. elegans* model system allow a unique line of investigation into fundamental problems in biology. The standard procedures for *C. elegans* strain maintenance, crosses and other genetic manipulations [143] was followed by K. Kounakis (Tavernarakis lab, IMBB) who had undertaken the preparation and the provision of the samples. Nematode rearing temperature was kept at 20°C. Before each experiment, adult animals were anaesthetized by immersing to an anesthetic mixture with a final volume of 20  $\mu$ L (15  $\mu$ L Tetramisole Sulphate 100 mM, 5  $\mu$ L sodium azide ( $\text{NaN}_3$ ) 20 mM) and subsequently they were mounted on thin glass slides. In the current study, wild type worms at the 1st, 6th and 9th day of adulthood were imaged.

## Experimental set up

In this study, SHG signals produced by the diode pumped laser (t-pulse) and the energy per pulse at the sample plane was 0.5 nJ. The 0.85 NA objective lens was used and the scanning was performed with a pair of silver coated galvanometric mirrors. SHG signals were collected in forward direction using a bandpass interference filter (Semrock 514-3) and a short pass filter (Semrock 720) before the PMT's input to cut off the transmitted laser light and solely detected SHG signals from the samples. Typical time duration for obtaining a 2-D 500x500 pixels (90x90  $\mu\text{m}$ ) SHG image was one second. To improve the signal to noise ratio (SNR), 10 scans were realized for each image. In this work, silver coating mirrors were used to minimize the induced polarization ellipticity at the sample plane. The extinction ratio, using cross polarization measurements at the sample plane, was measured to be higher than 25:1 for all linear polarization orientations, which is in agreement with a study that employed a similar set-up [111].

Specimens, where movement was observed during their irradiation or muscle contractions, were not included in the study. Furthermore, the samples under investigation were discarded from further analysis when minimal fluctuations of the laser power during the measurements was detected.

## Theory

For the most general case where all the  $\chi^{(2)}$  tensor elements (Equation 1.12) are non-zero and independent of each other, the form of the equation for  $I_{SHG}$  dependence with respect to the angle  $a$  is [47][144]:

$$I_{SHG} = b_0 + b_2 \cdot \cos(2 \cdot a) + b_4 \cdot \cos(4 \cdot a) + d_2 \cdot \sin(2 \cdot a) + d_4 \cdot \sin(4 \cdot a) \quad 3.3$$

which can be written as

$$I_{SHG} = b_0 + b'_2 \cdot \cos(2 \cdot (a - f_2)) + b'_4 \cdot \cos(4 \cdot (a - f_4)) \quad 3.4$$

and it is clear the difference compared it with Equation 3.1. In Equation 3.4 no symmetry axis has been assumed thus angles  $f_2, f_4$  (spectral phases) may differ. This will be pointed out analytically in this session.

If SHG emitters are arranged with trigonal symmetry, then the form of the  $\chi^{(2)}$  tensor is

$$\chi^{(2)} = \begin{pmatrix} 0 & 0 & 0 & 0 & \chi_{15} & -\chi_{22} \\ -\chi_{22} & \chi_{22} & 0 & \chi_{15} & 0 & 0 \\ \chi_{31} & \chi_{31} & \chi_{33} & 0 & 0 & 0 \end{pmatrix} \quad 3.5$$

and the generated SHG signal as a function of the previously defined angles  $a$  and  $f$ , takes the following form [75]:

$$I_{SHG} = E \cdot \{(\chi_{22} \cdot (\sin(a - f))^2 + \chi_{15} \cdot \sin[2(a - f)])^2 + [\chi_{31} \cdot (\sin(a - f))^2 + \chi_{33} \cdot (\cos(a - f))^2]^2\} \quad 3.6$$

In the case where  $\chi_{22}$  equals to zero and the sample does not absorb the incident radiation, thus Kleinman symmetry is valid and  $\chi_{15}$  equals to  $\chi_{31}$ , then Equation 3.6 takes the form of Equation 1.15. That means that the cylindrical symmetry is a specific case of trigonal symmetry and the ratio of the absolute value of  $\chi_{22}$  divided by  $\chi_{31}$  comprises a measure of

the balance between these two symmetries. This ratio, denoting as S (symmetry parameter), and its increase correspond to the dominance of the trigonal symmetry against the cylindrical one [126][127].

Via simple trigonometric identities, Equation 3.6 can also be written in the general form of 3.3 as:

$$I_{SHG} = b_0 + b_2 \cdot \cos(2 \cdot (a - f)) + b_4 \cdot \cos(4 \cdot (a - f)) + d_2 \cdot \sin(2 \cdot (a - f)) + d_4 \cdot \sin(4 \cdot (a - f)) \quad 3.7$$

where:

$$b_0 = E \left[ \frac{3 \cdot (x_{22}^2 + x_{31}^2 + x_{33}^2)}{8} + \frac{x_{15}^2}{2} + \frac{x_{31} \cdot x_{33}}{4} \right] \quad 3.8$$

$$b_2 = E \left[ \frac{x_{33}^2 - x_{31}^2 - x_{22}^2}{2} \right] \quad 3.9$$

$$d_2 = E[x_{22} \cdot x_{15}] \quad 3.10$$

$$b_4 = E \left[ \frac{x_{22}^2 + x_{31}^2 + x_{33}^2 - 4 \cdot x_{15}^2 - 2 \cdot x_{31} \cdot x_{33}}{8} \right] \quad 3.11$$

$$d_4 = E \left[ \frac{-x_{22} \cdot x_{15}}{2} \right] \quad 3.12$$

Finally, Equation 3.7 can be re-expressed based on the form of Equation 3.4 as:

$$I_{SHG} = b_0 + b_2' \cdot \cos(2 \cdot (a - [f - \Delta f_2])) + b_4' \cdot \cos(4 \cdot (a - [f - \Delta f_4])) \quad 3.13$$

where :

$$\Delta f_2 = \frac{\operatorname{atan} \left[ \frac{2 \cdot S \cdot \frac{x_{15}}{x_{31}}}{S^2 - \left( \frac{x_{33}}{x_{31}} \right)^2 + 1} \right]}{2} \quad 3.14$$

and

$$\Delta f_4 = \frac{\operatorname{atan} \left[ \frac{4 \cdot S \cdot \frac{x_{15}}{x_{31}}}{4 \left( \frac{x_{15}}{x_{31}} \right)^2 + 2 \cdot \frac{x_{33}}{x_{31}} - S^2 - \left( \frac{x_{33}}{x_{31}} \right)^2 - 1} \right]}{4} \quad 3.15$$

For the trigonal symmetry case it is clear now the physical meaning behind the difference in spectral phases (angles  $f_2$  and  $f_4$ ) from Equation 3.4. These angles, which can be computed through the DFT of SHG signal, are equal with the angle  $f$  minus  $\Delta f_2$  and  $\Delta f_4$  respectively. Equations 3.14 and 3.15 show that these  $\Delta f$  values depend on S. The next graph presents that, the enrichment of S increases also the difference between  $f_2$  and  $f_4$ . Thus a potential detected increased difference value between these two angles is an indicator of the domination of trigonal versus cylindrical symmetry.

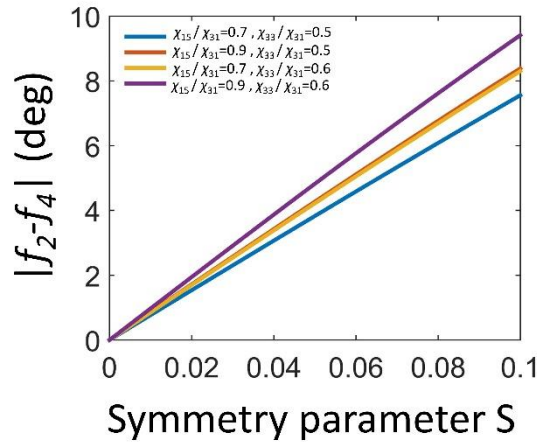


Figure 3.8 : Plot diagram of the absolute difference between  $f_2$  and  $f_4$  based on Equation 3.14 and 3.15 for different typical values of  $\chi_{15}/\chi_{31}$  and  $\chi_{33}/\chi_{31}$  as symmetry parameter S increases.

#### PSHG data analysis

As in the previous section, for each sample 18 2D SHG images of the same area were recorded, rotating each time the laser's linear polarization by 10 degrees ( $\alpha=0^\circ-170^\circ$ ), creating thus a 3D matrix (PSHG matrix) with dimensions  $500 \times 500 \times 18$ . However, due to the in vivo nature of our experiments small movements of the samples were possible during PSHG measurements. To verify the validity of our analysis, the 18 recorded SHG images firstly aligned through Fiji software for ensuring that the modulation of the non-linear signal from a pixel area comes from the rotation of the incident polarization. Images from samples that were not sufficiently aligned with the software were discarded.

In addition the developed DFT algorithm of the previous section (3.1) was evolved in order to compute the coefficients  $b_4$  and  $d_4$  of the general model (Equation 3.3) and through them the coefficient  $b'_4$  and angle  $f_4$  of Equation 3.4 by applying again DFT along the third dimension of the PSHG matrix. There is no need to be estimated the values of the coefficients  $b_0$ ,  $b'_2$  and angle  $f_2$  of Equation 3.4 since the way they were calculated by DFT is identical to that of  $c_0$ ,  $c_2$  and angle  $f$  of Equation 3.1. However, the recalculation of  $R^2$  values is necessary.

As it is already discussed Equation 3.6 describes samples where the trigonal symmetry is dominating. Equation 3.6 can be written in the form of Equation 3.13 where the coefficients  $b_0$ ,  $b'_2$ ,  $b'_4$ ,  $f_2$ ,  $f_4$  can be calculated via DFT analysis. However, for specimens with unknown structure, the DFT analysis cannot provide confidential information about Equation 3.6 parameters ( $E, f, \chi_{22}, \chi_{15}, \chi_{31}, \chi_{33}$ ). As mentioned in the previous section, the Fourier form of Equation 3.3 can describe the SHG signal modulation with respect to the angle that the laser polarization was turned, even and in the case that all the second order tensor elements

are independent and non-zero. This means that the  $b_0$ ,  $b_2$ ,  $b_4$ ,  $d_2$  and  $d_4$  coefficients which are the only results that DFT provides, in general, may be affected by tensor elements that the Equations 3.8-3.12 of the trigonal symmetry do not take into account. For that reasons and in order to have an estimation of Equation 3.6 parameters it was chosen to complete the analysis by fitting the SHG modulation on Equation 3.6 for all the pixels areas of each sample. The degree that the extracted results of the DFT and fitting procedures describe sufficiently the PSHG data of each sample can be quantitatively expressed through the ratio parameter values. As discussed in the previous section the value of this parameter was defined as the number of pixels with  $R^2 > 0.9$  divided by the total number of myosin sample's area pixels.

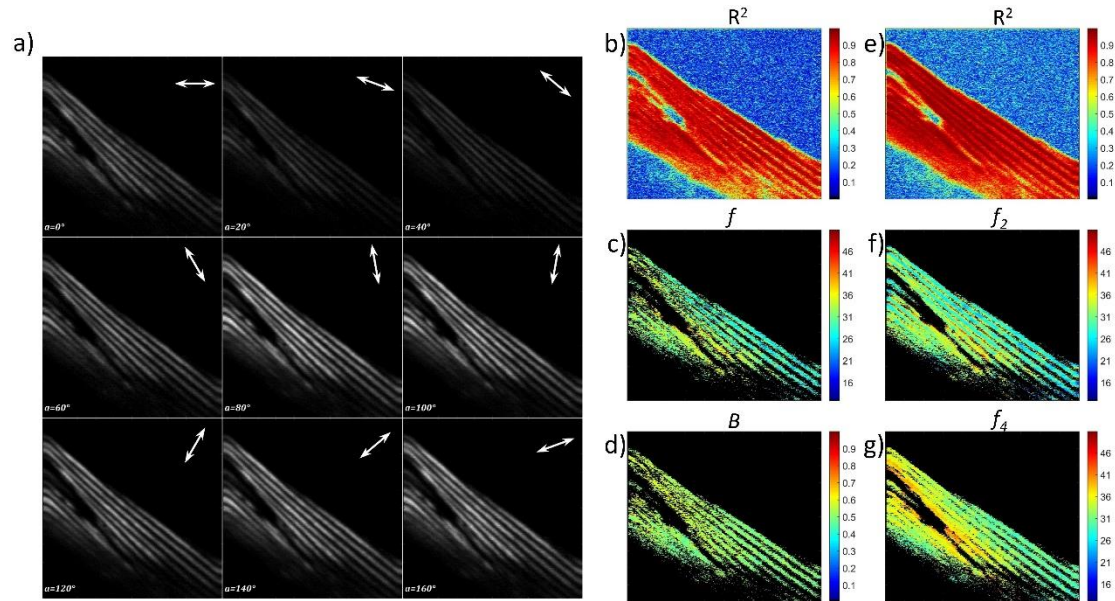


Figure 3.9 : Results of DFT analysis based on Equation 3.1 (b-d) (cylindrical symmetry model) and based on Equation 3.4 (e-g) (general model) for a PSHG dataset recorded from the middle body part of a 1 day old sample (a). a) 9 of the 18 PSHG dataset images. Each sub-image depicts the same area and the brightness is analog to the SHG recorded signals. The white arrow corresponds to the laser's linear polarization into the sample plane while at the bottom left of the sub-images there is the value of angle  $a$ . b) The color of each pixel corresponds to the value of  $R^2$  calculated for this pixel through the DFT analysis. Pixels with  $R^2 < 0.9$  have been excluded from further analysis and were displayed in black color in (c) and (d). c) Angle  $f$  computed values. d) Anisotropy parameter  $B$  computed values. e-g)  $R^2$  and angles  $f_2$  and  $f_4$  calculated values respectively.

In Figure 3.9 some representative results of our DFT analysis algorithm in a wild type 1 day old animal are depicted. Measurements were recorded from the striated muscles in the mid body region of the worm. The mean values of  $B$  ( $\langle B \rangle$ ) and angle  $f$  ( $\langle f \rangle$ ) as well as and the standard deviations of them, deriving from pixels with  $R^2 > 0.9$ , were calculated to be  $0.53 \pm 0.04$  and  $31.5^\circ \pm 3.4^\circ$  respectively. The value of  $\langle B \rangle$  considering Equation 1.17 matches with the lower brightness of Figure 3.9a for  $a=40^\circ$  (incoming polarization parallel to the sample symmetry axis) divided to  $a=140^\circ$  where the polarization is perpendicular and at the same time is in line with a previous study [49]. Specifically, through Equation 1.18 and due to the fact that the laser propagation direction is perpendicular to the muscle fibers, the value of  $\langle B \rangle$  corresponds to an effective angle of  $\theta_e$  around  $63^\circ \pm 1^\circ$ , which is in close proximity compared with the X-ray measured myosin helix angle which is  $68^\circ$  [49]. In the case of a perfectly cylindrical symmetric sample, the minimum expected value of  $\langle f \rangle$  is  $33^\circ$

considering that the angle between the direction of the initial laser's polarization (Figure 3.9a,  $\alpha=0^\circ$ ) and fiber's axis is around  $40^\circ$  and that myosin thick filaments are at an angle of  $5^\circ$ - $7^\circ$  to the muscle fiber [145]. However, by fitting SHG signal modulation for each point of this sample using Equation 3.6 it turns out that most of these points exhibit non zero S values, which means that the resulting angle of the DFT  $f_2$  can't be assumed equal with  $f$  due to the presence of  $\Delta f_2$  ( $f_2 = f - \Delta f_2$ ). Since the values of  $\chi_{15}$ ,  $\chi_{22}$ ,  $\chi_{31}$ ,  $\chi_{33}$  for each point are known after the fitting process it is feasible through evaluation of  $\Delta f_2$  value from Equation 3.14 to extract the angle  $f$  which encloses  $f_2$ . After the addition of the appropriate  $\Delta f_2$  value in each point, the mean value of the enclosed angle  $f$  resulted to be equal to  $33.5^\circ \pm 2.7^\circ$  which is even closer to the aforementioned expected value.

By comparing Figure 3.9c and Figure 3.9f it can be noticed that the calculated values of angles  $f$  and  $f_2$  are similar. However, in the second case, there is an increase in the number of pixels that present values with  $R^2 > 0.9$ , and the same holds by comparing Figure 3.9e with Figure 3.9b. This increase is mainly due to the fact that the values of angle  $f_4$ , calculating from the general model of Equation 3.4, differs from the  $f_2$  as shown Figure 3.9g and Figure 3.9f respectively. Furthermore, the increase of  $R^2$  can be expressed quantitatively through the estimation of the ratio parameter values. Thus the ratio parameter calculated to be 0.53 and 0.79 for the cylindrical symmetry and the general model respectively.

### 3.2.3 Results

PSHG measurements were performed in an attempt to monitor potential structural alterations in striated muscles of *C. elegans* samples during aging. Worms were irradiated at different time points for covering the whole animal life span. Figure 3.10 present the results of the implementation of the algorithm to a middle-aged *C. elegans* sample (6 day) while Figure 3.11 shows an old (9 day) worm. Measurements were recorded from the mid body part of the worms where the striated muscles are located.

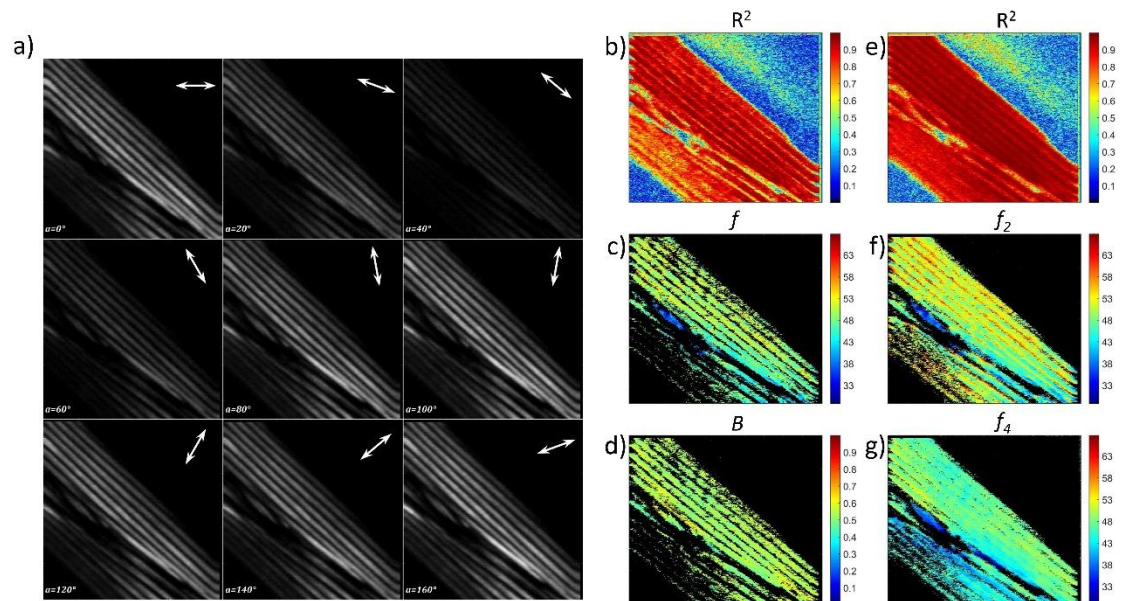


Figure 3.10 : Results of DFT analysis based on Equation 3.1 (b-d) and based on Equation 3.4 (e-g) for a PSHG dataset from a 6 days old sample (a). a) 9 of 18 PSHG dataset images. The

white arrow corresponds again to the laser's linear polarization into the sample plane and at the bottom left of each sub-image there is the value of angle  $a$ . b), e) The color of each pixel corresponds to the value of  $R^2$  calculated for this pixel through the DFT analysis. c) Angle  $f$  computed values. d) Anisotropy parameter  $B$  computed values, f) Angle  $f_2$  values and g) Angle  $f_4$  values. Pixels with  $R^2 < 0.9$  have been discarded from further analysis.

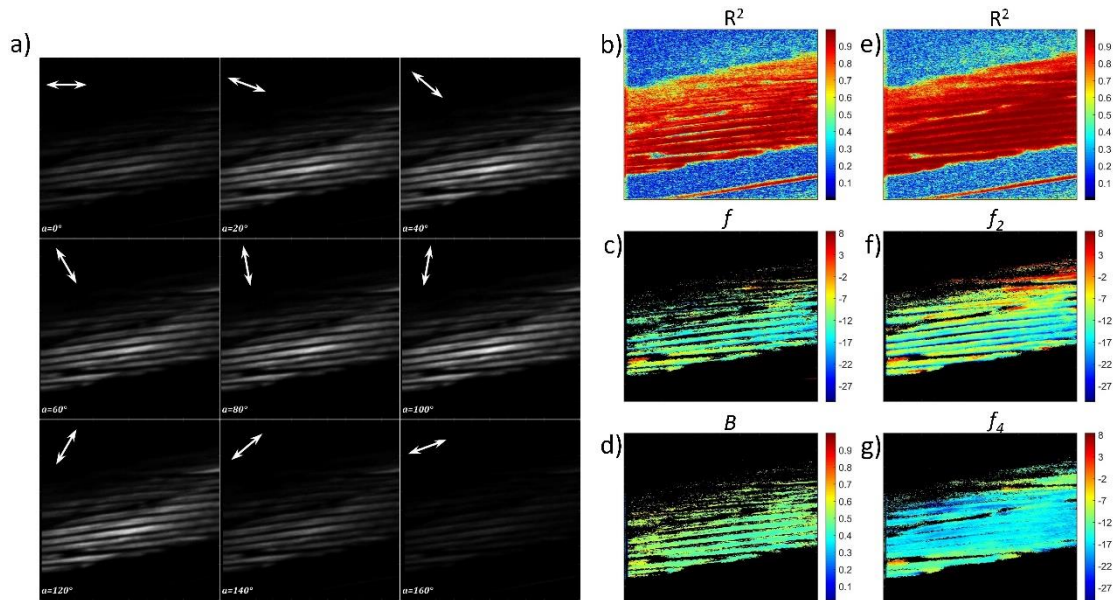


Figure 3.11 : Results similar as those depicted in Figure 3.9 and Figure 3.10 for a 9 days old sample. The red line at the bottom of (b) and (e) corresponds to a collagen fiber SHG signal from animal epidermis. These pixels are manually excluded from the other sub-images and from further processing.

For the cylindrical symmetry model and in order to examine potential  $B$  values variations during the aging of the *C. elegans*, the average values of  $\langle B \rangle$  for the three age groups (1d, 6d, and 9d) were calculated via our PSHG analysis based on Equation 3.1 and 3.2. 12 samples for each age category were tested. The obtained results presented in Figure 3.12 depicts that no significant difference was detected in the extracted  $B$  parameter values due to aging of the samples. Thus via this type of analysis is not feasible to obtain information related to structural changes in the striated muscles of the worms due to aging.

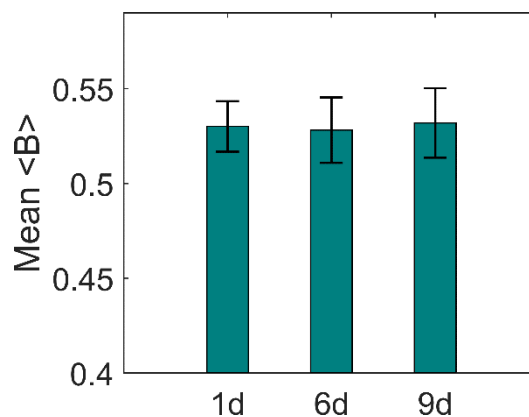


Figure 3.12 : Mean  $\langle B \rangle$  for 1d, 6d, and 9d worms. The error bars are the standard error of the mean (SEM) of each age group.  $n=12$  samples were irradiated in each case. The  $B$  values are similar, no significant difference is detected.

However, through our DFT analysis based on Equation 3.4 that represents the general model, and the fitting procedure in Equation 3.6 that indicates the trigonal symmetry model it was observed that the difference between the angles  $f_2$  and  $f_4$  was increased for the older age group.

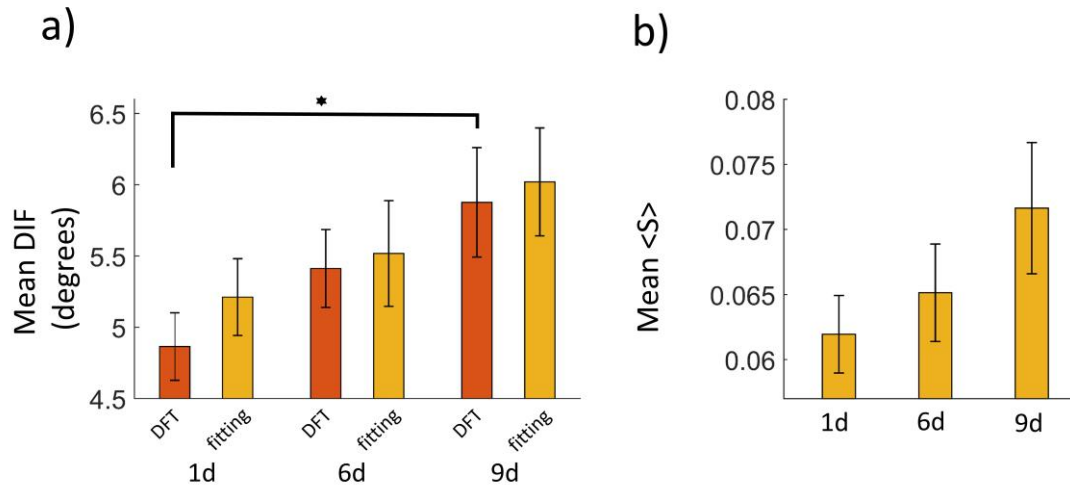


Figure 3.13 : a) Mean DIF computed with DFT based on Equation 3.4 and with fitting procedure based on Equation 3.6 respectively for the same samples of Figure 3.12. b) Mean  $\langle S \rangle$  (symmetry parameter) resulting from fitting procedure of (a). The error bars correspond to the SEM for each case. \* Statistically significant ( $<0.05$ ).

Figure 3.13a presents the average absolute difference in the values between the angles  $f_2$  and  $f_4$  (DIF) calculated with two different ways. In both cases, by implementing DFT analysis based on Equation 3.4 and by using fitting procedure based on Equation 3.6, older *C. elegans* samples present higher values compared to the younger ones. However, the mean DIF values showed a statistically significant increase for the 9d compared to the 1d samples only for the analysis derived from the general model.

Figure 3.13b depicts the calculated S mean values. Higher S values are an indicator that the trigonal symmetry is promoted against the cylindrical one. DIF raise of the older specimens accompanied with the increase of S values (Figure 3.13). Thus the recorded results show that the dominance of trigonal versus the cylindrical symmetry is enhanced in the striated muscles during the aging of the *C. elegans*.

In an attempt to investigate the symmetry that describes better the myosin alterations during the aging of the worms the ratio parameter values for the three approaches (cylindrical, trigonal and general models) were estimated. Figure 3.14 presents the mean ratio values for the 1d, 6d and 9d samples. In this figure is depicted that the trigonal model is preferable for the description of the three age groups in comparison with the classical cylindrical symmetry model. Moreover, Figure 3.14 shows that aging procedure is better delineated by employing DFT analysis based on Equation 3.4 (general model) rather with the fitting procedure based on Equation 3.6 that represents the trigonal symmetry model.

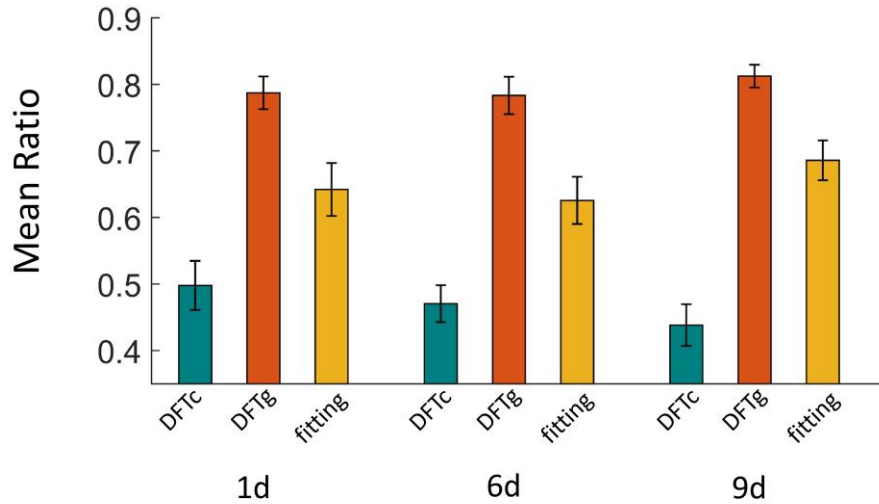


Figure 3.14 : Mean ratio values for 1, 6 and 9 days old samples obtained by: DFT analysis based on Equation 3.1 of cylindrical symmetry model (DFTc), DFT analysis based on Equation 3.4 of the general model (DFTg) and with the fitting procedure based on Equation 3.6 of trigonal symmetry model. The error bars correspond to the SEM for each case.  $n=12$  specimens for each age group.

### 3.2.4 Discussion

The results of this study show that the anisotropy parameter  $B$  extracted by DFT analysis from the widely used cylindrical symmetry PSHG model does not present any changes across the *C. elegans* lifespan. So it was not feasible by using this model for data analysis to detect myosin structural alterations during the aging of the worms. In addition, as Figure 3.14 presents the results from this model cannot adequately describe the PSHG data since the mean percentage of the pixels exhibit  $R^2$  values higher than 0.9 is lower than 50%. The fitting procedure with the trigonal symmetry model appears improved mean ratio results and an increase of the mean DIF values during *C. elegans* lifespan. By using the most general form of  $I_{SHG}$  dependence with respect to the angle  $a$  (Equation 3.4) the optimum score is obtained (up to 80%). The general model not only represents the PSHG data better but also the results of the DFT analysis based on this model that includes all possible structures provide an indication that the *C. elegans*' body striated muscles are undergoing structural alterations during aging. This indication is quantitatively expressed through the statistically significant increase of the mean DIF of the old (9d) compared with the young group of the worms (1d) (Figure 3.13). The DIF parameter for one sample defined as the average absolute difference of the angles  $f_2$  and  $f_4$  and this difference generally depends on the second order tensor elements and thus to the sample's structure. For example, in the case of a cylindrical symmetric sample, the expected DIF value is zero, whereas in the case of a trigonal symmetry the DIF value is estimated by Equations 3.14 and 3.15. Moreover, we showed that the observed raised of the DIF can be interpreted as an enhancement of the trigonal symmetry dominance to the cylindrical during aging. However, this does not imply that the younger samples should be exclusively described via a cylindrical symmetry model since they also present noticeable non-zero values of  $S$  (Figure 3.13b) and lower values of the ratio parameter compared to the other models (Figure 3.14).

A very recent study [141] has observed that there is a transition of SHG modulation with respect to the laser polarization in rat ventricles myosin filaments from a cylindrical to trigonal symmetry line profile during aging. The obtained results are in accordance with our study. In addition, they suggested that this transition may be due to the reduction of  $\alpha/\beta$  myosin isoforms ratio which their main difference lays in their head region. Nevertheless, as and in our case it is cannot be claimed that the detected changes in SHG modulation are exclusively arising from the enhancement of the presence of trigonal symmetry. Figure 3.14 demonstrates that for all the age groups the results of the DFT analysis based on the general model describe better the PSHG data. The following factors can interpret this behavior: possible failure in the accurate determination of the total minimum and/or the need for using an even more complicated model that take into account more symmetries than this of the trigonal one. Summarizing the findings presented herein suggest that the very promising modality of PSHG can be used as diagnostic tool for detecting myosin structural changes in the striated muscles of wild type *C. elegans* during their lifespan.

## Chapter 4 - NLOM for material characterization

As mentioned in the first chapter, NLOM microscopy can also be used to characterize and image various materials beyond biological samples. During the last part of this study NLOM techniques were employed as non-invasive, high resolution tools for cultural heritage studies. Specifically, in the framework of the thesis a specially designed algorithm was constructed for the precise identification of the different layers based on the collected MPEF signals from the artworks. Moreover, NLOM imaging combined with optoacoustic measurements and it was shown that they can provide new, valuable insights for the layers characterization of artefacts and for restoration procedures.

### 4.1 Introduction

Non-linear image contrast have been proven to be powerful diagnostic tools for cultural heritage (CH) studies, facilitating the accurate control of any cleaning interventions[146]. CH artefacts can strongly benefit from *in-situ* non-destructive testing methods, providing fruitful key information such as the determination of the different layers and their precise thickness or surface topography, revealing the cracks in the layers. Non-linear techniques can also define the concentration, shape and orientation of particles. Most of the optical properties, such as the absorption and luminescence of each component of the layers (binding media, varnishes, etc), can be studied. Recent work has demonstrated the potential of non-linear imaging techniques for depth-resolved imaging of materials in CH, such as fresh and aged varnishes [147][148], lining glues [149][150], historical coatings [151], parchments [9], paint [10] and the corrosion layer in metal-based artefacts [152]. Following presented some characteristic non-linear images from CH objects.

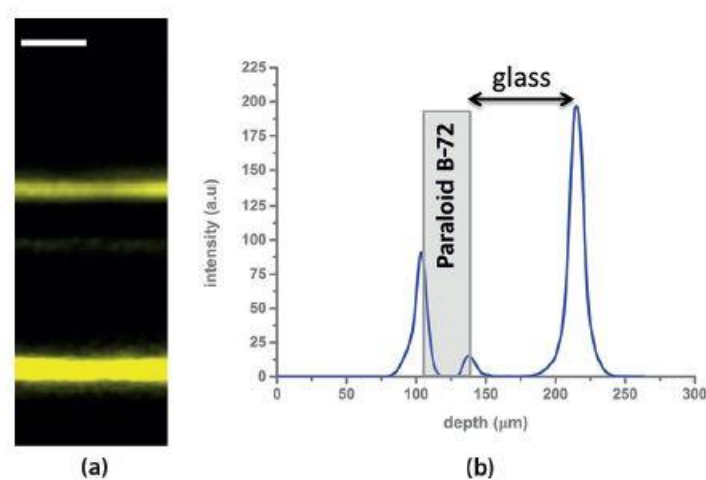


Figure 4.1 : (a) THG cross-sectional imaging of a Paraloid B-72 sample; and (b) the plot of the pixel brightness distribution across a central vertical line of image (a) (scale bar: 30  $\mu\text{m}$ ) [146].

Firstly, NLOM modalities can be employed for the precise determination of the thickness of varnishes commonly used as protective layers in CH objects. The sample in Figure 4.1 is a layer of a Paraloid B-72 film on a thin UV transparent glass imaged via THG microscopy. The THG arises from the three interfaces (air-varnish, varnish-glass, glass-air). The signals recorded by employing the same setup of Chapter 2 in the transmission mode. The distance of

the first two peaks of Figure 4.1b corresponds to the varnish thickness which verified by measuring the sample thickness with a mechanical profilometer [146][153][154][149].

Moreover, the layer thicknesses of a sample that simulates a work of art can be estimated by MPEF microscopy.

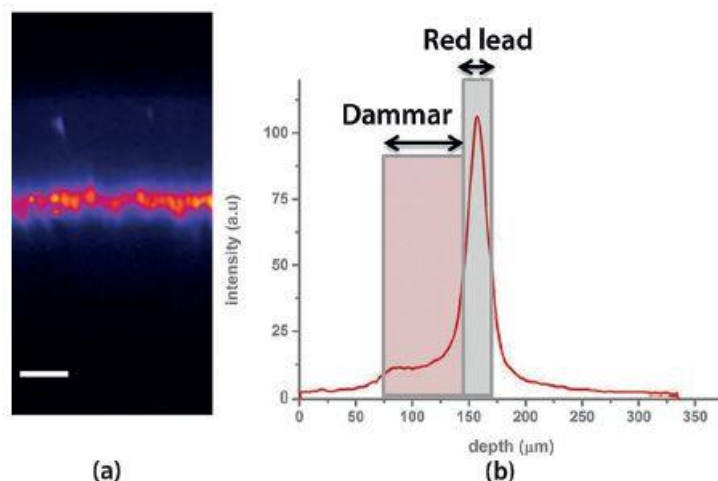


Figure 4.2 : (a) MPEF cross-sectional non-linear image of a model multi-layer sample that contains a layer of paint (red lead) and a layer of varnish (dammar); (b) plots of the pixel brightness distribution across a central vertical line of image (a) [146]. Signals detected in the reflection mode.

Two different intensity levels of fluorescence signal are presented in Figure 4.2(a), arising from the different layers. A low-intensity MPEF arises from the layer of dammar, while the layer of paint emits a higher intensity fluorescence signal. The pixel brightness across a central vertical line provides a quantitative view of the signal distribution of the model multi-layer painted sample (Figure 4.2b). The thickness of the two layers was measured by calculating the full width at half maximum (FWHM) of the resulting curves, which is 75  $\mu\text{m}$  for the varnish and 23  $\mu\text{m}$  for the paint layer (red lead). Based on the intensity of the collected MPEF signals, this technique allows the discrimination, rather than the determination, of the chemical composition of the protective (varnish) layer and the paint layer. No THG signal was detected from the sample in the transmission mode. This is due to the high absorption of the materials (red lead and dammar) in the UV region of the spectrum. Consequently, the weak THG signals generated from the interfaces of the multi-layer sample at 343 nm are reabsorbed by the material [146][10].

In addition to information on the thickness of varnishes for the preservation of works of art, NLOM microscopy can provide valuable information on another very important material for this field, starch glue [149]. In Chapter 1 is mentioned that amylopectin is considered the main molecular source of SHG signals in starch granules whereas at the same time its radial orientation can be depicted by PSHG measurements as also presented in the following Figure.

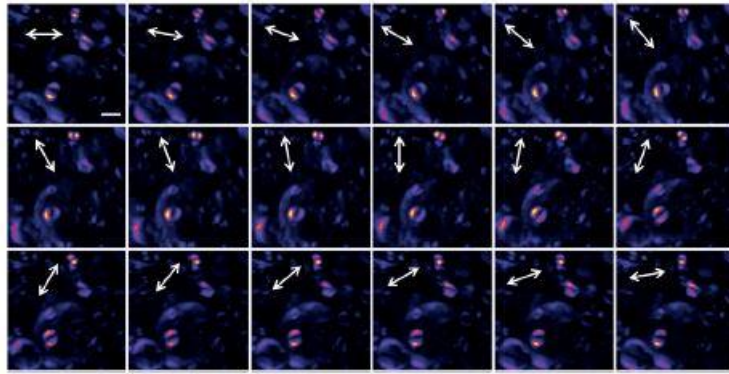


Figure 4.3 : PSHG imaging from a starch-based glue. The incident excitation linear polarization rotates clockwise between  $0^\circ$  and  $170^\circ$  in steps of  $10^\circ$  (white arrows) (scale bar:  $10 \mu\text{m}$ ) [146].

In a recent study of our group, PSHG microscopy was employed as a new diagnostic tool for the quantitative discrimination between aged and fresh starch-based glues [150]. It was found that in naturally aged glues, the SHG effective orientation (SHG angle  $\theta$ ) of the starch is shifted to significantly higher values, in comparison to the fresh granules and this was attributed to the hydration level of the starch granules.

#### 4.2 Specially designed deconvolution algorithm for MPEF signals

The way in which the thickness of the varnish was measured in Figure 4.2 is an estimation, as it does not take into account the fact that at some point the recorded MPEF signal may come from both materials. However, the accurate determination of varnish thickness is crucial for CH restoration [146]. For that reason, during this thesis, a mathematical model was proposed and used by a specially designed deconvolution algorithm [8]. Moreover, in order to evaluate the performance of this algorithm to real case sample, the setup of this thesis (Figure 1.13) was evolved via the development of a LabView program to scanning up to  $2 \text{ cm}^2$  areas based only on the movement of the translation stages.

From a mathematical standpoint, the depth-resolved MPEF signal (along the Z-axis) was considered to be the summation of two terms involving the nonlinear interaction of the focused Gaussian beam with the successive varnish and paint layers (Figure 4.4). The first term represents the convolution of the axial beam's profile raised to the third power, with a top-hat function corresponding to the overlying varnish layer. The exponentiation of the beam's profile is linked to the nonlinearity order based on the spectral characteristics of the materials. The investigated fresh varnishes present high transparency in the visible and infrared regions, while they absorb strongly in the near-UV part, thus demonstrating a predominant three-photon excitation mechanism for the employed excitation wavelength [154]. Similarly, the second term represents the convolution of the squared axial profile with a second top-hat function standing for the underlying paint layer, which presents strong two-photon absorption properties. In addition, it must take into account the scattering effects on the fundamental beam, as well as the partial re-absorption of the emitted fluorescence into the paint layer's bulk, by inserting an exponential attenuation factor in the second convolution term. The absorption effects in the varnish layer were considered to be negligible within the employed excitation and detection range, as has been shown in previous studies [147][10].

The above mathematical model is used in an optimization fitting procedure for the determination of the first top-hat function's amplitude and width, which provides the varnish thickness and the relative depth of the varnish-paint interface. Since the scattering of the fundamental beam into the paint is very high, the second convolution term of the algorithm provided practically information about the maximum penetration depth, rather than the layer's thickness. The resulting depth values were finally corrected for apparent depth distortion due to the refractive index mismatch between air ( $n=1$ ) and measured layers ( $n \approx 1.5$ ).

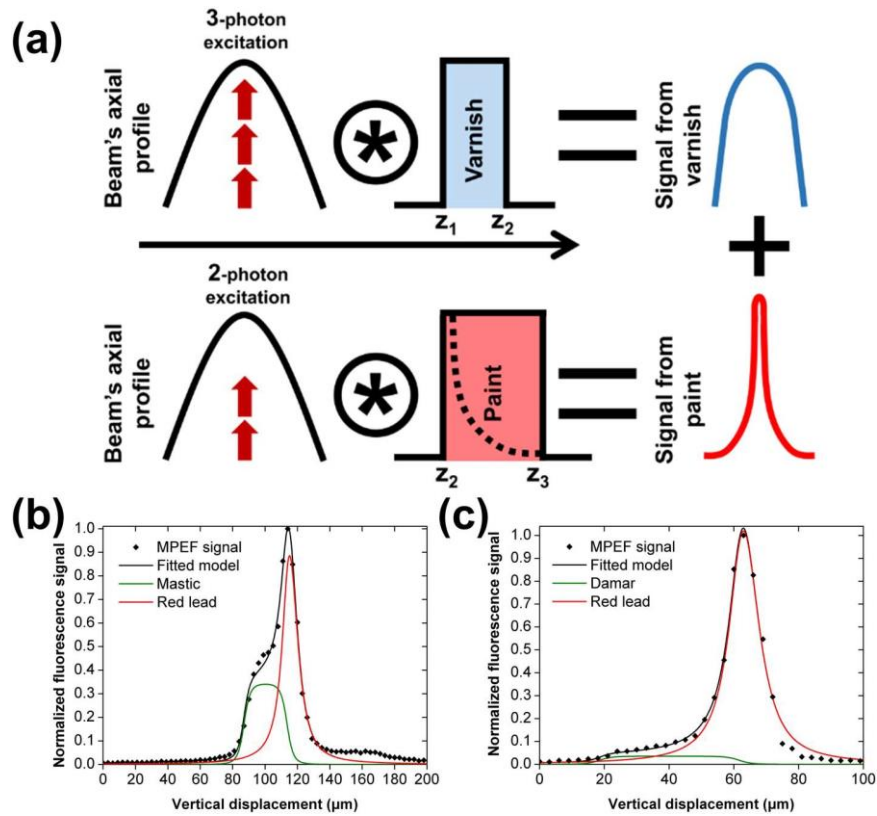


Figure 4.4 : MPEF signal discrimination in Z-Scan measurements. (a) Graphical illustration of the fitted model resulting from the summation of two convolution functions involving axial signal profiles and layer thicknesses, represented as top-hat functions. The optical attenuation has been additionally considered due to scattering and fluorescence re-absorption effects. (b) Z-Scan MPEF measurement of a red lead painting sample covered with mastic in the reflection mode. The fitted model (black line,  $R^2=0.99$ ) was used to decouple the recorded response (black points) into respective signal contributions arising from varnish (green line) and paint (red line). (c) Similar data are presented for a painting sample covered with dammar ( $R^2=0.99$ ).

The capability of the developed algorithm in regard to MPEF signal discrimination was initially evaluated by performing Z-Scan measurements in two painting samples covered with mastic and dammar varnishes, respectively (Figure 4.4 b and c). Black points correspond to the recorded MPEF signal values as a function of depth, whereas black curve represents the optimum fitting of experimental data according to the employed convolution model ( $R^2=0.99$  for both cases), which can be subsequently decoupled into distinct contributions arising from each layer. More specifically, the green curve stands for the first convolution term, representing the interaction of excitation beam with the varnish, whereas the red curve describes the second term indicating the penetration depth of the fundamental beam into the paint's bulk. In the case of mastic sample (Figure 4.4b), the varnish boundaries were

estimated at  $z_1$  87  $\mu\text{m}$  and  $z_2$  114  $\mu\text{m}$ , respectively, yielding an uncorrected thickness equal to 27  $\mu\text{m}$ . By multiplying the latter value with the apparent depth correction factor ( $\sim 1.6$ ) [155], a final varnish thickness of 43  $\mu\text{m}$  is calculated. On the other hand, the  $1/e$  width of the red curve was estimated at 15  $\mu\text{m}$ , yielding a penetration of around 24  $\mu\text{m}$  into the paint.

Similarly, the dammar sample's varnish boundary values were calculated at  $z_1$  19  $\mu\text{m}$  and  $z_2$  62  $\mu\text{m}$ , providing a final distortion-corrected thickness of  $\sim 69$   $\mu\text{m}$  (Figure 4.4c). As expected, the penetration depth into the paint was found to be identical to the previous case. It is also worth mentioning that the amplitudes of the mastic and dammar signal contributions present a significant difference by almost an order of magnitude, thus allowing for their reliable identification through the intensity-based analysis of the recorded MPEF. The increased absorption coefficient of mastic at 343 nm (three-photon excitation in our case) can be linked with the higher MPEF intensity signals recorded from this material. Thus this technique based on the intensity of the collected MPEF signals can discriminate these two common used CH natural varnishes.

Moreover, in this study presented for the first time, to the best of our knowledge, the feasibility to act synergistically NLOM with photoacoustic (PA) imaging techniques for CH diagnosis. PA measurements (Figure 4.5) performed from Dr Tserevelakis (Zacharakis lab, IESL). Briefly PA imaging has been very lately proposed as a highly promising diagnostic tool for CH, which is able to provide optical absorption contrast through the detection of ultrasonic waves following excitation with pulsed laser radiation. Due to the up to three orders of magnitude lower attenuation coefficient of ultrasound compared to NIR radiation, imaging depths of several mm can be achieved in turbid media with a spatial resolution determined by acoustic detection parameters rather than by focused light [156]. Such novel PA imaging approaches have already been applied in CH for the visualization of hidden underdrawings in paintings [157], the thickness measurement of paint layers [158], as well as the uncovering of content in layered documents [159]. The painting samples prepared for this work aimed to replicate real easel paintings on a small scale. Initially, patterns of parallel lines ( $\sim 0.5$  mm thick) were produced on prepared canvas by employing a graphite pencil representing the sketch layer of the painting. Subsequently, red lead pigment was mixed with an acrylic binder to produce an acrylic paint that was applied by brush over the sketch of the canvas. A thin layer of varnish (mastic or dammar) was finally applied on the paint to simulate the structure of realistic paintings.

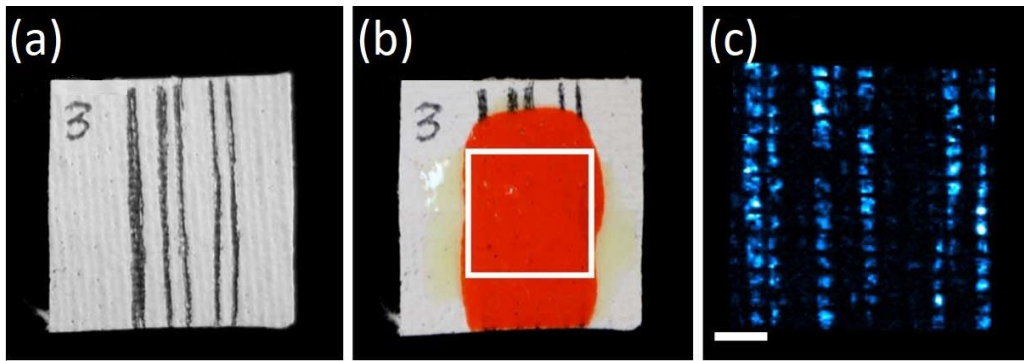


Figure 4.5 : (a) Brightfield image of a mock-up canvas sample ( $22 \times 22 \text{ mm}^2$ ) with several sketch lines drawn by pencil. (b) Same mock-up following the application of red lead paint and mastic layers. The white square ( $1 \times 1 \text{ cm}^2$ ) indicates the central region imaged using the PA modality. (c) Maximum amplitude projection PA image of underlying pencil lines for the selected field of view (scale bar, 2 mm).

Figure 4.6a shows the central cross-sectional MPEF image of Figure 4.5b sample (perpendicular to sketch lines). The depicted region is 1 cm and  $385 \mu\text{m}$  in the X, Z direction, sampled with 200 by 80 pixels, respectively. The small regions characterized by a total absence of MPEF signals can be attributed to the high inhomogeneity of the handmade painting sample

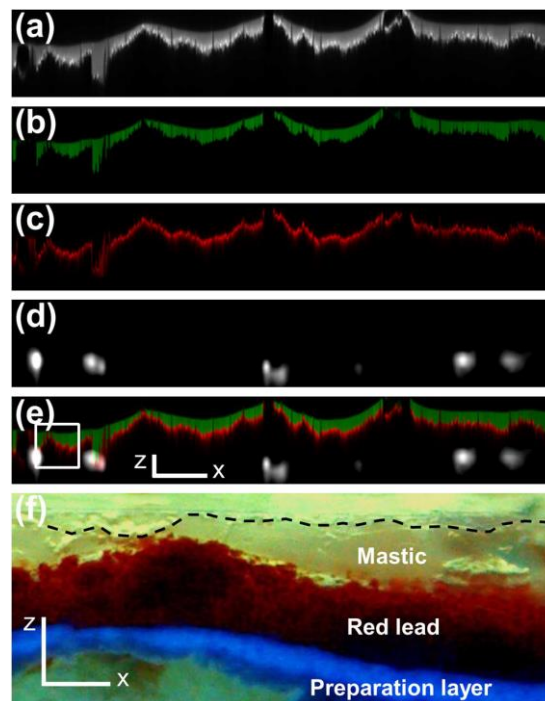


Figure 4.6 : Combined MPEF and PA cross-sectional imaging. (a) Raw MPEF image. (b) Unmixed MPEF image of the mastic layer. (c) Unmixed MPEF image of the red lead paint layer. (d) PA image of the underlying pencil sketch. (e) Composite MPEF and PA image (scale bar Z,  $100 \mu\text{m}$ ; scale bar X, 1 mm). (f) Brightfield image of the region indicated with a white square in (e) using near-UV light. The black dashed line represents the border of the mastic layer. Both scale bars in the Z and X dimensions correspond to  $100 \mu\text{m}$ .

By applying the developed algorithm, the mixed information carried by the MPEF image was decomposed into relative contributions from the mastic layer (Figure 4.6b) and red lead paint

(Figure 4.6c) presented with green and red pseudo colors, respectively. The cross-sectional PA image from the same region shown in Figure 4.6d reveals explicitly the distribution of graphite along the selected central line. A composite image merging the sections presented in Figure 4.6 b-d is shown in Figure 4.6e, delineating the full stratigraphy of the investigated mock-up sample at high resolution and contrast specificity within the limits of the combined imaging approaches. The superposition of the profiles in the Z-axis has been achieved according to the mean thickness of the mock-up at the measurement region, as has been estimated by brightfield microscopy observations at the edges of the sample. Finally, to validate our results, we cut the mock-up sample at the imaged profile's location and obtained cross-sectional brightfield microscopy images to use them for a direct comparison with the composite image. Figure 4.6f shows a near-UV brightfield view of the sample's cross section at the region indicated with a white square in Figure 4.6e. As is clear from the images, the two regions present an obvious similarity in terms of structure, morphology, and layer spatial distribution on the canvas. Furthermore, from a quantitative point of view, the extracted mastic layer thickness value for the right section of the region of interest ( $\sim 75 \mu\text{m}$ ) is in very good agreement with Figure 4.6f, thus confirming the precision of our measurements following convolution-based data processing.

This study has provided experimental evidence that the effective combination of these two diagnostic techniques (NLOM and PA) can offer highly complementary information, allowing for the accurate mapping and delineation of different stratigraphic layers in a painted artwork.

## Chapter 5 - Conclusions

The obtained results of this thesis reveal that NLOM microscopy can be used not only for the characterization and the visualization of tissues and cells, but through appropriate imaging and state of the art data analysis these techniques can give new perspectives on fundamental biological problems as well and on the early and accurate diagnosis of serious diseases such as cancer.

Indeed, in Chapter 2 presented that THG imaging microscopy can be used to differentiate malignant from benign unlabeled human breast biopsies and distinguish the different grades of cancer. In the framework of this thesis, towards the application of such technologies to clinic, a deep learning algorithm was developed for the analysis of the recorded non-linear images, allowing thus the accurate and fast -less than a second- diagnosis of specimens. The main advantages of the proposed technology include the reliable outputs in cancer diagnosis, the speed and the utilization of unstained tissue. The implementation of this technique can potentially act synergistically with standard histopathology for increasing cancer detection rates and considerably decreasing the required time for biopsies' characterization. The application of THG imaging implemented with the model developed herein and in conjugation with the recent advances in laser scanning microscopes, opens the road to digital pathology in benefit to patients and healthcare systems.

One of the most important advantages of NLOM is the ability to record multiple non-linear signals simultaneously and with the use of the same setup. The findings presented in the third Chapter of the thesis suggest that PSHG, which is a non-linear, label free and non-destructive imaging technique, can also evaluate the tumor state, differentiate malignant from benign breast tissue samples and distinguish the different grades of cancer based on the quantitative parameters values of  $B$  and ratio. Specifically, the obtained PSHG data showed increased calculated second-harmonic anisotropy parameter ( $B$ ) values, which is an indication for collagen structure organisation in tumor progression. Moreover, the proposed biophysical model that was verified via simulation analysis, correlated SHG anisotropy values with the mechanical tension applied to collagen during cancer progression.

Except from the application of PSHG on breast cancer tissue discrimination, it was shown that PSHG modality can be used as an innovative diagnostic tool for studying aging phenomena. Specifically, indications of myosin structural alterations was detected, in the striated muscles of wild type *C. elegans* during their lifespan, via PSHG microscopy. Through the implementation of the widely used, classical, cylindrical symmetry model and the calculation of the anisotropy parameter values it is not feasible to detect alterations and discriminate the different age groups. Nevertheless, the application of a trigonal symmetry and a general model in order to describe the extracted PSHG data allow the age classification of the nematodes based on of the difference in spectral phases derived from the Fourier Transform analysis. In addition, the obtained results suggest the enhancement of the trigonal symmetry dominance against cylindrical one in the striated muscles during the aging of the worms.

In the future further studies on mutants, such as animals that promote longevity and the implementation of models that take into account more symmetries for the data processing is expected to attribute additional insights for the thorough clarification of the morphological changes that undergoes the structure of the myosin molecules during aging. Moreover, several

muscle diseases are associated with changes in myosin molecules. Thus, it would be very interesting the investigation of the alterations in the sub-cellular structure of myosin with the disease progression via the performance of PSHG measurements.

Concluding for biological applications this research provided an initial step ahead towards the implementation of NLOM modalities in preclinical and/or clinical studies.

In the last part of this thesis an algorithm developed to accurately determine the varnish protective layer thickness in artworks based on MPEF measurements. It was demonstrated the usefulness of NLOM technique for providing new insights in Cultural Heritage studies as a non-invasive diagnostic tool.

## Chapter 6 - Bibliography

- [1] R. W. Boyd, *Nonlinear Optics*. San Diego, USA: Academic Press Inc., 1992.
- [2] E. Garmire, “Nonlinear optics in daily life,” *Opt. Express*, vol. 21, no. 25, p. 30532, Dec. 2013, doi: 10.1364/oe.21.030532.
- [3] B. Masters and P. So, *Handbook of biomedical nonlinear optical microscopy*. New York, USA: Oxford University Press, Inc., 2008.
- [4] T. Meyer, M. Schmitt, B. Dietzek, and J. Popp, “Accumulating advantages, reducing limitations: Multimodal nonlinear imaging in biomedical sciences - The synergy of multiple contrast mechanisms,” *J. Biophotonics*, vol. 6, no. 11–12, pp. 887–904, Dec. 2013, doi: 10.1002/jbio.201300176.
- [5] V. Tsafas *et al.*, “Polarization-dependent second-harmonic generation for collagen-based differentiation of breast cancer samples,” *J. Biophotonics*, vol. 13, no. 10, Oct. 2020, doi: 10.1002/jbio.202000180.
- [6] J. T. Trachtenberg *et al.*, “Long-term in vivo imaging of experience-dependent synaptic plasticity in adult cortex,” *Nature*, vol. 420, no. 6917, pp. 788–794, Dec. 2002, doi: 10.1038/nature01273.
- [7] G. J. Tserevelakis, G. Filippidis, E. V. Megalou, C. Fotakis, and N. Tavernarakis, “Cell tracking in live *Caenorhabditis elegans* embryos via third harmonic generation imaging microscopy measurements,” *J. Biomed. Opt.*, vol. 16, no. 4, p. 046019, 2011, doi: 10.1117/1.3569615.
- [8] G. J. Tserevelakis, V. Tsafas, K. Melessanaki, G. Zacharakis, and G. Filippidis, “Combined multiphoton fluorescence microscopy and photoacoustic imaging for stratigraphic analysis of paintings,” *Opt. Lett.*, vol. 44, no. 5, p. 1154, Mar. 2019, doi: 10.1364/ol.44.001154.
- [9] G. Latour, L. Robinet, A. Dazzi, F. Portier, A. Deniset-Besseau, and M.-C. Schanne-Klein, “Correlative nonlinear optical microscopy and infrared nanoscopy reveals collagen degradation in altered parchments,” *Sci. Rep.*, vol. 6, no. 1, pp. 1–10, 2016.
- [10] G. Filippidis, G. J. Tserevelakis, A. Selimis, and C. Fotakis, “Nonlinear imaging techniques as non-destructive, high-resolution diagnostic tools for cultural heritage studies,” *Appl. Phys. A*, vol. 118, no. 2, pp. 417–423, 2015.
- [11] G. Violakis, V. Tsafas, G. Filippidis, and S. Pissadakis, “Electrically Poled, MNA-Microstructured Optical Fibers for Second Harmonic Generation,” *IEEE J. Sel. Top. Quantum Electron.*, vol. 26, no. 4, Jul. 2020, doi: 10.1109/JSTQE.2019.2958995.
- [12] S. Kujala, A. Mannila, L. Karvonen, K. Kieu, and Z. Sun, “Natural silk as a photonics component: A study on its light guiding and nonlinear optical properties,” *Sci. Rep.*, vol. 6, no. 1, pp. 1–9, 2016.
- [13] H. An and S. Fleming, “Investigating the effectiveness of thermally poling optical fibers with various internal electrode configurations,” *Opt. Express*, vol. 20, no. 7, pp. 7436–7444, 2012.
- [14] M. Zhao *et al.*, “Atomically phase-matched second-harmonic generation in a 2D crystal,” *Light Sci. Appl.*, vol. 5, no. 8, pp. e16131–e16131, Mar. 2016, doi: 10.1038/lsa.2016.131.
- [15] L. M. Malard, T. V Alencar, A. P. M. Barboza, K. F. Mak, and A. M. De Paula, “Observation of intense second harmonic generation from MoS<sub>2</sub> atomic crystals,” *Phys. Rev. B*, vol. 87, no. 20, p. 201401, 2013.

- [16] R. Beams *et al.*, “Characterization of few-layer 1T' MoTe<sub>2</sub> by polarization-resolved second harmonic generation and Raman scattering,” *ACS Nano*, vol. 10, no. 10, pp. 9626–9636, 2016.
- [17] R. L. Siegel, K. D. Miller, and A. Jemal, “Cancer statistics, 2020,” *CA. Cancer J. Clin.*, vol. 70, no. 1, pp. 7–30, 2020.
- [18] V. Parodi, E. Jacchetti, R. Osellame, G. Cerullo, D. Polli, and M. T. Raimondi, “Nonlinear optical microscopy: From fundamentals to applications in live bioimaging,” *Front. Bioeng. Biotechnol.*, vol. 8, 2020.
- [19] W. Lee, M. M. Kabir, R. Emmadi, and K. C. Toussaint Jr, “Third-harmonic generation imaging of breast tissue biopsies,” *J. Microsc.*, vol. 264, no. 2, pp. 175–181, 2016.
- [20] N. V Kuzmin *et al.*, “Third harmonic generation imaging for fast, label-free pathology of human brain tumors,” *Biomed. Opt. Express*, vol. 7, no. 5, pp. 1889–1904, 2016.
- [21] K. König, A. Ehlers, I. Riemann, S. Schenkl, R. Bückle, and M. Kaatz, “Clinical two-photon microendoscopy,” *Microsc. Res. Tech.*, vol. 70, no. 5, pp. 398–402, 2007.
- [22] D. R. Rivera *et al.*, “Compact and flexible raster scanning multiphoton endoscope capable of imaging unstained tissue,” *Proc. Natl. Acad. Sci.*, vol. 108, no. 43, pp. 17598–17603, 2011.
- [23] F. Akhoundi, Y. Qin, N. Peyghambarian, J. K. Barton, and K. Kieu, “Compact fiber-based multi-photon endoscope working at 1700 nm,” *Biomed. Opt. Express*, vol. 9, no. 5, pp. 2326–2335, 2018.
- [24] D. M. Huland *et al.*, “In vivo imaging of unstained tissues using long gradient index lens multiphoton endoscopic systems,” *Biomed. Opt. Express*, vol. 3, no. 5, pp. 1077–1085, 2012.
- [25] W. Liang, G. Hall, B. Messerschmidt, M.-J. Li, and X. Li, “Nonlinear optical endomicroscopy for label-free functional histology in vivo,” *Light Sci. Appl.*, vol. 6, no. 11, pp. e17082–e17082, 2017.
- [26] D. Y. Kim *et al.*, “Lissajous scanning two-photon endomicroscope for in vivo tissue imaging,” *Sci. Rep.*, vol. 9, no. 1, pp. 1–8, 2019.
- [27] W. Ren *et al.*, “Visualization of lymphatic vascular invasion in breast cancer by multiphoton microscopy,” *Lasers Med. Sci.*, vol. 36, no. 2, pp. 303–309, 2021.
- [28] B. Cromey, A. McDaniel, T. Matsunaga, J. Vagner, K. Q. Kieu, and B. Banerjee, “Pancreatic cancer cell detection by targeted lipid microbubbles and multiphoton imaging,” *J. Biomed. Opt.*, vol. 23, no. 4, p. 46501, 2018.
- [29] T. Matsui *et al.*, “Non-labeling multiphoton excitation microscopy as a novel diagnostic tool for discriminating normal tissue and colorectal cancer lesions,” *Sci. Rep.*, vol. 7, no. 1, pp. 1–9, 2017.
- [30] A. R. Ahmed *et al.*, “Directly imaging the localisation and photosensitization properties of the pan-mTOR inhibitor, AZD2014, in living cancer cells,” *J. Photochem. Photobiol. B Biol.*, vol. 213, p. 112055, 2020.
- [31] M. Gu, H. C. Bao, and J. L. Li, “Cancer-cell microsurgery using nonlinear optical endomicroscopy,” *J. Biomed. Opt.*, vol. 15, no. 5, p. 50502, 2010.
- [32] E. Gavgiotaki *et al.*, “Third Harmonic Generation microscopy as a reliable diagnostic tool for evaluating lipid body modification during cell activation: The example of BV-2 microglia cells,” *J. Struct. Biol.*, vol. 189, no. 2, pp. 105–113, 2015.

- [33] M. Mari, G. Filippidis, K. Palikaras, B. Petanidou, C. Fotakis, and N. Tavernarakis, “Imaging ectopic fat deposition in *Caenorhabditis elegans* muscles using nonlinear microscopy,” *Microsc. Res. Tech.*, vol. 78, no. 6, pp. 523–528, 2015.
- [34] J. Yuan, W. Deng, J. Cha, X. Sun, J.-P. Borg, and S. K. Dey, “Tridimensional visualization reveals direct communication between the embryo and glands critical for implantation,” *Nat. Commun.*, vol. 9, no. 1, pp. 1–13, 2018.
- [35] A. L. Lopez and I. V. Larina, “Second harmonic generation microscopy of early embryonic mouse hearts,” *Biomed. Opt. Express*, vol. 10, no. 6, pp. 2898–2908, 2019.
- [36] A. L. Williams and B. L. Bohnsack, “Multi-photon time lapse imaging to visualize development in real-time: Visualization of migrating neural crest cells in Zebrafish embryos,” *J. Vis. Exp. JoVE*, no. 126, 2017.
- [37] C. C. Moura, K. N. Bourdakos, R. S. Tare, R. O. C. Oreffo, and S. Mahajan, “Live-imaging of bioengineered cartilage tissue using multimodal non-linear molecular imaging,” *Sci. Rep.*, vol. 9, no. 1, pp. 1–9, 2019.
- [38] B. C. Syverud, M.-A. Mycek, and L. M. Larkin, “Quantitative, label-free evaluation of tissue-engineered skeletal muscle through multiphoton microscopy,” *Tissue Eng. Part C Methods*, vol. 23, no. 10, pp. 616–626, 2017.
- [39] K. Huemer, J. M. Squirrell, R. Swader, D. C. LeBert, A. Huttenlocher, and K. W. Eliceiri, “zWEDGI: wounding and entrapment device for imaging live zebrafish larvae,” *Zebrafish*, vol. 14, no. 1, pp. 42–50, 2017.
- [40] J. Rico-Jimenez *et al.*, “Non-invasive monitoring of pharmacodynamics during the skin wound healing process using multimodal optical microscopy,” *BMJ Open Diabetes Res. Care*, vol. 8, no. 1, p. e000974, 2020.
- [41] G. A. Blab, P. H. M. Lommerse, L. Cognet, G. S. Harms, and T. Schmidt, “Two-photon excitation action cross-sections of the autofluorescent proteins,” *Chem. Phys. Lett.*, vol. 350, no. 1–2, pp. 71–77, 2001.
- [42] X. Deng, Z. Zhuang, H. Liu, P. Qiu, and K. Wang, “Measurement of 3-photon excitation and emission spectra and verification of Kasha’s rule for selected fluorescent proteins excited at the 1700-nm window,” *Opt. Express*, vol. 27, no. 9, p. 12723, Apr. 2019, doi: 10.1364/oe.27.012723.
- [43] L. Moreaux, O. Sandre, and J. Mertz, “Membrane imaging by second-harmonic generation microscopy,” *J. Opt. Soc. Am. B*, vol. 17, no. 10, p. 1685, Oct. 2000, doi: 10.1364/josab.17.001685.
- [44] D. Oron, E. Tal, and Y. Silberberg, “Depth-resolved multiphoton polarization microscopy by third-harmonic generation,” *Opt. Lett.*, vol. 28, no. 23, pp. 2315–2317, 2003.
- [45] G. J. Tserevelakis, E. V. Megalou, G. Filippidis, B. Petanidou, C. Fotakis, and N. Tavernarakis, “Label-Free Imaging of Lipid Depositions in *C. elegans* Using Third-Harmonic Generation Microscopy,” *PLoS One*, vol. 9, no. 1, p. e84431, Jan. 2014, doi: 10.1371/journal.pone.0084431.
- [46] P. Stoller, K. M. Reiser, P. M. Celliers, and A. M. Rubenchik, “Polarization-modulated second harmonic generation in collagen,” *Biophys. J.*, vol. 82, no. 6, pp. 3330–3342, Jun. 2002, doi: 10.1016/S0006-3495(02)75673-7.
- [47] J. Duboisset, D. Aït-Belkacem, M. Roche, H. Rigneault, and S. Brasselet, “Generic model of the molecular orientational distribution probed by polarization-resolved second-harmonic generation,” *Phys. Rev. A - At. Mol. Opt. Phys.*, vol. 85, no. 4, p.

043829, Apr. 2012, doi: 10.1103/PhysRevA.85.043829.

- [48] S. V. Plotnikov, A. C. Millard, P. J. Campagnola, and W. A. Mohler, “Characterization of the myosin-based source for second-harmonic generation from muscle sarcomeres,” *Biophys. J.*, vol. 90, no. 2, pp. 693–703, 2006, doi: 10.1529/biophysj.105.071555.
- [49] F. Tiaho, G. Recher, and D. Rouède, “Estimation of helical angles of myosin and collagen by second harmonic generation imaging microscopy,” *Opt. Express*, vol. 15, no. 19, p. 12286, Sep. 2007, doi: 10.1364/oe.15.012286.
- [50] S. Psilodimitrakopoulos, I. Amat-Roldan, P. Loza-Alvarez, and D. Artigas, “Estimating the helical pitch angle of amylopectin in starch using polarization second harmonic generation microscopy,” *J. Opt.*, vol. 12, no. 8, p. 84007, 2010.
- [51] E. Pilling and A. M. Smith, “Growth ring formation in the starch granules of potato tubers,” *Plant Physiol.*, vol. 132, no. 1, pp. 365–371, 2003.
- [52] T. P. Coultate, *Food: the chemistry of its components*. Royal Society of Chemistry, 2009.
- [53] S. W. Chu *et al.*, “Amylopectin: origin of second harmonic generation in starch,” *Focus Microsc. (Krakov, April, 2009)*.
- [54] S. Psilodimitrakopoulos *et al.*, “Starch granules as a probe for the polarization at the sample plane of a high resolution multiphoton microscope,” in *Multiphoton Microscopy in the Biomedical Sciences VIII*, 2008, vol. 6860, p. 68600E.
- [55] J. Shimada, H. Kaneko, T. Takada, S. Kitamura, and K. Kajiwara, “Conformation of amylose in aqueous solution: small-angle x-ray scattering measurements and simulations,” *J. Phys. Chem. B*, vol. 104, no. 9, pp. 2136–2147, 2000.
- [56] L. Novotny and B. Hecht, *Principles of nano-optics*. Cambridge university press, 2012.
- [57] G. S. Kino and T. R. Corle, *Confocal scanning optical microscopy and related imaging systems*. Academic Press, 1996.
- [58] A. M. Kabel, “Tumor markers of breast cancer: New perspectives,” *J. Oncol. Sci.*, vol. 3, no. 1, pp. 5–11, Apr. 2017, doi: 10.1016/j.jons.2017.01.001.
- [59] L. Li *et al.*, “Visualization of Tumor Response to Neoadjuvant Therapy for Rectal Carcinoma by Nonlinear Optical Imaging,” *IEEE J. Sel. Top. Quantum Electron.*, vol. 22, no. 3, pp. 158–163, May 2016, doi: 10.1109/JSTQE.2015.2456108.
- [60] L.-H. Li *et al.*, “Monitoring neoadjuvant therapy responses in rectal cancer using multimodal nonlinear optical microscopy,” *Oncotarget*, vol. 8, no. 63, p. 107323, 2017.
- [61] Y. K. Tao *et al.*, “Assessment of breast pathologies using nonlinear microscopy,” *Proc. Natl. Acad. Sci.*, vol. 111, no. 43, pp. 15304–15309, 2014.
- [62] M. G. Giacomelli *et al.*, “Multiscale nonlinear microscopy and widefield white light imaging enables rapid histological imaging of surgical specimen margins,” *Biomed. Opt. Express*, vol. 9, no. 5, pp. 2457–2475, May 2018, doi: 10.1364/BOE.9.002457.
- [63] T. Yoshitake *et al.*, “Rapid histopathological imaging of skin and breast cancer surgical specimens using immersion microscopy with ultraviolet surface excitation,” *Sci. Rep.*, vol. 8, no. 1, pp. 1–12, 2018.
- [64] P.-C. Wu, T.-Y. Hsieh, Z.-U. Tsai, and T.-M. Liu, “In vivo quantification of the

- structural changes of collagens in a melanoma microenvironment with second and third harmonic generation microscopy,” *Sci. Rep.*, vol. 5, no. 1, pp. 1–7, 2015.
- [65] E. Gavgiotaki *et al.*, “THG imaging of lipid body profiles in diagnosis of biological samples,” *Med. Res. Arch.*, vol. 4, no. 7, 2016.
- [66] J. F. Adur *et al.*, “Quantitative changes in human epithelial cancers and osteogenesis imperfecta disease detected using nonlinear multicontrast microscopy,” *J. Biomed. Opt.*, vol. 17, no. 8, p. 81407, 2012.
- [67] Z. Zhang, N. V Kuzmin, M. L. Groot, and J. C. de Munck, “Quantitative comparison of 3D third harmonic generation and fluorescence microscopy images,” *J. Biophotonics*, vol. 11, no. 1, p. e201600256, 2018.
- [68] E. Gavgiotaki *et al.*, “Distinction between breast cancer cell subtypes using third harmonic generation microscopy,” *J. Biophotonics*, vol. 10, no. 9, pp. 1152–1162, Sep. 2017, doi: 10.1002/jbio.201600173.
- [69] D. Débarre *et al.*, “Imaging lipid bodies in cells and tissues using third-harmonic generation microscopy,” *Nat. Methods*, vol. 3, no. 1, pp. 47–53, Jan. 2006, doi: 10.1038/nmeth813.
- [70] P. T. Bozza and J. P. B. Viola, “Lipid droplets in inflammation and cancer,” *Prostaglandins, Leukot. Essent. Fat. Acids*, vol. 82, no. 4–6, pp. 243–250, 2010.
- [71] E. Gavgiotaki *et al.*, “Third Harmonic Generation microscopy distinguishes malignant cell grade in human breast tissue biopsies,” *Sci. Rep.*, vol. 10, no. 1, p. 11055, Dec. 2020, doi: 10.1038/s41598-020-67857-y.
- [72] A. H. Fischer, K. A. Jacobson, J. Rose, and R. Zeller, “Hematoxylin and eosin staining of tissue and cell sections,” *Cold Spring Harb. Protoc.*, vol. 3, no. 5, May 2008, doi: 10.1101/pdb.prot4986.
- [73] G. Falzon, S. Pearson, and R. Murison, “Analysis of collagen fibre shape changes in breast cancer,” *Phys. Med. Biol.*, vol. 53, no. 23, p. 6641, 2008.
- [74] K. Tilbury and P. J. Campagnola, “Applications of second-harmonic generation imaging microscopy in ovarian and breast cancer,” *Perspect. Medicin. Chem.*, vol. 7, p. PMC-S13214, 2015.
- [75] R. Ambekar, T.-Y. Lau, M. Walsh, R. Bhargava, and K. C. Toussaint, “Quantifying collagen structure in breast biopsies using second-harmonic generation imaging,” *Biomed. Opt. Express*, vol. 3, no. 9, pp. 2021–2035, 2012.
- [76] I. Prvulović, I. Kardum-Skelin, D. Susterčić, J. Jakić-Razumović, and S. Manojlović, “Morphometry of tumor cells in different grades and types of breast cancer,” *Coll. Antropol.*, vol. 34, no. 1, pp. 99–103, 2010.
- [77] A. I. Baba and C. Câtoi, “Tumors of the respiratory system,” in *Comparative Oncology*, The Publishing House of the Romanian Academy, 2007.
- [78] E. Gavgiotaki *et al.*, “Detection of the T cell activation state using nonlinear optical microscopy,” *J. Biophotonics*, vol. 12, no. 3, p. e201800277, Mar. 2019, doi: 10.1002/jbio.201800277.
- [79] I. Goodfellow, Y. Bengio, A. Courville, and Y. Bengio, “Deep learning. vol. 1.” MIT press Cambridge, 2016.
- [80] Y. Lecun, Y. Bengio, and G. Hinton, “Deep learning,” *Nature*, vol. 521, no. 7553, Nature Publishing Group, pp. 436–444, May 27, 2015, doi: 10.1038/nature14539.

- [81] S. You *et al.*, “Real-time intraoperative diagnosis by deep neural network driven multiphoton virtual histology,” *npj Precis. Oncol.*, vol. 3, no. 1, p. 33, Dec. 2019, doi: 10.1038/s41698-019-0104-3.
- [82] F. Emmert-Streib, Z. Yang, H. Feng, S. Tripathi, and M. Dehmer, “An introductory review of deep learning for prediction models with big data. Front,” *Artif. Intell.*, vol. 3, no. 4, 2020.
- [83] V. Nair and G. E. Hinton, “Rectified Linear Units Improve Restricted Boltzmann Machines,” Jan. 2010.
- [84] S. Lawrence, C. L. Giles, A. C. Tsoi, and A. D. Back, “Face recognition: A convolutional neural-network approach,” *IEEE Trans. neural networks*, vol. 8, no. 1, pp. 98–113, 1997.
- [85] Y. Bengio, *Learning deep architectures for AI*. Now Publishers Inc, 2009.
- [86] M. D. Zeiler, “Adadelta: an adaptive learning rate method,” *arXiv Prepr. arXiv1212.5701*, 2012.
- [87] L. Shen, L. R. Margolies, J. H. Rothstein, E. Fluder, R. McBride, and W. Sieh, “Deep learning to improve breast cancer detection on screening mammography,” *Sci. Rep.*, vol. 9, no. 1, pp. 1–12, 2019.
- [88] L. Abdelrahman, M. Al Ghamdi, F. Collado-Mesa, and M. Abdel-Mottaleb, “Convolutional neural networks for breast cancer detection in mammography: A survey,” *Comput. Biol. Med.*, p. 104248, 2021.
- [89] H. Chougrad, H. Zouaki, and O. Alheyane, “Deep convolutional neural networks for breast cancer screening,” *Comput. Methods Programs Biomed.*, vol. 157, pp. 19–30, 2018.
- [90] T. Ayer, Q. Chen, and E. S. Burnside, “Artificial neural networks in mammography interpretation and diagnostic decision making,” *Comput. Math. Methods Med.*, vol. 2013, 2013.
- [91] S. Dabeer, M. M. Khan, and S. Islam, “Cancer diagnosis in histopathological image: CNN based approach,” *Informatics Med. Unlocked*, vol. 16, p. 100231, 2019.
- [92] C. Zhu, F. Song, Y. Wang, H. Dong, Y. Guo, and J. Liu, “Breast cancer histopathology image classification through assembling multiple compact CNNs,” *BMC Med. Inform. Decis. Mak.*, vol. 19, no. 1, pp. 1–17, 2019.
- [93] S. H. Kassani, P. H. Kassani, M. J. Wesolowski, K. A. Schneider, and R. Deters, “Classification of histopathological biopsy images using ensemble of deep learning networks,” *arXiv Prepr. arXiv1909.11870*, 2019.
- [94] M. A. Aleskandarany, M. E. Vandenberghe, C. Marchiò, I. O. Ellis, A. Sapino, and E. A. Rakha, “Tumour heterogeneity of breast cancer: from morphology to personalised medicine,” *Pathobiology*, vol. 85, no. 1–2, pp. 23–34, 2018.
- [95] S. Ioffe and C. Szegedy, “Batch normalization: Accelerating deep network training by reducing internal covariate shift,” in *32nd International Conference on Machine Learning, ICML 2015*, Feb. 2015, vol. 1, pp. 448–456, Accessed: Dec. 07, 2020. [Online]. Available: <https://arxiv.org/abs/1502.03167v3>.
- [96] U. Von Luxburg and B. Schölkopf, “Statistical learning theory: Models, concepts, and results,” in *Handbook of the History of Logic*, vol. 10, Elsevier, 2011, pp. 651–706.
- [97] S. Witte *et al.*, “Label-free live brain imaging and targeted patching with third-harmonic generation microscopy,” *Proc. Natl. Acad. Sci.*, vol. 108, no. 15, pp. 5970–

- 5975, 2011.
- [98] S. You *et al.*, “Intravital imaging by simultaneous label-free autofluorescence-multiharmonic microscopy,” *Nat. Commun.*, vol. 9, no. 1, pp. 1–9, Dec. 2018, doi: 10.1038/s41467-018-04470-8.
- [99] T. Hompland, A. Erikson, M. Lindgren, T. Lindmo, and C. de Lange Davies, “Second-harmonic generation in collagen as a potential cancer diagnostic parameter,” *J. Biomed. Opt.*, vol. 13, no. 5, p. 054050, 2008, doi: 10.1117/1.2983664.
- [100] N. D. Kirkpatrick, M. A. Brewer, and U. Utzinger, “Endogenous optical biomarkers of ovarian cancer evaluated with multiphoton microscopy,” *Cancer Epidemiol. Biomarkers Prev.*, vol. 16, no. 10, pp. 2048–2057, Oct. 2007, doi: 10.1158/1055-9965.EPI-07-0009.
- [101] C. Morrison, J. Thornhill, and E. Gaffney, “The connective tissue framework in the normal prostate, B.P.H and prostate cancer: Analysis by scanning electron microscopy after cellular digestion,” *Urol. Res.*, vol. 28, no. 5, pp. 304–307, Oct. 2000, doi: 10.1007/s002400000123.
- [102] P. J. Campagnola and L. M. Loew, “Second-harmonic imaging microscopy for visualizing biomolecular arrays in cells, tissues and organisms,” *Nature Biotechnology*, vol. 21, no. 11, pp. 1356–1360, Nov. 2003, doi: 10.1038/nbt894.
- [103] M. Fang, J. Yuan, C. Peng, and Y. Li, “Collagen as a double-edged sword in tumor progression,” *Tumor Biology*, vol. 35, no. 4, Kluwer Academic Publishers, pp. 2871–2882, Apr. 2014, doi: 10.1007/s13277-013-1511-7.
- [104] B. Brodsky and A. V. Persikov, “Molecular structure of the collagen triple helix,” *Adv. Protein Chem.*, vol. 70, pp. 301–339, 2005, doi: 10.1016/S0065-3233(05)70009-7.
- [105] P. A. Torzilli, J. W. Bourne, T. Cigler, and C. T. Vincent, “A new paradigm for mechanobiological mechanisms in tumor metastasis,” *Seminars in Cancer Biology*, vol. 22, no. 5–6, pp. 385–395, Oct. 2012, doi: 10.1016/j.semcancer.2012.05.002.
- [106] P. P. Provenzano, K. W. Eliceiri, J. M. Campbell, D. R. Inman, J. G. White, and P. J. Keely, “Collagen reorganization at the tumor-stromal interface facilitates local invasion,” *BMC Med.*, vol. 4, no. 1, p. 38, Dec. 2006, doi: 10.1186/1741-7015-4-38.
- [107] X. Tang *et al.*, “Mechanical force affects expression of an in vitro metastasis-like phenotype in HCT-8 cells,” *Biophys. J.*, vol. 99, no. 8, pp. 2460–2469, Oct. 2010, doi: 10.1016/j.bpj.2010.08.034.
- [108] L. Bingle, N. J. Brown, and C. E. Lewis, “The role of tumour-associated macrophages in tumour progression: Implications for new anticancer therapies,” *Journal of Pathology*, vol. 196, no. 3, pp. 254–265, 2002, doi: 10.1002/path.1027.
- [109] J. N. Wolfe, “Risk for breast cancer development determined by mammographic parenchymal pattern,” *Cancer*, vol. 37, no. 5, pp. 2486–2492, 1976, doi: 10.1002/1097-0142(197605)37:5<2486::AID-CNCR2820370542>3.0.CO;2-8.
- [110] C.-K. Chou, W.-L. Chen, P. T. Fwu, S.-J. Lin, H.-S. Lee, and C.-Y. Dong, “Polarization ellipticity compensation in polarization second-harmonic generation microscopy without specimen rotation,” *J. Biomed. Opt.*, vol. 13, no. 1, p. 014005, 2008, doi: 10.1117/1.2824379.
- [111] S. Psilodimitrakopoulos, L. Mouchliadis, I. Paradisanos, A. Lemonis, G. Kioseoglou, and E. Stratakis, “Ultrahigh-resolution nonlinear optical imaging of the armchair orientation in 2D transition metal dichalcogenides,” *Light Sci. Appl.*, vol. 7, no. 5, pp. 18005–18005, May 2018, doi: 10.1038/lsa.2018.5.

- [112] M. G. Monaghan, S. Kroll, S. Y. Brucker, and K. Schenke-Layland, “Enabling Multiphoton and Second Harmonic Generation Imaging in Paraffin-Embedded and Histologically Stained Sections,” *Tissue Eng. - Part C Methods*, vol. 22, no. 6, pp. 517–523, Jun. 2016, doi: 10.1089/ten.tec.2016.0071.
- [113] W. L. Chen *et al.*, “Second harmonic generation  $\chi$  tensor microscopy for tissue imaging,” *Appl. Phys. Lett.*, vol. 94, no. 18, p. 183902, May 2009, doi: 10.1063/1.3132062.
- [114] S. W. Chu *et al.*, “Studies of  $\chi(2)/\chi(3)$  tensors in submicron-scaled bio-tissues by polarization harmonics optical microscopy,” *Biophys. J.*, vol. 86, no. 6, pp. 3914–3922, 2004, doi: 10.1529/biophysj.103.034595.
- [115] R. M. Williams, W. R. Zipfel, and W. W. Webb, “Interpreting second-harmonic generation images of collagen I fibrils,” *Biophys. J.*, vol. 88, no. 2, pp. 1377–1386, 2005, doi: 10.1529/biophysj.104.047308.
- [116] P. Matteini *et al.*, “Photothermally-induced disordered patterns of corneal collagen revealed by SHG imaging,” *Opt. Express*, vol. 17, no. 6, p. 4868, Mar. 2009, doi: 10.1364/oe.17.004868.
- [117] L. Mostaçõ-Guidolin, N. L. Rosin, and T. L. Hackett, “Imaging collagen in scar tissue: Developments in second harmonic generation microscopy for biomedical applications,” *Int. J. Mol. Sci.*, vol. 18, no. 8, p. 1772, Aug. 2017, doi: 10.3390/ijms18081772.
- [118] G. Ducourthial *et al.*, “Monitoring dynamic collagen reorganization during skin stretching with fast polarization-resolved second harmonic generation imaging,” *J. Biophotonics*, vol. 12, no. 5, p. e201800336, May 2019, doi: 10.1002/jbio.201800336.
- [119] D. J. S. Hulmes, “Building collagen molecules, fibrils, and suprafibrillar structures,” in *Journal of Structural Biology*, 2002, vol. 137, no. 1–2, pp. 2–10, doi: 10.1006/jsbi.2002.4450.
- [120] A. S. Quigley, S. Bancelin, D. Deska-Gauthier, F. Légaré, L. Kreplak, and S. P. Veres, “In tendons, differing physiological requirements lead to functionally distinct nanostructures,” *Sci. Rep.*, vol. 8, no. 1, pp. 1–14, Dec. 2018, doi: 10.1038/s41598-018-22741-8.
- [121] E. I. Romijn, A. Finnøy, and M. B. Lilledahl, “Analyzing the feasibility of discriminating between collagen types I and II using polarization-resolved second harmonic generation,” *J. Biophotonics*, vol. 12, no. 1, p. e201800090, Jan. 2019, doi: 10.1002/jbio.201800090.
- [122] F. J. Ávila, O. Del Barco, and J. M. Bueno, “Polarization dependence of aligned collagen tissues imaged with second harmonic generation microscopy,” *J. Biomed. Opt.*, vol. 20, no. 8, p. 86001, Aug. 2015, doi: 10.1117/1.JBO.20.8.086001.
- [123] D. F. Holmes, Y. Lu, T. Starborg, and K. E. Kadler, “Collagen Fibril Assembly and Function,” in *Current Topics in Developmental Biology*, vol. 130, Academic Press Inc., 2018, pp. 107–142.
- [124] M. J. Buehler, “Nature designs tough collagen: Explaining the nanostructure of collagen fibrils,” *Proc. Natl. Acad. Sci. U. S. A.*, vol. 103, no. 33, pp. 12285–12290, Aug. 2006, doi: 10.1073/pnas.0603216103.
- [125] K. R. Campbell, R. Chaudhary, J. M. Handel, M. S. Patankar, and P. J. Campagnola, “Polarization-resolved second harmonic generation imaging of human ovarian cancer,” *J. Biomed. Opt.*, vol. 23, no. 6, pp. 1–8, 2018, doi:

- 10.1117/1.JBO.23.6.066501.
- [126] R. Mercatelli *et al.*, “Morpho-mechanics of human collagen superstructures revealed by all-optical correlative micro-spectroscopies,” *Commun. Biol.*, vol. 2, no. 1, pp. 1–10, Dec. 2019, doi: 10.1038/s42003-019-0357-y.
- [127] R. Mercatelli, T. Triulzi, F. S. Pavone, R. Orlandi, and R. Cicchi, “Collagen ultrastructural symmetry and its malignant alterations in human breast cancer revealed by Polarization microscopy,” *J. Biophotonics*, p. jbio.202000159, May 2020, doi: 10.1002/jbio.202000159.
- [128] C. Teulon, I. Gusachenko, G. Latour, and M.-C. Schanne-Klein, “Theoretical, numerical and experimental study of geometrical parameters that affect anisotropy measurements in polarization-resolved SHG microscopy,” *Opt. Express*, vol. 23, no. 7, p. 9313, Apr. 2015, doi: 10.1364/oe.23.009313.
- [129] S. Z. Despotović *et al.*, “Altered organization of collagen fibers in the uninvolved human colon mucosa 10 cm and 20 cm away from the malignant tumor,” *Sci. Rep.*, vol. 10, no. 1, pp. 1–11, Dec. 2020, doi: 10.1038/s41598-020-63368-y.
- [130] E. Gavgiotaki *et al.*, “Nonlinear imaging of female breast tissue biopsies,” in *Advances in Microscopic Imaging II*, Jul. 2019, vol. 11076, p. 18, doi: 10.1117/12.2526285.
- [131] M. Zimmerley, P. Mahou, D. Débarre, M. C. Schanne-Klein, and E. Beaurepaire, “Probing ordered lipid assemblies with polarized third-harmonic-generation microscopy,” *Phys. Rev. X*, vol. 3, no. 1, p. 011002, Jan. 2013, doi: 10.1103/PhysRevX.3.011002.
- [132] G. Ducourthial *et al.*, “Development of a real-time flexible multiphoton microendoscope for label-free imaging in a live animal,” *Sci. Rep.*, vol. 5, no. 1, pp. 1–9, Dec. 2015, doi: 10.1038/srep18303.
- [133] A. Lombardini *et al.*, “High-resolution multimodal flexible coherent Raman endoscope article,” *Light Sci. Appl.*, vol. 7, no. 1, pp. 1–8, Dec. 2018, doi: 10.1038/s41377-018-0003-3.
- [134] V. Santilli, A. Bernetti, M. Mangone, and M. Paoloni, “Clinical definition of sarcopenia,” *Clin. cases Miner. bone Metab.*, vol. 11, no. 3, p. 177, 2014.
- [135] L. V Thompson, “Age-related muscle dysfunction,” *Exp. Gerontol.*, vol. 44, no. 1–2, pp. 106–111, 2009.
- [136] H. Kagawa, T. Takaya, R. Ruksana, F. Anokye-Danso, M. Z. Amin, and H. Terami, “C. elegans model for studying tropomyosin and troponin regulations of muscle contraction and animal behavior,” *Regul. Mech. Striated Muscle Contract.*, pp. 153–161, 2007.
- [137] H. N. Aguilar and B. F. Mitchell, “Physiological pathways and molecular mechanisms regulating uterine contractility,” *Hum. Reprod. Update*, vol. 16, no. 6, pp. 725–744, 2010.
- [138] P. Bianchini and A. Diaspro, “Three-dimensional (3D) backward and forward second harmonic generation (SHG) microscopy of biological tissues,” *J. Biophotonics*, vol. 1, no. 6, pp. 443–450, 2008.
- [139] V. Nucciotti *et al.*, “Probing myosin structural conformation in vivo by second-harmonic generation microscopy,” *Proc. Natl. Acad. Sci.*, vol. 107, no. 17, pp. 7763–7768, 2010.
- [140] I. Amat-Roldan, S. Psilodimitrakopoulos, P. Loza-Alvarez, and D. Artigas, “Fast

- image analysis in polarization SHG microscopy,” *Opt. Express*, vol. 18, no. 16, p. 17209, Aug. 2010, doi: 10.1364/oe.18.017209.
- [141] C. Yuan *et al.*, “Study of the expression transition of cardiac myosin using polarization-dependent SHG microscopy,” *Biophys. J.*, vol. 118, no. 5, pp. 1058–1066, 2020.
- [142] C. Yuan *et al.*, “Changes in the crystallographic structures of cardiac myosin filaments detected by polarization-dependent second harmonic generation microscopy,” *Biomed. Opt. Express*, vol. 10, no. 7, pp. 3183–3195, 2019.
- [143] S. Brenner, “The genetics of *Caenorhabditis elegans*,” *Genetics*, vol. 77, no. 1, pp. 71–94, 1974.
- [144] X. Y. Dow, E. L. DeWalt, J. A. Newman, C. M. Dettmar, and G. J. Simpson, “Unified Theory for Polarization Analysis in Second Harmonic and Sum Frequency Microscopy,” *Biophys. J.*, vol. 111, no. 7, pp. 1553–1568, Oct. 2016, doi: 10.1016/j.bpj.2016.04.019.
- [145] “MusFIG 9 Legend.”  
<https://www.wormatlas.org/hermaphrodite/musclesomatic/MusSomaticframeset.html>  
 (accessed Jan. 11, 2021).
- [146] M. Mari, V. Tsafas, K. Melessanaki, and G. Filippidis, “Applications of non-linear imaging microscopy techniques to cultural heritage objects,” *Insight-Non-Destructive Test. Cond. Monit.*, vol. 60, no. 12, pp. 663–669, 2018.
- [147] M. Oujja *et al.*, “Nonlinear imaging microscopy for assessing structural and photochemical modifications upon laser removal of dammar varnish on photosensitive substrates,” *Phys. Chem. Chem. Phys.*, vol. 19, no. 34, pp. 22836–22843, 2017.
- [148] G. Filippidis *et al.*, “Assessment of in-depth degradation of artificially aged triterpenoid paint varnishes using nonlinear microscopy techniques,” *Microsc. Microanal.*, vol. 21, no. 2, p. 510, 2015.
- [149] G. Filippidis, K. Melessanaki, and C. Fotakis, “Second and third harmonic generation measurements of glues used for lining textile supports of painted artworks,” *Anal. Bioanal. Chem.*, vol. 395, no. 7, pp. 2161–2166, 2009.
- [150] S. Psilodimitrakopoulos, E. Gavgiotaki, K. Melessanaki, V. Tsafas, and G. Filippidis, “Polarization Second Harmonic Generation Discriminates Between Fresh and Aged Starch-Based Adhesives Used in Cultural Heritage,” *Microsc. Microanal.*, vol. 22, no. 5, p. 1072, 2016.
- [151] G. Latour, J.-P. Echard, M. Didier, and M.-C. Schanne-Klein, “In situ 3D characterization of historical coatings and wood using multimodal nonlinear optical microscopy,” *Opt. Express*, vol. 20, no. 22, pp. 24623–24635, 2012.
- [152] F. Faraldi, G. J. Tserevelakis, G. Filippidis, G. M. Ingo, C. Riccucci, and C. Fotakis, “Multi photon excitation fluorescence imaging microscopy for the precise characterization of corrosion layers in silver-based artifacts,” *Appl. Phys. A*, vol. 111, no. 1, pp. 177–181, 2013.
- [153] M. Mari and G. Filippidis, “Non-Linear Microscopy: A Well-Established Technique for Biological Applications towards Serving as a Diagnostic Tool for in situ Cultural Heritage Studies,” *Sustainability*, vol. 12, no. 4, p. 1409, 2020.
- [154] G. Filippidis, E. J. Gualda, K. Melessanaki, and C. Fotakis, “Nonlinear imaging microscopy techniques as diagnostic tools for art conservation studies,” *Opt. Lett.*, vol. 33, no. 3, pp. 240–242, 2008.

- [155] A. Selimis *et al.*, “Nonlinear microscopy techniques for assessing the UV laser polymer interactions,” *Opt. Express*, vol. 20, no. 4, pp. 3990–3996, 2012.
- [156] J. Yao and L. V Wang, “Photoacoustic microscopy,” *Laser Photon. Rev.*, vol. 7, no. 5, pp. 758–778, 2013.
- [157] G. J. Tserevelakis *et al.*, “Photoacoustic imaging reveals hidden underdrawings in paintings,” *Sci. Rep.*, vol. 7, no. 1, pp. 1–11, 2017.
- [158] G. J. Tserevelakis, A. Dal Fovo, K. Melessanaki, R. Fontana, and G. Zacharakis, “Photoacoustic signal attenuation analysis for the assessment of thin layers thickness in paintings,” *J. Appl. Phys.*, vol. 123, no. 12, p. 123102, 2018.
- [159] G. J. Tserevelakis, M. Tsagkaraki, P. Siozos, and G. Zacharakis, “Uncovering the hidden content of layered documents by means of photoacoustic imaging,” *Strain*, vol. 55, no. 2, p. e12289, 2019.